The Dissertation Committee for Ignacio Francisco Gallardo Certifies that this is the approved version of the following dissertation:

TUNING OF CORE-SHELL HETEROSTRUCTURED NANOPARTICLES GENERATED BY LASER ABLATION OF MICROPARTICLES

Committee:

John W. Keto Supervisor

Ken-Shih

Greg O. Sitz

Ernst-Ludwig Florin

Desiderio Kovar

TUNING OF CORE-SHELL HETEROSTRUCTURED NANOPARTICLES GENERATED BY LASER ABLATION OF MICROPARTICLES

by

Ignacio Francisco Gallardo, BS

Dissertation

Presented to the Faculty of the Graduate School of

The University of Texas at Austin

in Partial Fulfillment

of the Requirements

for the Degree of

Doctor of Philosophy

The University of Texas at Austin

May, 2009

Dedication

Para: Miguel Gallardo Rodriguez
y Jorge Eduardo Tenorio Guerra.

Si ellos no me hubieran despertado el interés por la física, el Nacho actual y esta disertacion doctoral no existirian.
(If they hadn't awakened my interest in Physics, the current Nacho and this doctoral dissertation wouldn't exist.)

Acknowledgements

I would like to thank Professor John Keto for his time, advice, guidance and patience. Special thanks to Dr. Keto’s lab students (current and former): Dr. David Stoker, John Dunn, Nathan Erickson, Leah Hesla, Hoda Tavakoli, Rodoflo Barniol-Duran, Rualdo Soto-Chavez, Yingyue Boretz, Kanon J. and Sandra Lang for their invaluable help and friendship. Students (and former students) equally helpful but in different labs include but are not limited to: Dr. Daniel O’Brien, Dr. Chong Huang, Kris Gleason, Dr. Andre Albert, Dr. James Ma, Manuj Nahar, Wenqian Wang, Jaclyn Wiggins and Robert Morgan. Equally thanks to Laura Mondino, Jack Clifford, Allan Schroeder and Michael Ronalter for their hard work and machine training.

Thanks to Dr. Kay Hoffmann, Dr. Manfred Fink, Dr. Mike Becker, Dr. Desiderio Kovar, Dr. Greg Sitz, Dr. Ernst-Ludwig Florin, Dr. Chih-Kang Ken Shih, Dr. George Sudarshan, Dr. Gerald Hoffmann, Dr. Mike Marder, Dr. Angela Bardo, Dr. John Mendenhall, Dr. Lew Rabenberg, Dr. Brian Korgel, Dr. Ji-Ping Zhou, Dr. William Lackowski, Dr. Yiaming Sun, Dr. Luis Orozco. Dr. Braulio Medina, Dr. George Shubeita, Dr. Alan Campion and Dr. Paulo Ferreira. I would be here without them.

The Physics Department of The Univeristy of Texas at Austin, the Center for Nano and Molecular Science and Technology, (CNM), the Robert A. Welch Foundation,

the Strategic Partnership for Research In Nanotechnology, (SPRING), and CONACYT deserve my appreciation for sharing with me their facilities and financial support.

In addition to the people above who contributed in many ways to this dissertation and my doctoral candidate experience, my family bellow supported me with all their moral strenght and friendship. Alejandra Guerra, Miguel Gallardo & Ivette Montero, Alejandra Gallardo, Ronald Gallardo, Maria Luisa Guerra, Raul Gutierrez, Monica Gutierrez, Raul Gutierrez Jr, Margarita Guerra, Alfonso Betancourt, Margarita Betancourt, Alfonso Betancourt Jr, Carla Betancourt, Manuela Guerra, Manuela Maria Guerra & Ezequiel Rodriguez, Nacho Guerra and Eduardo Guerra.

I also want to thank the friends that I met in Austin, those who have gone away and those who are still in town.

I don't want to put names here because I am sure I will forget some, but I will try a few of the manes that remind me to the fabulous people I have come across during my time in Austin: Puya, Clayton, Bob, Omar, Homer, Mani, Usama, Ryan, Nathaniel, Adam, Hugo, Juanra, Debora, Tiffany, Terri, Sean, Yehoshua, Hector, Matt, Hrishikesh, David, Alan, Angel, Rafael, Rafal, Tonkang, Gabriel, Arban, Fatmir, Kevin, Marcus, Vaggelis, Francisco, Ramon, Carlos, Cesar, Takahide, Jun, Dylan, Elia, Kevin, Roland, Michael, Levent, Massimo, Dongil, Dagim, Larry, Yafis, Adolfo, Hossein, Sarp, Paul, Suchin, Kaleem, Mathias, Mohamed, Tim, Emmanuala, Bo, Maria, Katie, Ion, Isaac, Pablo, Matilde, Nick, Melissa, Estivalis, Paula, Karina, Charlotte, Anne, Victor, Rudy, Phillip, Matthew, Jakub, Ryan, Alex, Sarah, Zhaowen, Kimby, Morgann, Miguel, Thai, Carol, Jose, Jamie, Silvia, Martin, Lucia, Luis, Maria, Yanick, Richard, Adriana, Michal, Petar, Tobias, Rohit, Marcos, Sonya, Virginia, Debby, Harry, Nick, Alexander, Walter, Mar, Gemma, Renato, Mauricio, Tania, Hernan, Claudia, Manuel, Lorena, Gladiola, Adriana, Eva, Martin, Tim, Aynur, Rodirgo, Erick, Hector, Miguel, Arcelia, Valentina, Dolgor, Fayola, Ricardo, Renata, Vanessa, Emanuel, Davi, Ilani, Valdo, Ashutosh, Zackary, Simone, Benedetta, Alessandro, Marcello, Andrea, Nuni, Lucy, Donna, Gabriel, Saskia, Mirko, Mateo, Juana, Winnie, Nancy, Veronica, Silvia, Christine, Judy, Jaqueline, Marina, Nalini, Jason, Supna, Kim, Sandra, Joao, Bryan, Diego, Vanessa, Murilo, Eduardo, Danielli, Ricardo, Lourdes, Masa, Sasha, Claudia, Llewyn, Theresa, Nick, Rachel, Hyewon, Crystal, Ernest, Holly, Flavia, Jaime Alison, Guillermo, Alice, Jonathan, Alistar, Antonio, Reza, Alvaro, Shelly, Nicky, Romain, Lorenzo, Amy, Aracely, Armando, Ericka, Hunter, Belinda, Brendan, Cristina, Darlan, Cynthia, Domingo, Horacio, Vasilis, Kumar, Amit, Hilda, Ramesh, Yohanes, Joe, Neil and many more.

Last but not least I would also like to thank the friends from Mexico who were supportive and those who thought that I was never going to make it (it took me almost seven years to prove these friends wrong).

Apologies

To those who I forgot to thank and know that they should be in this page because without their help, support and friendship I couldn’t have made it (or maybe I could have made it but the journey would have been much harder, boring and worst).

I specially want to apologize to those who I couldn’t be with when they wanted me to be there for them. The least I could do is to show them this work as an excuse for my absence. This Ph.D. took me almost seven years to complete. I apologize to Marina Gallardo Calderon, Rafael Gallardo Rodriguez, and mimito, who left in times when I couldn’t say goodbye. Too bad I couldn’t be there for Jahaziel’s, Neto’s or Enrique’s wedding among many others. I was taking measurements during Miguel Jr. baptism and Fernando’s birthday. Everyone in my hometown is seven years older and I missed almost everyone’s birthday celebrations and I am not justified for not calling home more often than six times a year. With this pages I just want to show them all what I was doing far away in Austin, (besides partying on weekend nights and walking around the safe city).

TUNING OF CORE-SHELL HETEROSTRUCTURED NANOPARTICLES GENERATED BY LASER ABLATION OF MICROPARTICLES

Publication No.______________

Ignacio Francisco Gallardo, Ph.D
The University of Texas at Austin, 2009

Supervisor: John W. Keto

Laser Ablation of Microparticles (LAM) is a process of nanoparticle formation in which microparticles in a flowing aerosol are continuously ablated by high power laser pulses. For the first time, we have produced CdSe/ZnS core/shell nanoparticles using a double ablation apparatus, designed to undergo a two step LAM process. This process can be inverted to produce ZnS/CdSe core/shell nanoparticles. The present work focuses on the range around ~15 nm radius heterostructures and uses high resolution transmission electron microscopy (HRTEM) to image core and shells. For smaller particles core shell structures have been detected with a energy dispersive spectroscopy (EDS) 5 nm spot size beam, and fast Fourier transform (FFT) spectra. Differences in the ablation behavior were measured between the two IIB-VIA type semiconductors.

We investigate the temperature and size distribution of Ag, Ge, CdSe and ZnS nanoparticles undergoing UV excimer laser pulses. A two laser pulse experiment is designed to monitor nanoparticle size before and after laser interaction. We study HRTEM images and measure the ablation and fluorescence spectra of particles before and after evaporation. Results show that the nanoparticle mean radius decreases from 3.4 ± 0.2 nm to 2.6 ± 0.2 nm, from 4.3 ± 0.1 nm to 3.5 ± 0.1 nm, and from 3.1 ± 0.2 nm to 2.6 ± 0.2 nm for Ag, Ge and CdSe, respectively. No ZnS nanoparticle size reduction was observed. Theoretical models for nanoparticles undergoing laser heating show that temperatures above the bulk and nanoparticle material melting point reduce the nanoparticles size by a factor of 0.3 and suggest recondensation before collection. For CdSe nanoparticles collected on dry substrates and solvents, blue shifted fluorescence (PL) peaks support the size reduction.

Table of Contents

List of Tables

List of Figures

1. Introduction

Metallic and semiconductor nanoparticles exhibit unique size-tunable optical properties due to the confinement of the electronic wave functions. By changing the size of the nanoparticles, the optical absorption and emission can be selected across the visible spectrum, which makes these materials attractive for applications in optoelectronics, nonlinear optics [1] and selective charge confinement. [2] Also, their enhanced quantum yield is attractive in biophysics for their use as fluorescent probes in biological staining and diagnostics (labeling technologies). [3]

The high surface-to-volume ratio of nanoparticles suggests that the surface properties are of great importance when studying relevant optical properties like luminescence and quantum yield. Semiconductor nanoparticles capped by a wider band gap semiconductor have shown to exhibit enhanced band-edge luminescence and increased quantum yields up to one order of magnitude compared to surfactant-covered, unshelled nanoparticles. [4] For the cases when the wider band gap semiconductor makes the core, heterostructures have shown charge separation which is useful in the production of high frequency lasers. [2]

Core/shell nanoparticles have been previously prepared by chemical synthesis, using organometallic reagents. [4,5] The present work explains and discusses a process for core/shell nanoparticle production using Laser Ablation of Microparticles (LAM). LAM is a process for the production of nanoparticles of a wide variety of materials (metals, semiconductors and dielectrics), having relatively narrow nanoparticle size distributions and large production rates. [6] In the LAM process, a high-energy laser pulse ablates a microparticle (1-10 µm in radius) and generates a plasma. A subsequent shockwave produces the particle breakdown (vaporization) which is followed by a condensation of nanoparticles behind the shockwave. As a result, all the microparticle mass is converted to nanoparticles with a range of mean radius from 1.5 to 10 nm depending upon aerosol gas type and pressure. [7,8]

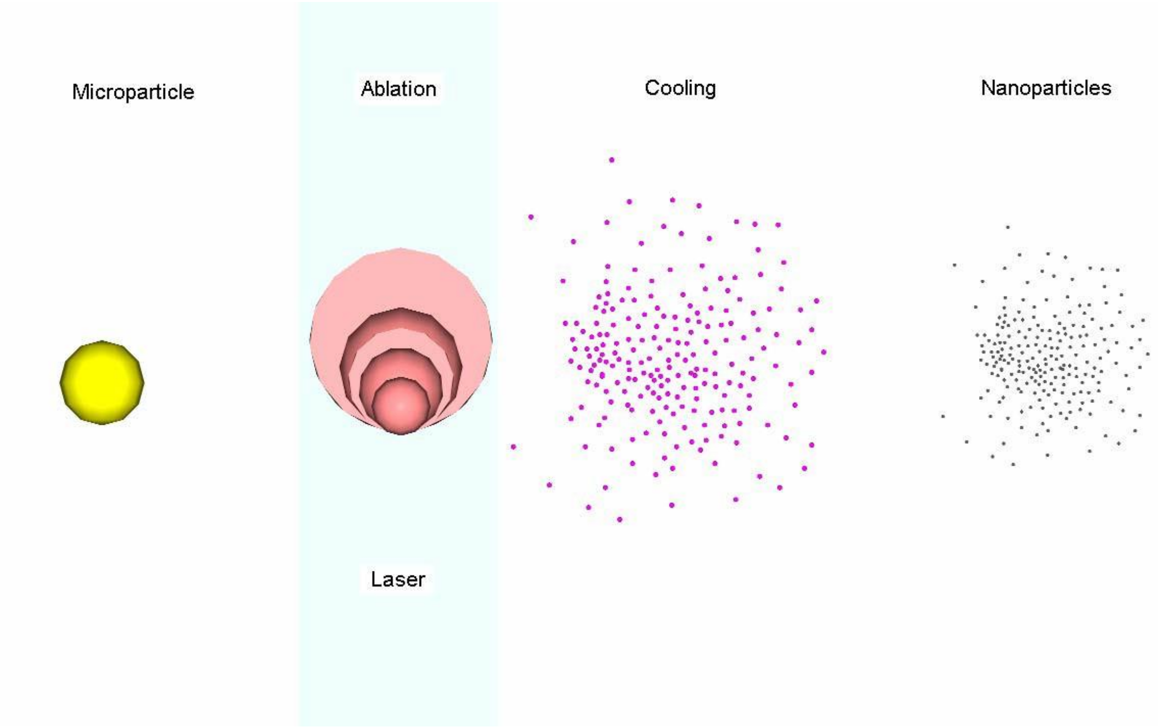

Figure 1: Laser ablation of microparticle (LAM) process.

CdSe/ZnS nanocrystals (NCs) generated by LAM need no organic ligands on their surfaces to be formed and therefore these bare nanoparticles are optimum for studying scientifically interesting surface effects associated with bleaching and blinking of CdSe/ZnS nanoparticles. LAM nanoparticles can be coated with different types of organic ligands to study how these modify the NCs fluorescent properties.

Kos, et al. point out that by using chemically grown NCs in electroluminescent applications, the carrier injection is inhibited by the organic surfactants bound to the surface. [9] This passivation layer and the conductive organic polymers used for carrier injection limit carrier mobility and resulting device performance. In an early study of electroluminescence from CdSe NC/polymer composites, Dabbousi et al. found I-V characteristics of a tunnel junction which they attributed to band offsets at the NC/polymer interface. [10] Instead, the insulating layer might be attributed to the trioctylphosphine oxide (TOPO) passivation layer. Other investigations of NC/semiconductor polymer light emitting devices (LEDs), [11,12] did not consider the effect of the passivation layers on carrier transport. The performance of conducting polymer/NC composite LEDs may be improved when these insulating capping layers are eliminated by the use of core/shell NCs with bare surfaces as are produced by LAM.

Though more difficult to manufacture than conducting polymer composites, it is possible to inject carriers into LAM produced NCs using an inorganic, high-mobiliity PN junction built using semiconductor quantum well structures. In related studies we measured electron mobilities in nanostructured films of supersonically impacted LAM produced Ag NCs. After impaction, mobilities were 8% of that of a bulk crystal due to void and grain boundary scattering, (grain size at impaction of 30 nm). This scattering was reduced significantly (mobilities 25% of bulk) by annealing at temperatures of only 100 C. [13] Though we would expect the sintering properties of semiconductor core/shell NCs to be significantly different than metals, these techniques might be used to produce inorganic NC composite LEDs.

In many applications, chemically made nanoparticles must undergo processes that exchange the organic ligands in which they were made, with those needed to incorporate the NCs in a target system such as a biological organelle. The quantum yield of the NC decreases 20 to 40% after some of these surface treatments. [14] For biological labeling, CdSe/ZnS NCs need to be soluble in water. For this reason, the organic ligands in which they are grown need to be replaced or encapsulated with bifunctional thiol ligands. Unfortunately the impact of this process on the photophysical properties of the quantum dots (QD's) is often complicated and deleterious. [14, 15] When using nanoparticles produced by LAM, they can be collected directly in any organic ligand desired for subsequent use.

The high surface-to-volume ratio of nanoparticles suggests that the surface properties are of great importance when studying relevant optical phenomena like quantum yield. Semiconductor nanoparticles that have smoother edges enhance band-edge luminescence and increase quantum yields. The large atomic number for Ge makes it an ideal semiconductor for size reduction visualization in the HRTEM. The large amount of data on Ag nanoparticles gives an ideal background to compare experiments with simulations, which require accurate experimental parameters.

2. Nanoparticle generation system

a. AEROSOL GENERATOR

The aerosol generator shown in Fig. 3 is the chamber in which the feedstock material is kept and mixed with a buffer gas. It consists of a stainless steel drum (0.84” ID, 1.48” OD and length of 1.73”) that can fit o-rings on both of its ends. On the top it is covered by a plastic transparent lid that helps for watching the microparticle powder level. The microparticle powder is put in through the detachable plastic lid. The lid is held with eight screws to avoid leaks through the upper o-ring seal. The microparticles are sitting on top of a rubber membrane around 0.5 mm thick that is flexible enough to be deformed 10 times per second by the magnetically driven iron plunger seated under it. The membrane is held in place between the main body of the drum and a stainless steel ring that fits on the down side of the drum and is sealed with four screws and a o-ring. The four screws go through the membrane and connect the metallic bottom ring with the drum. If the membrane wasn’t in place we would be able to see across the Z axis through the window and the hole on the center of the bottom ring. The bottom ring’s hole is threaded so that a solenoid screws tightly into it. The solenoid is manufactured by GR valve Inc. and normally used in pulsed supersonic nozzles and it is not required for the microparticles to be sealed inside the drum on top of the membrane. The solenoid is located inside a cylindrical jacket that screws in and allows for a plunger or iron core to fit and slide freely inside at the center of the electromagnet. The jacket is closed at the bottom so that the iron core sits at the bottom when there is no magnetic field. Between

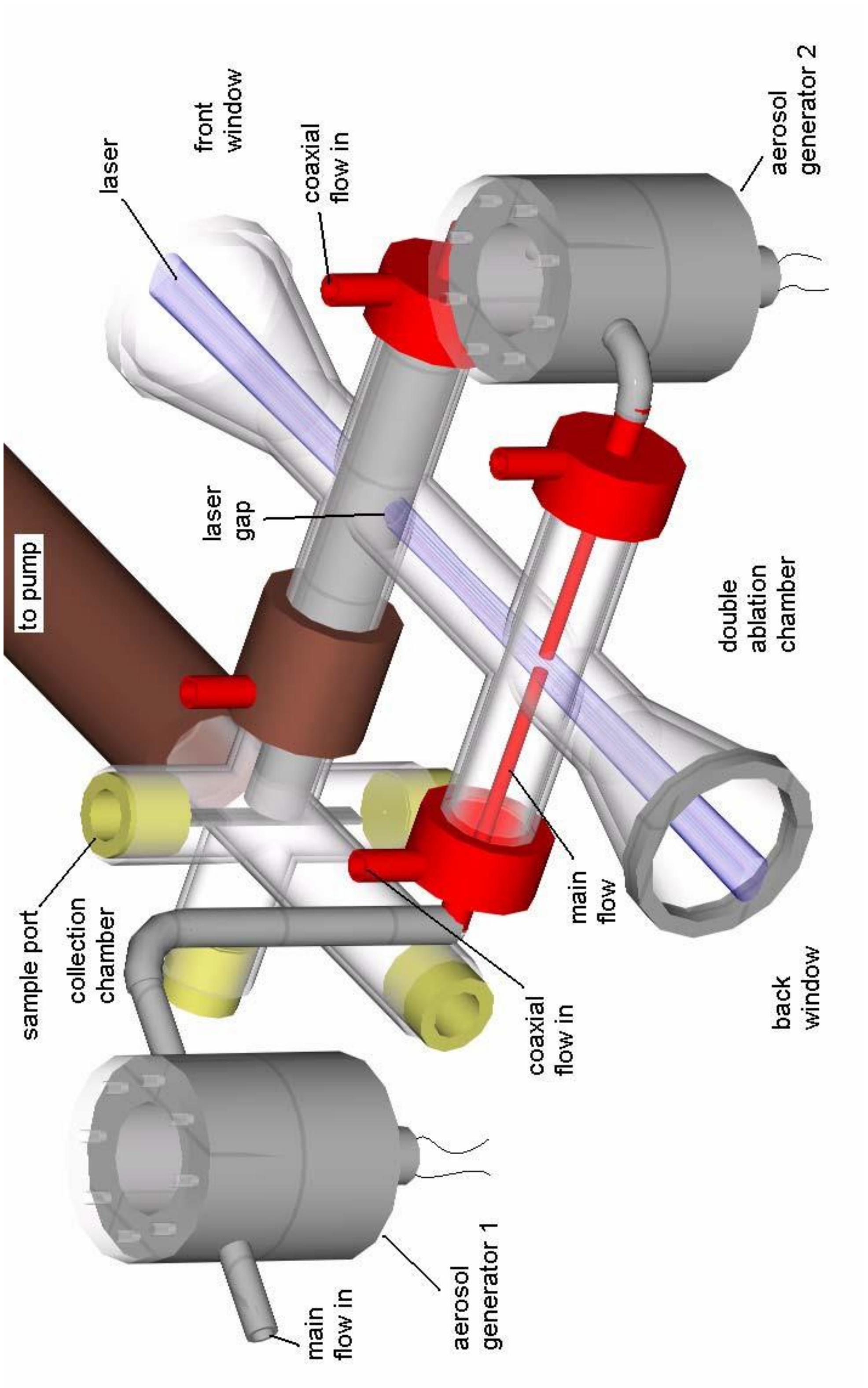

Figure 2: Ablation Chamber and Collection Chamber

the bottom of the electromagnet or solenoid and the iron plunger there is a compressible spring that pushes the plunger up. The compressibility of the spring is crucial for the maximum force that the plunger puts on the membrane. The 80 ohm solenoid consists of insulated copper wire that has around 200 turns. The solenoid is driven with a 60 V square wave that has a 10 Hertz frequency where the width of the positive pulse is only one tenth of the half-wave period.

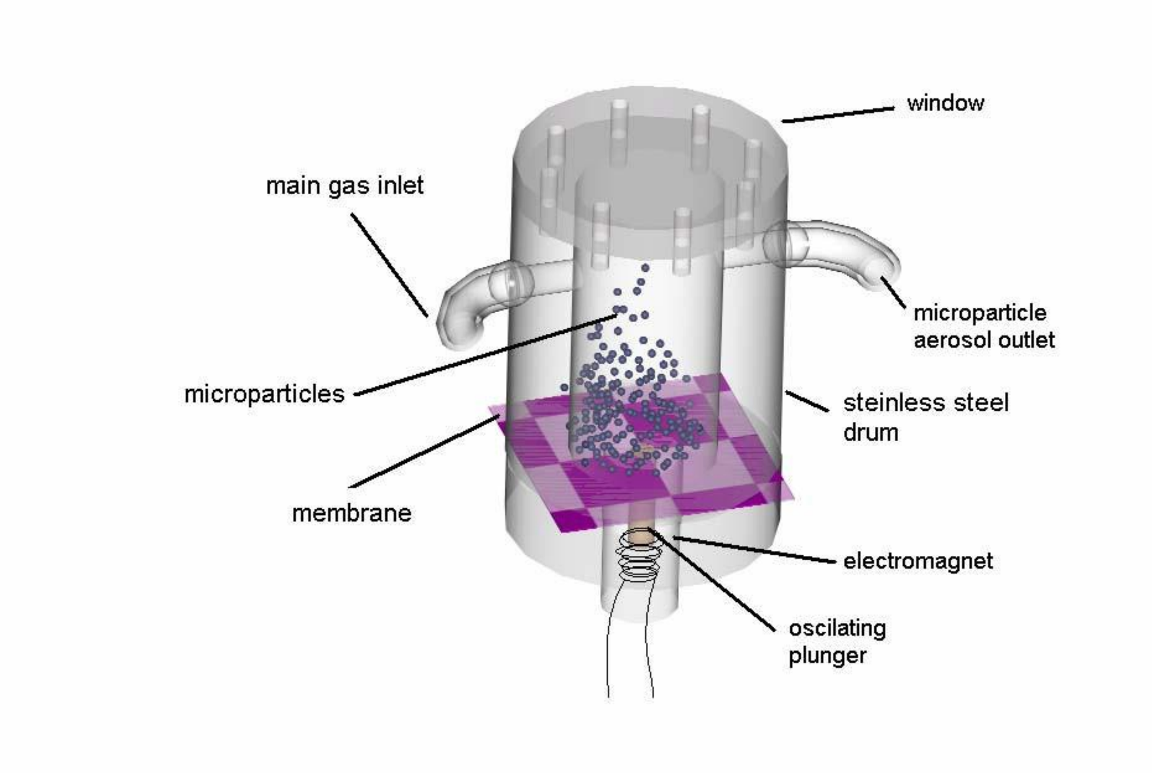

Figure 3: Aerosol Generator

This means that the solenoid is only activated one twentieth of a cycle. When the solenoid is activated a magnetic field is generated that attracts the plunger down to compress the spring. The plunger is held down only for one twentieth of the cycle and then is shot upward by the spring. To protect the membrane from the impact, we glue a stainless steel washer or a stainless steel mesh (cut the size of the diameter of the plunger) on the bottom of the membrane, so that it receives the direct impact. When the solenoid is off and the spring is relaxed the plunger pushes the membrane up and the powder is pushed away from the center of the drum onto the inside walls of the drum. When the solenoid is on, every time it has a non-zero voltage, the plunger is attracted down, the membrane relaxes and the powder falls down to the center of the feeder. Then the positive voltage is off the rest of the cycle and the spring pushes the plunger up so that it pushes the membrane and the microparticle powder is launched upwards. The microparticles reache high enough inside the drum (1.5" up from the relaxed membrane) to be carried away horizontally by the buffer gas that horizontally crosses the top of the drum 0.5 cm below the window. The buffer gas enters though a 0.25" tube that takes the microparticles to the ablation chamber. The amount of powder that flows into the ablation chamber is controlled by the amount of powder inside the aerosol generator, by the frequency of the square wave of the electromagnet, how deeply the electromagnet is screwed into the threaded bottom hole of the drum, the stiffness of the spring underneath the plunger (k, the spring constant) and the buffer gas flow inside the aerosol feeder.

The powder that sits on top of the membrane inside the aerosol generator consists of spherical microparticles that are purchased from several chemical companies, like Fisher Scientific, Dupont, Sigma Aldrich or Alfa Aesar. The spherical microparticles normally come covered with the organics that were involved in their synthesis process and help to keep them separated. These organics are present only on the surface of the microparticle and during ablation they may relocate to the surface of the nanoparticles, but the nanoparticle surfaces generated by the microparticle are 10^6 times larger than the original microparticle surface, (as seen from the SEM images on Figs. 4 for CdSe, 5 for

ZnS and 6 for Ag microparticles) which means that the number of organic molecules that could reside on a nanoparticle surface is negligible with respect to the number of nanoparticles that are formed from the same microparticle volume. We keep the microparticles in their sealed original bottles or inside the aerosol generators in a noble gas atmospheric pressure because they tend to cluster in the presence of water present in air.

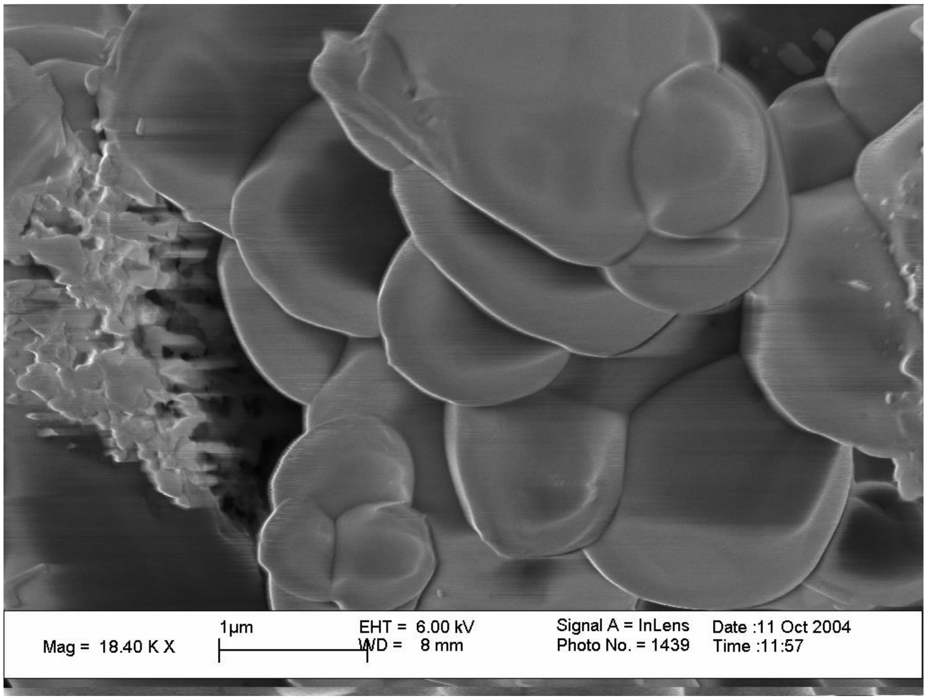

Figure 4: CdSe microparticles

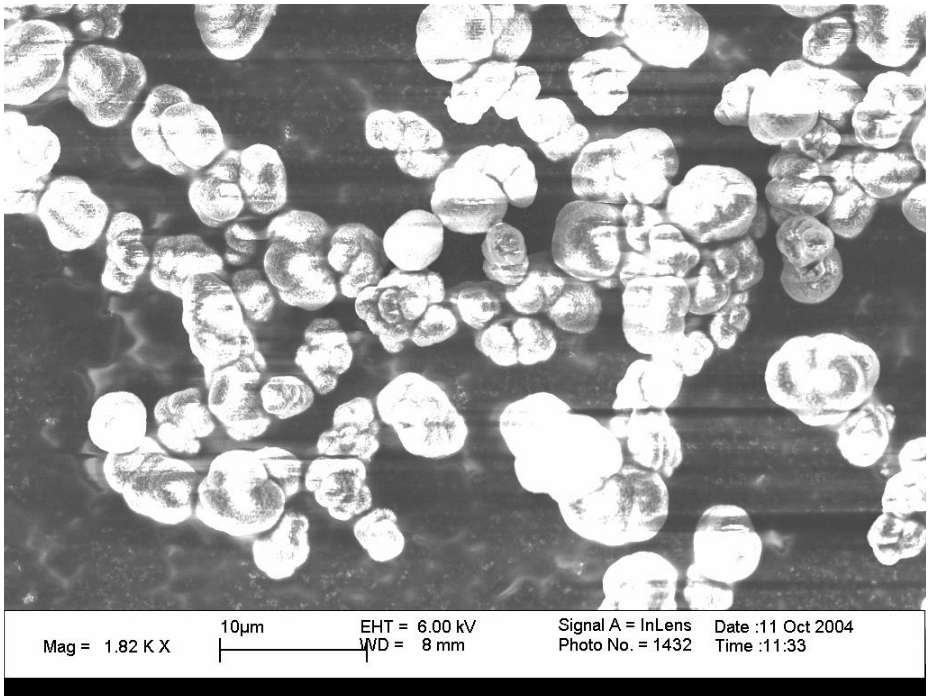

Figure 5: ZnS microparticles

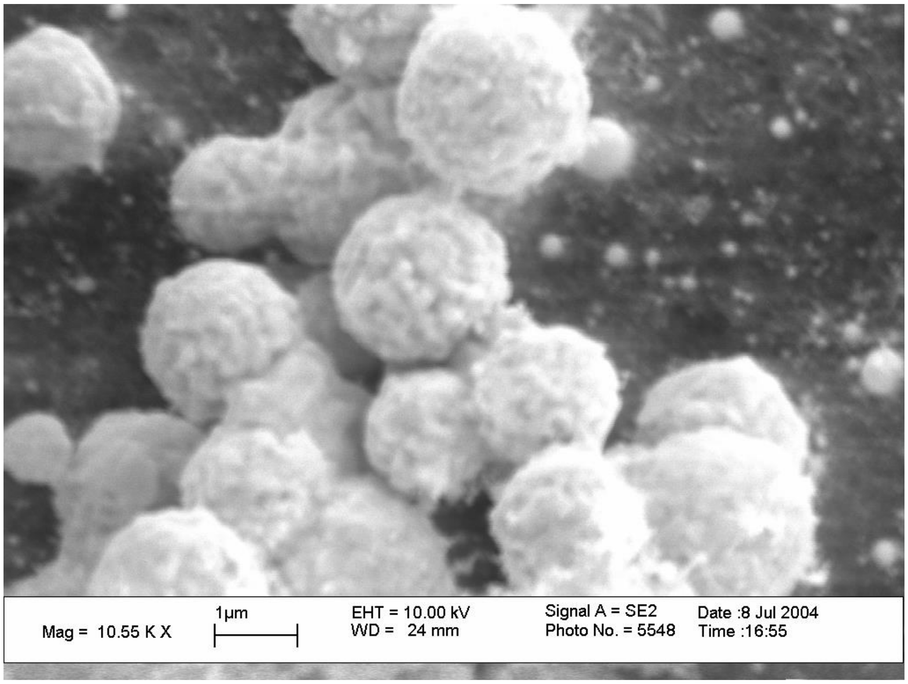

Figure 6: Ag microparticles

b. ABLATION CHAMBER DETAILS.

The chamber's walls are made by two crosses of borosilicate glass tube made by the glass shop (shown in Fig. 2). At the end of the long axis of the chamber, which is 2.47" long, we have fitted two funnel type stainless steel tubes so that the small side has the same diameter as the chamber glass tube, (0.748" OD and 0.645" ID). The larger opening of the funnel is welded to a 2" window frame so as we can fit a MgF-coated, quartz window. The coating is necessary for matching the index of refraction of the glass and the air to optimize the transmission of the 248 nm laser light. A UV-vis absorption spectrum was taken for the window and is shown in Fig. 7. The length of the long axis is also important for having a well focused beam at the center of each cross and a wide beam at the windows as to optimize the ablation at the center of the cells without damaging the windows by solarisation caused by exposure to high laser fluences. The volume inside the double ablation cell is small to keep a low gas flow rate in each ablation cell. The double ablation cell has one main flow inlet and one mainflow outlet that goes to the collection chamber. The gas flows into the ablation chamber are independently controlled by manual valves and flow meters with a scale of liter per minute. The required buffer gas cylinder is connected to the flow meters on one side with a pressure no more than 15 psi. There is one flow meter and valve for the main flow and another flow meter and valve for the coaxial flow. The coaxial flow has two independent inlets into the double ablation chamber. Each inlet is located in the same stainless steel jacket as the main flow. One jacket is in the first ablation region or first glass cross and another in the second ablation region or second cross. The main flow coming into the first ablation region, from the first aerosol generator goes along a thin stainless steel pipe into the center of the cell so it won't mix with the coaxial flow before the coaxial flow is flowing parallel to it. In this same jacket, the first coaxial flow is injected perpendicular to the main flow but it is given more than one inch in length inside the cell to collimate itself and flow parallel to the main flow before reaching the ablation region. In the ablation region the coaxial flow is important to keep the microparticles within the laser beam and prevent them from flowing to the back or front windows. If the microparticles reached the windows, the windows would become opaque to the laser and the ablation of the microparticles on the surface of the window would transmit heat to the windows, damaging their coatings.

It is desired that the laser goes from one window to the other without touching any other inside part of the chamber to avoid energy losses and ablation of any part close to the focus of the laser. The laser is focused into the double ablation cell by two cylindrical lenses. The first lens located right in front of the laser output has a focal length of 120 cm. This lens focuses the laser beam vertically. A second MgF-coated quartz lens with a focal length of 24 cm is located in front of the double ablation chamber in such a way that its focal point is in between the two ablation regions. Depending on the used materials, this 24 cm lens can be translated closer or further from the cell so as to increase the fluence in the first or second cell. To prevent any flow along the long axis of the chamber we installed two metallic cylinders along the two ablation cells in the direction of the coaxial flow. These metallic cylinders have slots on each side that are just wide enough to let the focused laser beam through but decrease the effective opening between the two cells. These slotted metallic cylinders have to be very well aligned to prevent them from laser ablating. Aligning is cumbersome but possible due to the visible ablation emission when the laser is not aligned. To provide a diagnostic for the alignment of the chamber, the first metallic cylinder was made from aluminum shim and the second one was made from stainless steel shim. In this way, in case of imperceptible misalignment, we would detect aluminum or stainless steel impurities in the Energy Dispersive Spectrometry, (EDS) sample analysis, letting us know what cell is the source of the impurities. Shim was used as so to minimize the thickness of the cylinder and leave the coaxial flow unperturbed. Before turning the aerosol generators on, we let the clean, main and coaxial flows reach a steady state. The volume inside the chamber in front of the window and along the long axis then reaches stagnation that prevents flow inside these cavities.

After the first ablation, the coaxial flow exits vertically through the exhaust located at the end of the first cell. The main center flow continues through a skimmer to the second aerosol generator in which the nanoparticles are mixed with microparticles. Just as in the first cell, the mixture of nano and micro particles are ablated and they remind confined in the center flow due to the second injection of clean coaxial flow. The second coaxial flow exits through its own independent coaxial outlet. Both coaxial flow exits are connected together to the same Edwards 80 mechanical pump through a 0.25” tube. The core shell structures exit the ablation chamber though the center exit of the second ablation cell. At this point, the second ablation cell center flow is coupled with the collection chamber.

The collection chamber consists of a three-fold cross made of borosilicate glass tubes. Each arm of the collection chamber cross has a well define purpose. The back port is for connecting the vacuum pump system, (Edwards 180 mechanical pump and roots blower in series), through a 2” valve and 2” vacuum pipe. The 2” vacuum valve is used for turning the vacuum inside the chamber on and off as quick as possible to avoid turbulent flows during transient opening and closing times, (transient times are quicker with wider valves because it takes less time to pump down.). The front port is sealed with a chemically inert, silicon rubber stopper coated with vacuum grease. It is only used for the liquid collection by replacing the blank stopper with one with a tight opening for introducing a long stainless steel needle for solvent injection. The port that is at the opposite side of the ablation chamber is used for introducing the electrodes and exchanging the samples for the electrostatic collection.

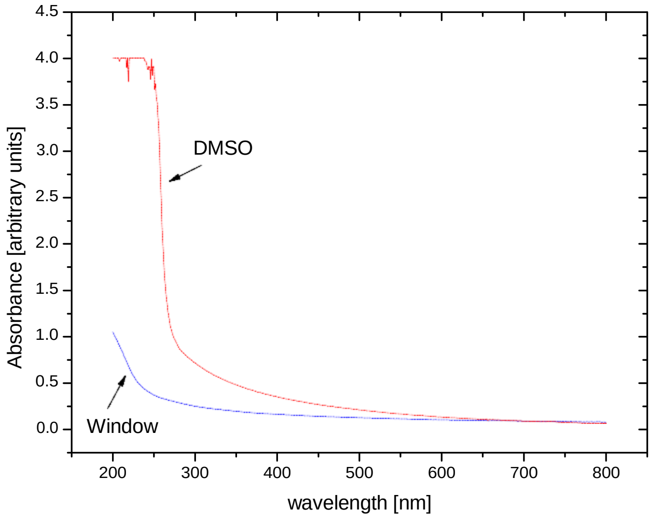

Figure 7: UV-Vis from window and DMSO: UV-Vis absorption spectra taken from Dimethyl Sulfoxide (DMSO) in a quartz cubet and quartz window of the chamber. The laser 248 nm light has a transmission of around 98% through the window.

In this case the chemically inert, silicon robber stopper is exchanged with one stopper with two tight holes in such a way that only Teflon-coated copper wires fit through them. The coated wires exit the chamber through this port in such a way that we can apply a high voltage to the electrodes. The top arm of the collection chamber cross fits a special chemically inert, silicon stopper that has been modified to serve as a sample holder. This stopper can hold long plates or trimmed microscope slides or wafers and hold them tight in place right in front of the nozzle for the supersonic impaction or behind the needle opening for the collection in solvent. The position and glancing angle of the substrate can be adjusted by rotating or pushing the stopper in place. The bottom port of the collection chamber is also used in the liquid collection to collect the nanoparticle solution as it spills down and is pulled by gravity.

c. NANOPARTICLE COLLECTION BY IMPACTION ON A SUBSTRATE.

We would like to answer the experimental question of how efficiently can we collect particles on a surface by directly impacting a nanoparticle aerosol onto a substrate. It is expected that particles with low masses would follow the flow lines and would never stick on the collection surface. We need to accelerate the particles to a velocity sufficient to transport them across the flow lines and reach the target surface. [16]

To accelerate the particles, we pass the aerosol beam through a supersonic nozzle. The aerosol jet is formed in a stagnation pressure P_o with temperature T_o and is passed through the nozzle with diameter d_n into a high vacuum chamber with pressure P_1 and temperature T_1. For a free jet expansion once the gas has gone through the nozzle, there is a strong shock called the Mach disc. The volume defined by the cone between the Mach disk and the nozzle is the volume where the nanoparticles are traveling faster than the speed of the sound and it is the region in which particles would not follow the flow lines. Our impaction collection needs to be done no further downstream than the distance from the nozzle to the Mach disk, (L_{Mach}), defined by, [17]

$$L_{Mach} = 0.67 d_n \sqrt{\frac{P_0}{P_1}} \qquad \textbf{- 1}$$

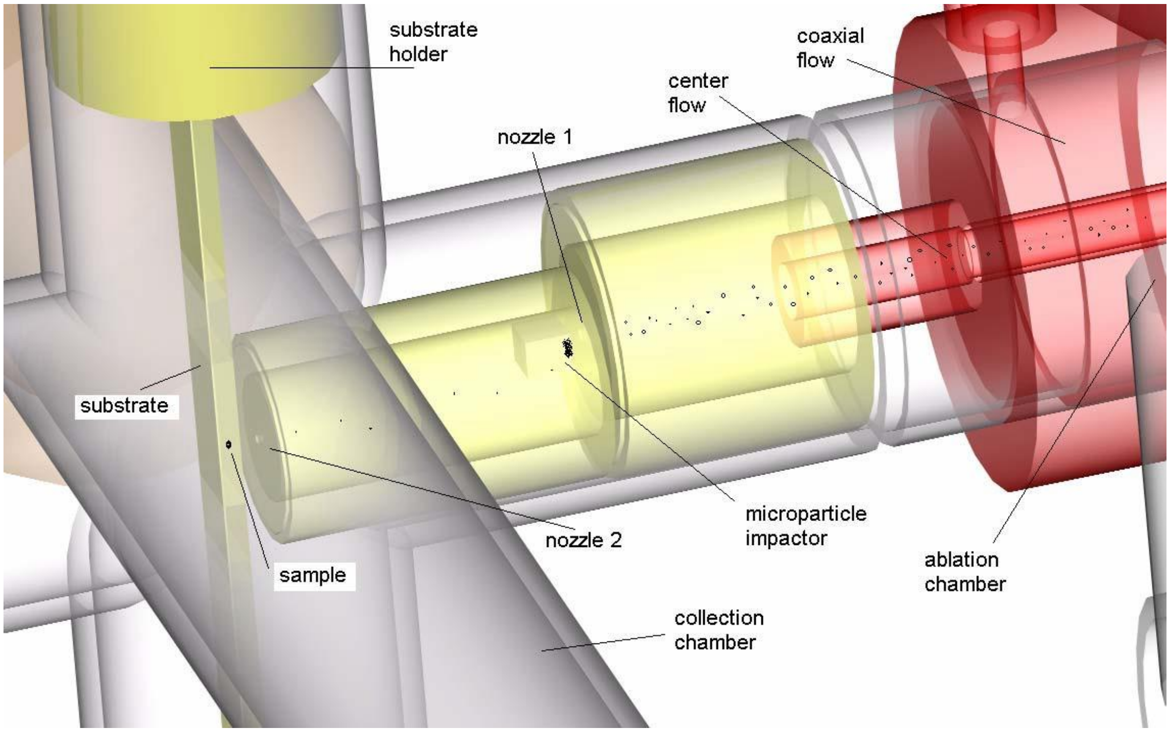

Figure 8: Collection by impaction that shows the main flow, microparticle impactor and nanoparticle substrate.

Collecting particles beyond the Mach disk makes it unlikely to succeed. This theory assumes that we are in the large nozzle Reynolds number regime, with large pressure ratios and a flat plate nozzle geometry. The particle velocity right after the flat plate nozzle and before the Mach disk is given by, [17]

$$V_{flow} = \sqrt{\frac{2\gamma}{\gamma - 1}\frac{kT_0}{m}} \qquad \textbf{- 2}$$

where $\gamma = C_p/C_v$ is the ratio of specific heats for the carrier gas, (He), *k* is the Boltzmann's constant and *m* is the gas molecular mass.

As the gas moves away from the nozzle, the pressure changes inside the Mach disk. [17] As a function of the distance from the nozzle this pressure P$_2$ is given by the equation,

$$P_2 = P_0 (3.26)^{\frac{-2}{\gamma-1}} \left(\frac{\gamma+1}{\gamma-1}\right)^{\frac{\gamma}{\gamma-1}} \left(\frac{\gamma+1}{2\gamma}\right)^{\frac{1}{\gamma-1}} \left(\frac{L-L_0}{d_n}\right)^{-2} \qquad \textbf{- 3}$$

where L$_o$ = 0.04d$_n$,

From Eq. 3 it is possible to calculate the density and temperature in this region as a function of distance from the nozzle using the isentropic expansion relation and ideal gas equation of state.

$$T_2 = T_0 \left(\frac{P_0}{P_1}\right)^{\frac{\gamma-1}{\gamma}} \quad \text{and} \quad \rho = \frac{P_2 m}{kT_2} \qquad \textbf{- 4}$$

We would like to know what is the final velocity of a particle after being accelerated as a function of its distance from the supersonic nozzle. The drag force accelerating a particle is given by the Stokes law:

$$F = m\frac{dv}{dt} = -\frac{3\pi\mu d_p v}{C_c} \qquad \textbf{- 5}$$

where *w* is the particle mass, μ is the gas viscosity, d_p is the particle diameter and *v* is the relative velocity between the gas and the particle velocity. C_c is the Cunningham slip factor that corrects the Stokes law (Eq. 5) for a discrete medium for particles on the order of the mean free path of the gas and it is given in terms of the Knudsen number K_n, the mean free path λ, and the temperature dependent viscosity $\mu(T)$ and the mean velocity of the gas molecules $V_m(T)$: [18]

$$C_c = 1 + K_n\left(1.257 + 0.4e^{-1.1/K_n}\right), \qquad \textbf{- 6}$$

where $$K_n = \frac{2\lambda}{d_p} = \frac{2}{d_p}\left(\frac{2\mu(t)}{\rho V_m}\right), \qquad \textbf{- 7}$$

and $$\mu(T) = \left(\frac{T}{T_0}\right)^{\frac{3}{2}}\left(\frac{T_0 + 1.47T_{boil}}{T + 1.47T_{boil}}\right). \qquad \textbf{- 8}$$

Solving for *v* from Stokes law, we get $v = v_0 e^{-t/\tau}$ where the relaxation time τ is defined as the ratio of the particle's momentum to the drag force acting upon it.

$$\tau = \frac{mv}{F_{drag}} = \frac{d_p^2 \rho_p C_c}{18\mu} \qquad \textbf{- 9}$$

From this equation we see that the denser the particle the longer it takes to reach a steady state velocity within the gas. If we substitute this last equation inside the equation for the velocity, then we can get the stream velocity before impaction on the surface.

When we collect by impaction we put a flat substrate perpendicular to the stream velocity after the nozzle. This stream obstruction causes a recompression of the aerosol right before the surface of the substrate. The flow lines curve eventually reaching 90 degrees with respect to the main stream and align parallel to the surface.

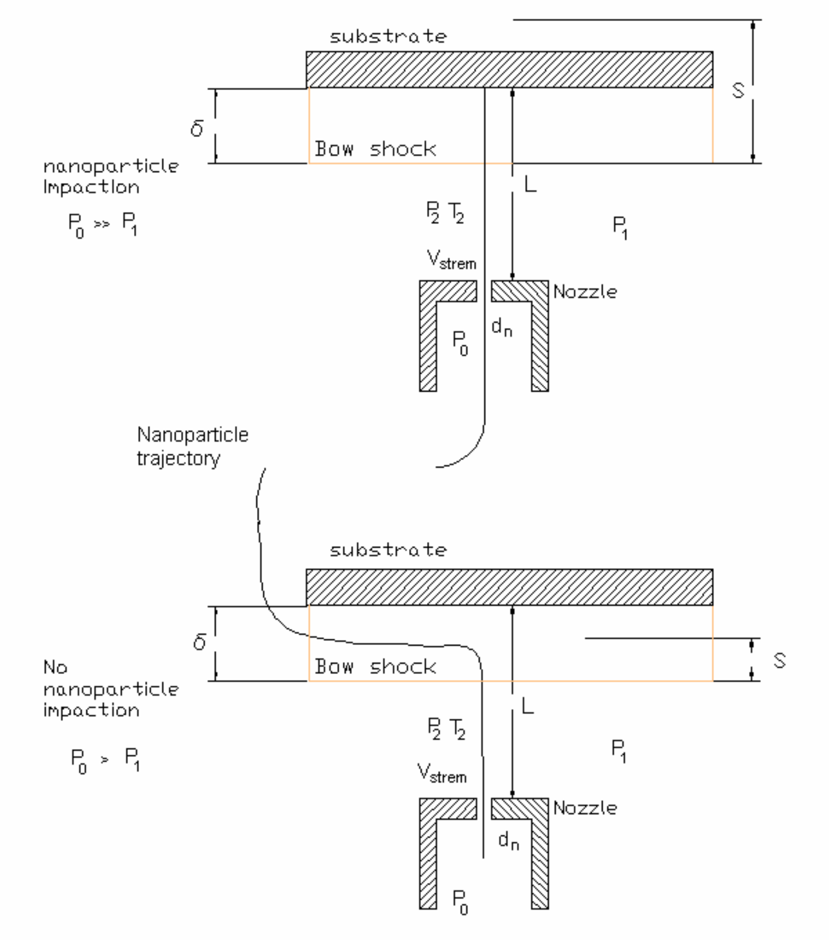

Figure 9: Two impactors with different conditions showing stopping distances S. The nanoparticle does not stop if the stopping distance is smaller than the distance from the substrate to the bow-shock.

This region of parallel flow lines to the surface has a characteristic thickness δ that is defined for the limit of high pressure difference and is given in terms of the nozzle flat surface distance L by

$$\frac{\delta}{L} = \frac{\gamma - 1}{2(\gamma + 1)} \qquad \textbf{- 10}$$

which is valid in the limit $L < 0.67\ L_{Mach}$

This distance δ is measured from the collection substrate in direction of the nozzle, and is the distance in which free jet starts to decelerate right before the impaction.

This parameter δ is known as the bow shock. The free jet of nanoparticles will completely stop after the bow shock at a characteristic distance S given by $S = \tau_2 V_{stream}$ where τ_2 is the relaxation time at the plate conditions (P_2, T_2). S is known as the stopping distance and it is calculated in Mathematica and plotted in Fig. 10. In this calculation, d_n is 100 µm, L is 1 mm, P_0 and P_1 are one atmosphere and 100 mTorr respectively, T_0 and T_1 are 300K, γ and T_{boil} for He are 1.67 and 4K respectively, the He viscosity is $2\text{x}10^{-5}$ Nsm^{-2} and we solve the velocity from the Stokes equation for $t = 7\tau$, (when we have reached equilibrium conditions). The densities of the materials are reported in a later table. In this figure, the bow shock is a constant horizontal line. All nanoparticles with stopping parameters below this horizontal line won't be collected by impaction. The minimum particle size that would be collected is given by the intersection of the horizontal line and the S curve for each material. The actual values will be reported later in the chapter on NP size reduction.

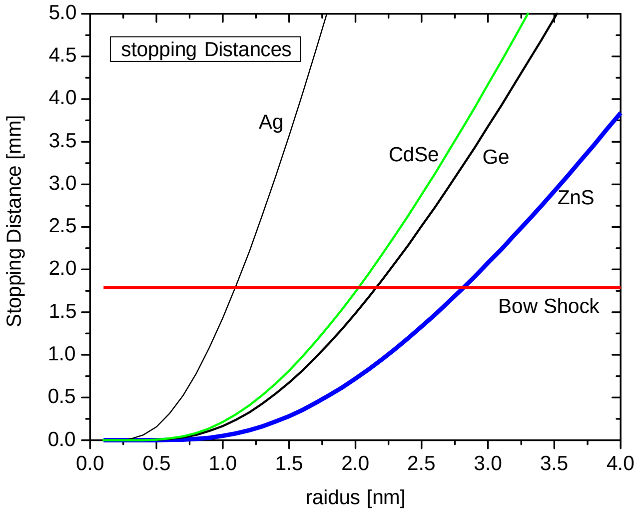

Figure 10: Calculation of the stopping distances. Intersection of the curve and the bow shock line gives the smallest particle size that can be collected by impaction.

d. IMPACTION INTO LIQUIDS.

To impact nanoparticles in liquid we used the supersonic nozzle that requires the formation of a silence cone (the so called region where the particles move faster than the speed of the sound of the media), and pressures on the order of mTorr. This implies that any solvent that we use for impaction has to have a low vapor pressure. High vapor pressure materials vaporize in a matter of minutes inside our vacuum chambers. Another restriction for the solvent is the surface tension. The liquid is pumped into the vacuum chamber by a syringe outside the chamber. At the end of the needle that connects the inside chamber with the syringe outside, a bubble is formed. To have high concentration of nanoparticles without liquid recirculation, the incoming bubble is kept still in front of the supersonic nozzle for a couple of seconds as shown in Fig. 11. If we keep pushing the liquid in then the nanoparticle loaded bubble will slide down the glass substrate that is behind it. The nanoparticle collection works better when the nanoparticle are impacted on the surface of the liquid before they impact the glass surface behind. Several common solvents were ranked to find the best solvent. Table 1 shows some of these parameters. Water has the best surface tension of the studied liquids and it is biocompatible, unfortunately it has a moderate vapor pressure but unfortunately it freezes inside our vacuum chamber, clogs the needle and therefore stops any further injection. Solvents that are

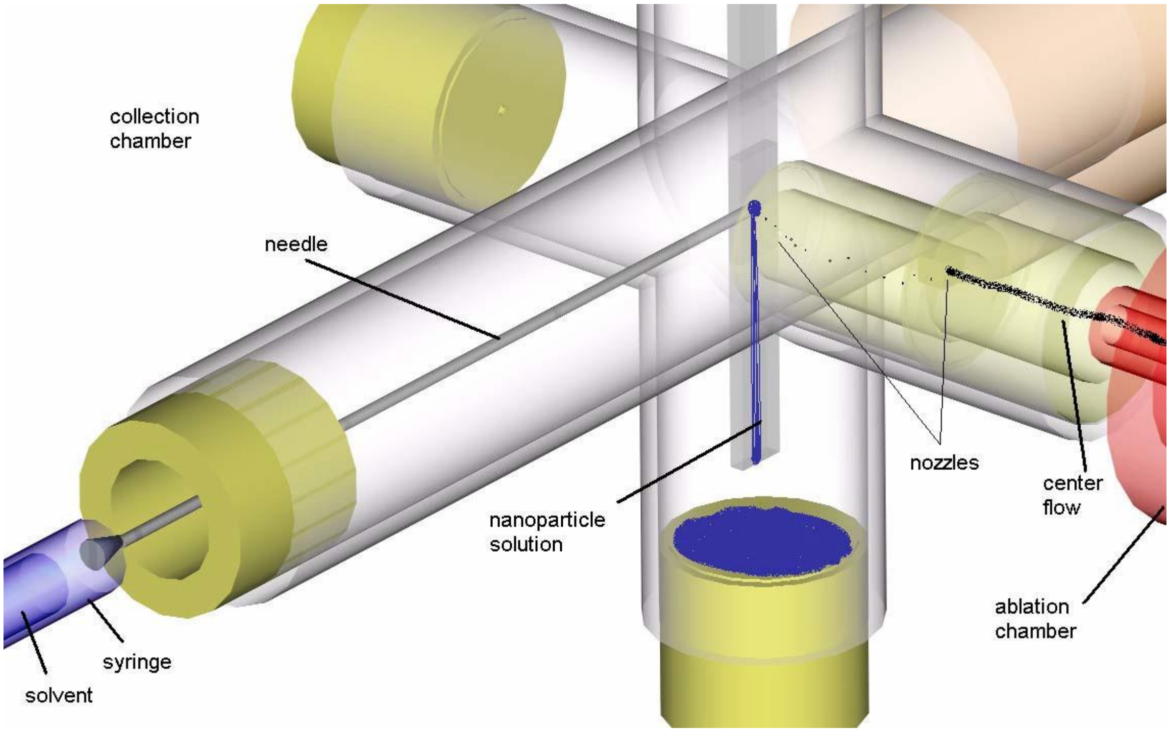

Figure 11: Liquid collection chamber

ideal for spectroscopy studies such as benzene and hexane, have vapor pressures that are high enough to vaporize the solvent as soon as it gets inside the vacuum. Chloroform was very desirable because it is commonly used in chemically grown quantum dot measurements but it is also vaporized inside the impaction chamber. The only three commonly used solvents with low vapor pressure were dymethyl sulfoxide (DMSO), nonanoic acid and octanol. Of these solvents, DMSO has the highest surface tension and octanol the lowest. Previous unpublished work done by William Nichols, suggest that no highly fluorescent quantum dots were seen in nonanoic acid. Based on this investigation DMSO, was used for our research. To be sure that we had nanoparticle collection into liquids, some samples were poured into ceramics and baked to vaporize the DMSO. Thin films of dry nanoparticles were seen deposited at the bottom of the ceramic.

Substance	Vapor Pressure [Torr]	Surface Tension [pascals]
Toluene	22	
Water	17.54	7.8
Chloroform	156.05	
Hexane	130	
Benzene	75	
DMSO	0.42	4.3
Nonanoic Acid	1	3.3
Octanol	0.15	2.8
Propanol	32	

Table 1: Vapor pressure and surface tension for some common solvents

e. ELECTROSTATIC COLLECTION

For collecting dispersed nanoparticles on quartz substrates, we put a potential difference across the trajectory of the main gas flow. Parallel to the main flow we put two copper electrodes that were 6.5 mm apart from the axis defined by the length of the inlet nozzle. The gas flow is unaffected when there is no high voltage applied to the electrodes that are 1.3 cm apart from each other. With no high voltage the flow moves parallel to the electrodes. When a voltage is applied to the electrodes any charged particle will be deflected and pulled towards the opposite charged electrode and remain attracted until the charge is eliminated by electron-ion recombination or by contact with the electrode. The quartz substrate was cleaned by rinsing it in distilled water and sonicated for 5 minutes in acetone.

The forces that a charged nanoparticle experience in the flow are the drag force, the electrostatic force and the gravitational force. They have been calculated previously [19] and after neglecting the gravitational force the resulting equations for the position of the particles in the plane of the electrodes and the inlet nozzle are detailed below.

In the direction of the main flow, the position of the particle after ionization is $x = tV_g$. In the vertical direction along the direction from the nozzle to the electrode, the position is described by

$$y = \frac{K_2}{K_1^2}(K_1 t + e^{-K_2 t} - 1) \qquad \textbf{- 11}$$

where

$$K_1 = \frac{9\mu}{2\rho C_c r^2} \quad \text{and} \quad K_2 = \frac{3qE_y}{4\rho\pi r^3} \qquad \textbf{- 12}$$

Where r, ρ and q are the radius, density and charge of the particle, E_y is the electric field in the vertical direction and C_c is the Cunningham factor introduced in Eq. 6 .

The drag force computation is based on the assumption that the particles are spherical. If the particles start to make chains, the drag force and the final y position change dramatically. On the other hand, since the chaining of the particles is directly related with ion-electron recombination at longer distances, downstream we will have recombination and chaining. At these longer downstream distances the equation for the position y must be modified for chains of random charge and geometry. Nevertheless, the trend is that the more massive chains and particles that are partially charged are attracted to the electrode at further downstream locations.

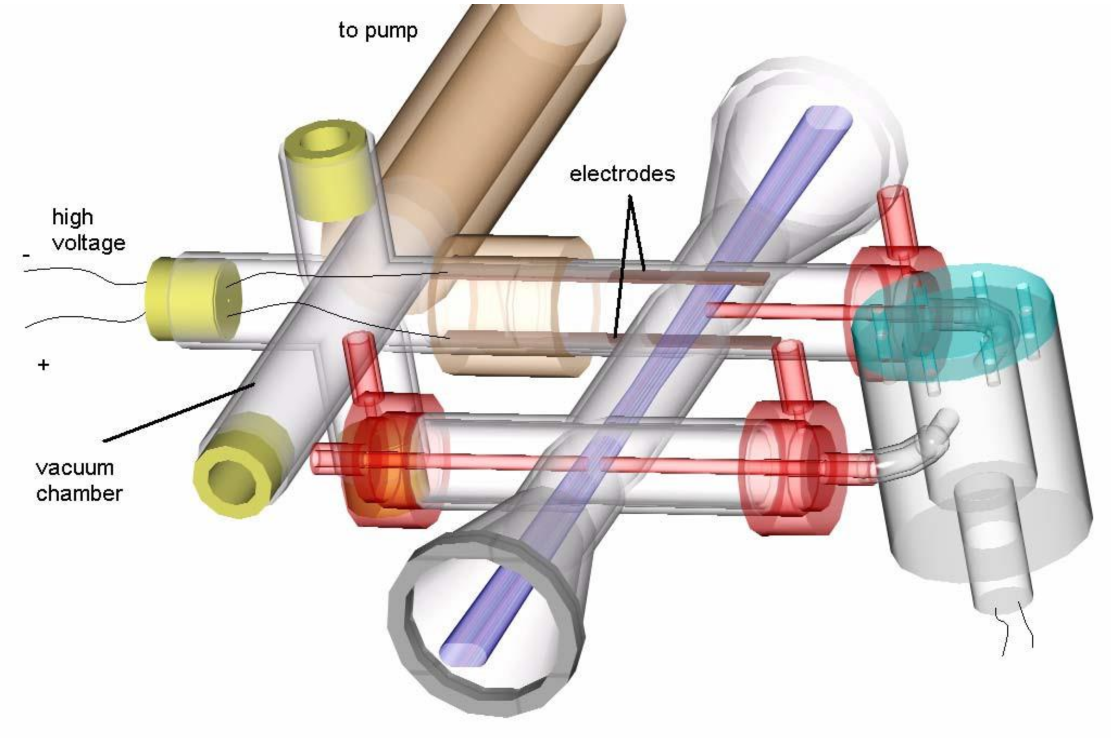

Figure 12: Electrostatic chamber configuration. First aerosol generator is not shown for clarity.

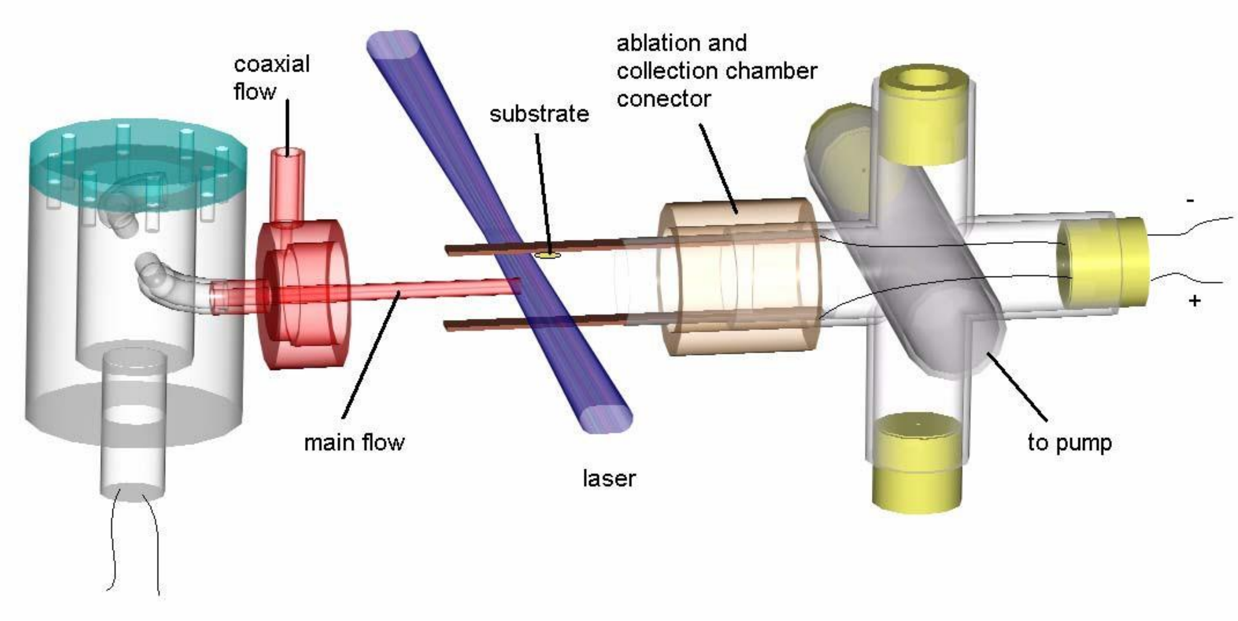

Figure 13: View of the electrodes and position of the sample on top of the electrode.

For the electrostatic calculation plotted, the applied voltage was 500 V, the separation between the electrodes was 13 mm. The velocity of the main flow was 1 ms^{-1}. The figure shows 4 different materials for which bulk densities were used and each material was run for two particle sizes, except for ZnS that didn't evaporate in the double ablation experiments.

The experimental selectivity is not as sharp as the one resulting from the simple simulation due to several reasons. First, the ablation or ionization region are not only one point, but a volume that has a cross section that on the plane of the simulation is given by our fluence area. All the ionized particles in this area will travel to the same electrodes and depending on their original positions in the small volume they could arrive at the same place on top of the electrode without having the same mass. Second, despite the effort of keeping steady flows for optimizing the ablation and synchronizing the first and second ablations, when the main flows are open a few seconds of turbulence pass before we can stabilize the flows in the correct positions. The temporary turbulence deposits random sized particles on our electrodes and samples. Even when the aerosol feeders are turned off, there is a small amount of nanoparticles deposited on the inlet tubes and nozzles that can easily be perturbed during the turbulent flow collection. The bad selectivity produced by this turbulence is minimized by making the turbulence time only a small fraction of the collection period. The samples are made in such away that the nanoparticle collection during the steady state flow is several times longer than the transient turbulent initial and final time when we open and close the clean gas valves for aerosol control. The high voltage is only turned on after we have reached stationary conditions to avoid collecting the wrong particle sizes. Experimentally we do observe a size selectivity that is not as sharp as that in the simulation but we can see a clear separation between well-ablated nanoparticles, unablated microparticles and large amorphous evaporated particles, (particles that are not properly ablated due to feedstock agglomeration or particles shadowing behind microparticles at the ablation region).

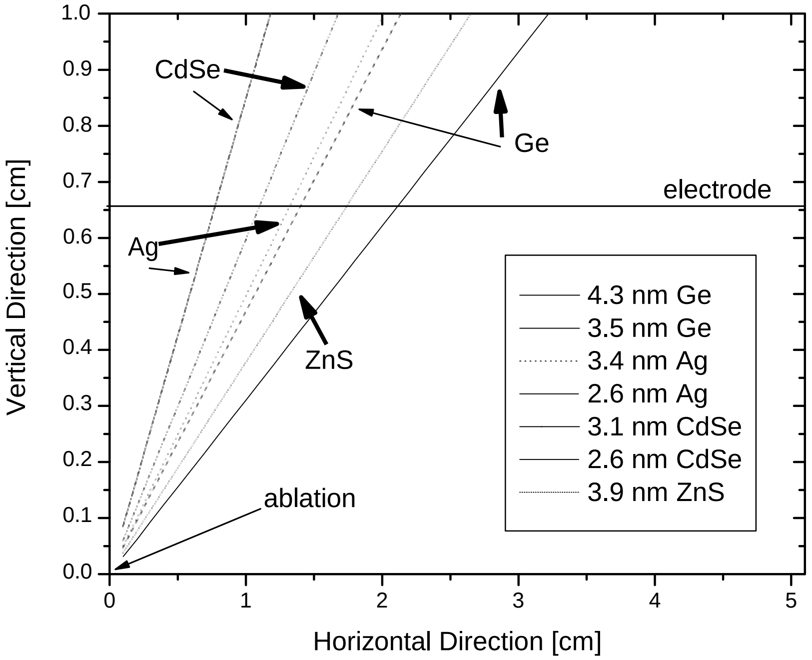

Figure 14: Calculated deflections for the electrostatic collection of nanoparticles.

The nanoparticle ablation zone is located at the origin. For each material, tick arrows represent trajectory of singly ablated nanoparticles. Thin arrows are double ablated nanoparticles. Electric field is 500 V.

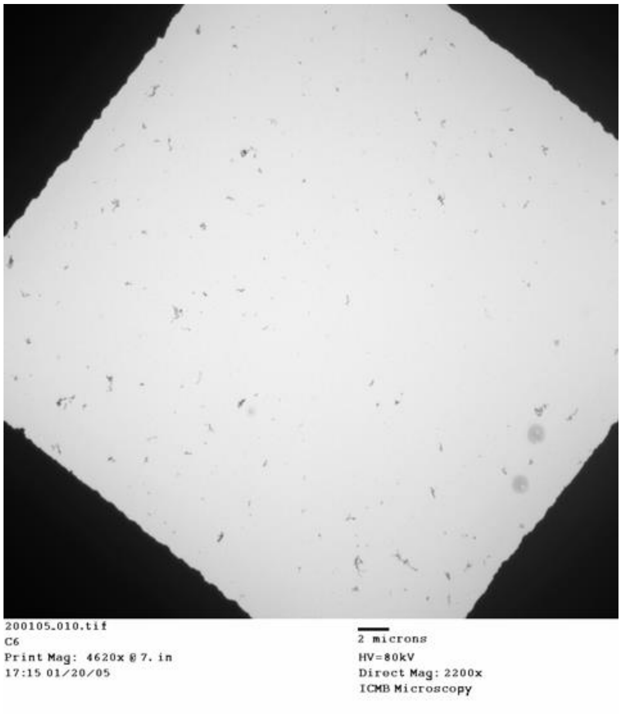

Figure 15: TEM micrographs of samples taken at 6 mm downstream from ablation zone

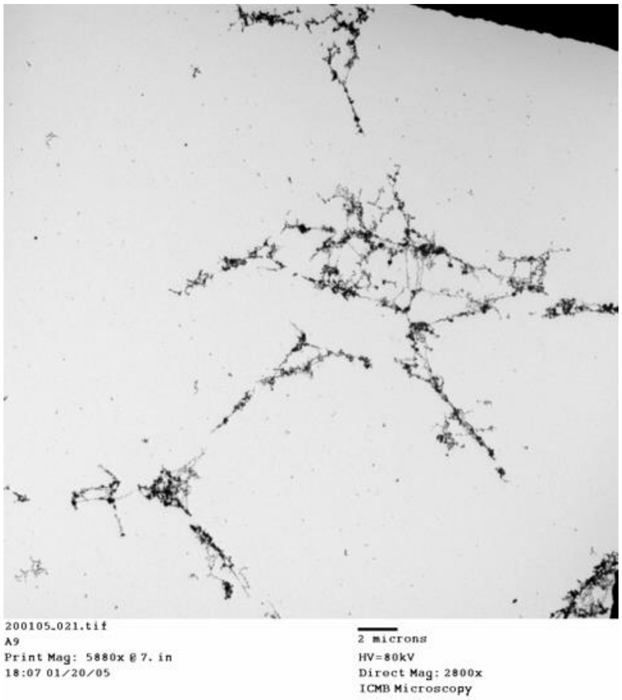

Figure 16: TEM micrographs of samples taken 10 cm downstream from ablation zone.

3. Theory

a. QUANTUM CONFINEMENT

Inside a semiconductor, when we excite an electron from the valance band to the conduction band it leaves a hole behind. Depending on the type of material, the electron and hole will feel each other through Coulomb interactions that are directly proportional on the number of free electrons that screen this interaction. The lower the temperature the less the screening and the more stable the couple. The hole-electron pair can be treated as a single entity called the exciton. Because of the Coulomb nature of their interactions the further away the electron is from the hole, the weaker the interaction.

In the bulk, the exciton can be described in the same way the hydrogen atom is described with the Schrödinger Equation with the Hamiltonian, H, given by

$$H = -\frac{h^2}{2m_p}\nabla^2{}_p - \frac{h^2}{2m_e}\nabla^2{}_e - \frac{e^2}{\left|r_p - r_e\right|} \qquad \textbf{- 13}$$

defined for the hydrogen atom. That leads to

$$H = -\frac{h^2}{2m_e^*}\nabla^2_e - \frac{h^2}{2m_h^*}\nabla^2_e - \frac{e^2}{\varepsilon\left|r_p - r_e\right|} \qquad \textbf{- 14}$$

for the exciton in the bulk, where we have substituted the mass of the electron and the mass of the proton for the effective masses of the electron and the hole in the bulk material and have considered the dielectric constant ε for the coulomb interaction inside the semiconductor.

Eq. 14 can be separated in two equations, one for the energy of the center of mass of the system and another for the binding energy.

$$H = -\frac{\hbar^2}{2M}\nabla_R^2 - \frac{\hbar^2}{2\mu}\nabla_r^2 - \frac{e^2}{\varepsilon r} \qquad \textbf{- 15}$$

where *H* is the total Hamiltonian, the first term corresponds to the center of mass kinetic energy, (where *M* is the total mass of the system located at the position denoted by the radius *R*) and the last two terms are only dependent on the relative position, r, that separates the electron from the hole and where μ is the reduced mass.

The Schrödinger equation with this Hamiltonian can be solved for a crystal in terms of the Bloch waves for wave vectors k near 0. This is only possible if the electron and hole are separated a distance longer than the crystal lattice constant. When this happens the excitons are know as of the Mott-Wannier exciton type.

If we continue talking about the exciton in terms of the hydrogen atom approximation we can define the equivalent Rydberg energy (Ry^e) and Bohr radius (a_B^e) for the exciton given by

$$a_B^e = \frac{\varepsilon\hbar^2}{\mu e^2} = \frac{\varepsilon m_e^*}{\mu} a_B \qquad \textbf{- 16}$$

and

$$Ry^e = \frac{e^2}{2\varepsilon a_B} = \frac{\mu e^4}{2\varepsilon^2\hbar^2} = \frac{\mu}{m_e^*\varepsilon^2} Ry \qquad \textbf{- 17}$$

where a_B is the Bohr radius and Ry is the Rydberg energy of the hydrogen atom. In a semiconductor ε has values of around 10 and the effective masses are around half the mass of the electrons. This means that the semiconductor excitons are 20 times larger than the hydrogen atom.

In a quantum dot that has a size on the order of a_B^e the exciton can’t keep moving freely and the kinetic energy of the exciton becomes discrete and has to be solved as a particle in a spherical box problem is solved in quantum mechanics. The solution for this kinetic energy levels is

$$H_R = -\frac{h^2 X_{nl}}{2Ma^2} \qquad \mathbf{-\ 18}$$

where X_{nl} are the zeros of the Bessel function. [20]

Then, by substituting H_R for the center of mass kineting energy in the Hamiltonian, the final form for the exciton’s absorption energy in the QD is

$$E_{nl} = E_g + \frac{h^2 X_{nl}^2}{2Ma^2} - \frac{\mu e^4}{2\varepsilon^2 h^2 l^2} \qquad \mathbf{-\ 19}$$

and with a correction in first order perturbation theory for the Coulomb interaction this absorption energy changes into.[21]

$$E_{1s1s} = E_g + \frac{h^2 \pi^2}{2\mu a^2} - 1.8\frac{e^2}{\varepsilon a} \qquad \mathbf{-\ 20}$$

which has been evaluated for the most visible 1s1s exciton level, (1s electron state and 1s hole state). Eq. 20 is called the parabolic approximation but it doesn’t take into account the influence of the other bands far away from the k = 0 zone. This approximation will be used to analyze the fluorescence results. For degenerate valence bands seen in some semiconductors, the Luttinger-Kohn model is a better approximation based on two more parameters that take into consideration light and heavy holes. [22]

b. NANOPARTICLE SIZE CHANGE DUE TO EVAPORATION.

From the Clausius-Clapeyron equation that describes the pressure change in the coexistence curve of the interface of a gas and a solid we get.

$$\left(\frac{dP}{dT}\right)_{coex} = \frac{\Delta h_s}{T\Delta V} \qquad \text{- 21}$$

where Δh_s is the change in energy and ΔV is the change in volume. If we assume a low gas density we can substitute the change in volume for the ideal gas equation of state.

$$\left(\frac{dP}{dT}\right)_{coex} = \frac{P\Delta h_s}{RT^2} \qquad \text{- 22}$$

by solving for each of the two variables *P* and *T* at each side of the equation we can integrate both sides independently on *P* and *T*,

$$\int\left(\frac{dP}{p}\right)_{coex} = \frac{1}{R}\int\frac{dT\,\Delta h_s}{T^2}, \quad \text{with solution} \quad P_c = Ae^{-\frac{\Delta h_s}{RT_c}} \qquad \text{- 23}$$

that describes the behavior of the pressure as the function of the temperature along the coexistent curve in terms of the initial condition $A(P_o, T_o)$.

On the other hand, if we assume that the atoms that escape the surface are moving with average thermal velocity of the gas then the velocity of the atoms is

$$V_a = \left(\frac{8kT}{\pi m}\right)^{\frac{1}{2}} \qquad \text{- 24}$$

where m is the mass of the atom.

The continuity equation that conserves the number of atoms in the system says that the change in the radius of the nanoparticle (*a*) is proportional to the number of atoms in the gas phase per unit volume and their velocity, therefore, the continuity equation takes the form.

$$\rho_s \frac{da}{dt} = \rho_v V_a \qquad \textbf{- 25}$$

where ρ_s is the density of the solid and ρ_v is the density of atoms in the vapor phase which can also be obtained by solving the ideal gas equation of state for the volume and dividing both sides of the equation by the mass of the atom.

$$\frac{nRT}{mP} = \frac{V}{m} = \frac{1}{\rho_v} \qquad \textbf{- 26}$$

From the continuity equation (Eq. 25) we solve for the change in radius and we substitute the atom mean velocity and the density of the vapor phase to get,

$$\frac{da}{dt} = \frac{\rho_v V_a}{\rho_s} = \frac{Pw}{nRT\rho_s}\left(\frac{8kT}{\pi m}\right)^{\frac{1}{2}}. \qquad \textbf{- 27}$$

We finally can substitute Eq. **23** for the pressure at the coexistent curve into Eq. 27 to find the change in particle radius as a function of temperature.

$$\frac{da}{dt} = \left(\frac{1}{\rho_s} A\left(\frac{8m}{\pi k}\right)^{\frac{1}{2}}\right)\frac{1}{T\sqrt{\ }} e^{-\frac{Cs}{kT}} \qquad \textbf{- 28}$$

Where the constant in parenthesis is dependent only on the melting point of the material. Notice that the sublimation energy per atom is substituted by the energy required for the atom to leave the surface of the particle which is the cohesive energy C_s The initial condition *A* is obtained by using Eq.23 for initial condition P_0 and T_0. Eq. 28. Is used in Eq. 30 to calculate the reduction in radius of double ablated nanoparticles.

c. THERMIONIC ELECTRON EMISSION

At high enough temperature, thermally excited electrons are more likely to tunnel the energy barrier and get emitted even when excited by photons of lower energy than the barrier. At even higher temperatures and without the photon excitation an electron will be emitted according to the Richardson-Dushman equation for the electron current density *j*.

$$j = A_R(1-\eta)T^2 e^{-w/kT} \qquad \textbf{- 29}$$

where $A_R = 120$ Acm^{-2}K^{-2}, η is the reflectivity of the electron at the surface barrier (1-5%) and w is the work function. Nevertheless, after comparison, this cooling term is negligible with respect to collision cooling or evaporation.

d. MIE THEORY.

In this section we try to understand what fraction of the incident light on a nanoparticle is scattered and absorbed. The LAM process in which a microparticle is ablated by ionization and generation of a shockwave was simulated and discussed earlier. Here we focus on LAM generated nanoparticles that are irradiated with light after they are formed. The scattered light is limited to a single spherical particle. The interactions with the background gas or substrates are not considered in these studies.

In a paper published by Mie [23] in 1908, he solved the Maxwell's equations rigorously assuming a plane monochromatic wave incident on a homogenous sphere of any diameter or composition. He obtained the resulting electromagnetic field or diffraction in the form of an infinite series. A way to derive this formula and to relate it with the light pressure on a conducting sphere calculated by P. Debye is described in detail by M. Born and E. Wolf. [24] The theory of Mie can only be applied for single spheres or collection of spheres that are separated by a long distance in comparison to the wavelength of the incident light.

An extension to the Mie calculation to a core and shell structure with a spherical shape is found in ref. [25] It is important to notice that all these calculations are classical and they don't take into account light emitted from the particle through nonlinear processes such as fluorescence.

The fluorescent light that we experimentally study in this dissertation comes from the quantum mechanical description of electron confinement and discrete energy levels of the exciton inside the nanoparticle as it is represented as a quantum well. Therefore, the Mie theory calculations are mostly useful to understand the classical absorption of light and calculate how the energy is dissipated. On the other hand, the plasmon resonances of the nanoparticles help us to predict where to expect spectral peaks on our experimental studies and how to separate fluorescence from scattered light coming from Mie theory.

For the materials that we study in this dissertation we have calculated the Mie absorption cross section as a function of particle size and excitation energy. The particle size dependence is useful for computing the nanoparticle evaporation. The excitation energy calculations are useful to know how our measured spectra overlaps with the Mie intensities.

The energy of the 248 nm excimer laser is high enough to assume that most of the incident light of the pulse sees an ionized particle. The ionization time is commonly known to be two or more orders of magnitude faster than the duration of the excimer laser pulse used in these experiments (FWHM of 18 *nsec*). The way that charged nanoparticles are studied by using Mie theory, is by adding a free electron cloud around the core single nanoparticle. This cloud is a free electron shell that is physically characterized by is thickness and its own free electron index of refraction. [26]. The equations for Mie scattering of core-shell nanoparticles will be presented in the chapter of the evaporation of nanoparticles.

The energy calculations were run for particles of different sizes as we expect plasmon shifts for each experimentally studied particle size.

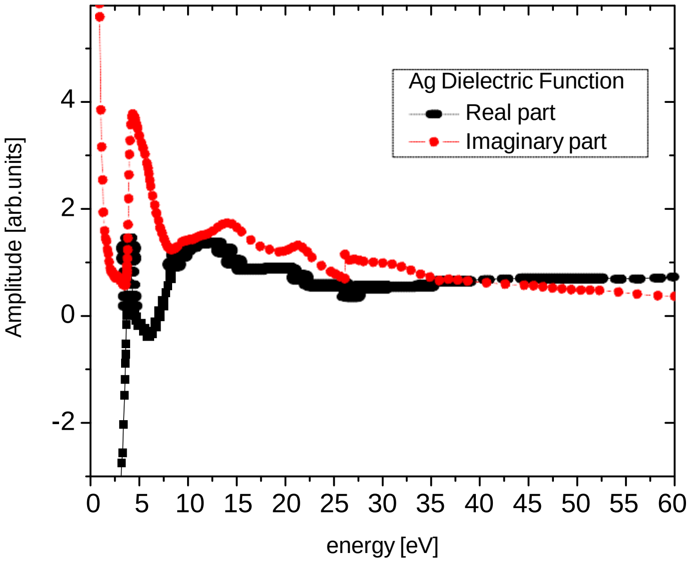

Figure 17: Complex dielectric function of Ag used in the simulation. circles are the imaginary part. Squares are the real part.

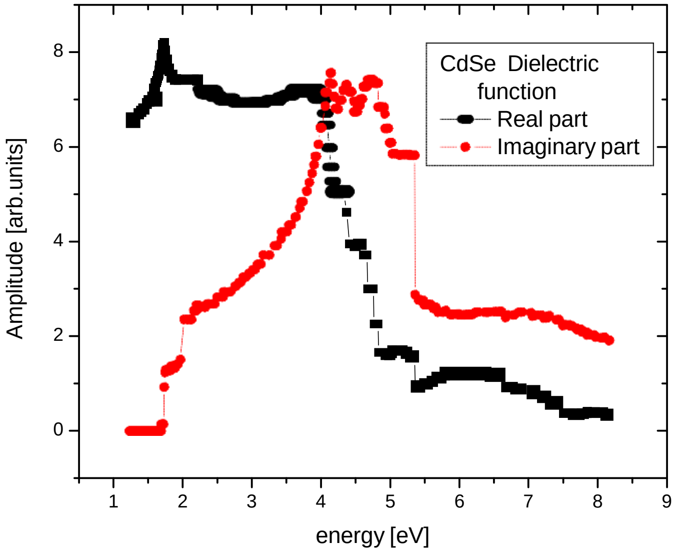

Figure 18: Complex dielectric function of CdSe used in the simulation. circles are the imaginary part. Squares are the real part.

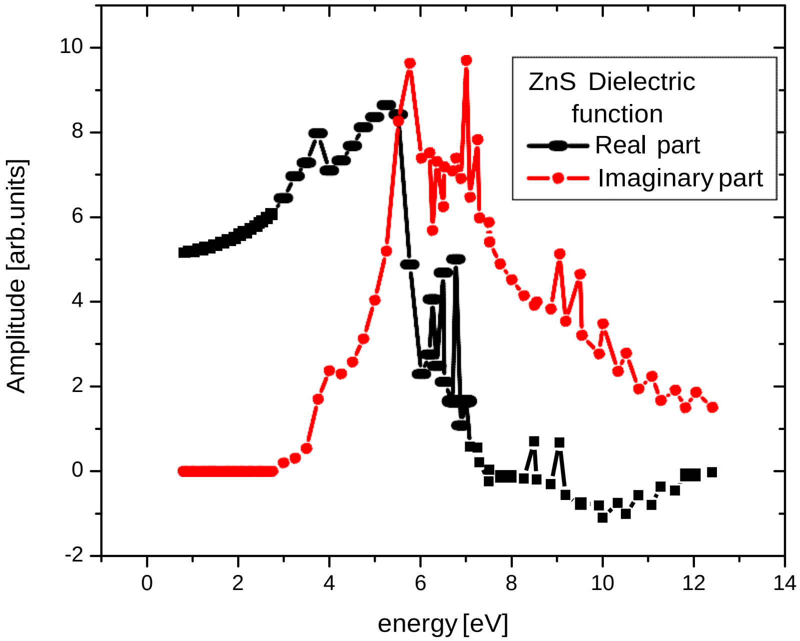

Figure 19: Complex dielectric function of ZnS used in the simulation. circles are the imaginary part. Squares are the real part.

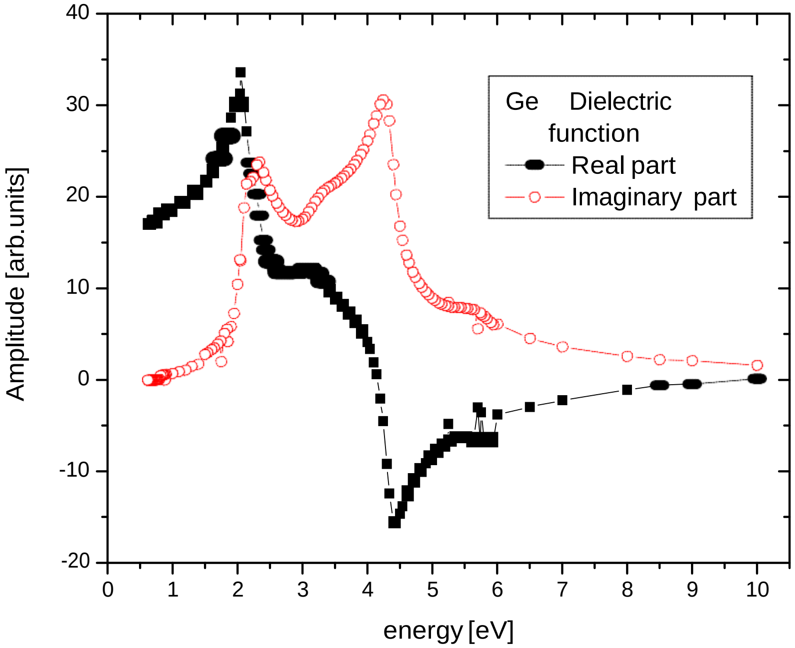

Figure 20: Complex dielectric function of Ge used in the simulation. Circles are the imaginary part. Squares are the real part.

Mie Model type	Charge [electron units]	δ [nm]	a_k [nm]
Core/shell	+1000	0	0.28
Core/shell	+20	0	0.13
Core/shell	+1	0	0.13
Core/shell	-1	0.12	0.13
Core/shell	neutral	0.045	0.28
Single Core	0	0	0

Table 2: Parameters used in the simulation for the core/shell [26] and single core model.

The parameters reported by Kresin et al., are for charges +1,-1 and neutral particles. In our work we extrapolate these results to explore what happens to the core/shell model for charges of +1000 and +20. For all positively charged NPs, the spilling of the electrons (δ) is assumed to be 0 and the overlap of the s-d level represented by the shell with thickness a_k is 0.13. The value of $a_k = 0.28$ for the +1000 charged NP was maximized and given by the maximum value for s-d level overlap (a_k) reported by Kresin et al. As a result of this, it was noticed that changing the charge state of the nanoparticle did not play a significant role in the calculation for the absorption cross section in comparison with the change in the shell thickness. Despite the change in the charge state by three orders of magnitude, the absorption cross section didn’t change much.

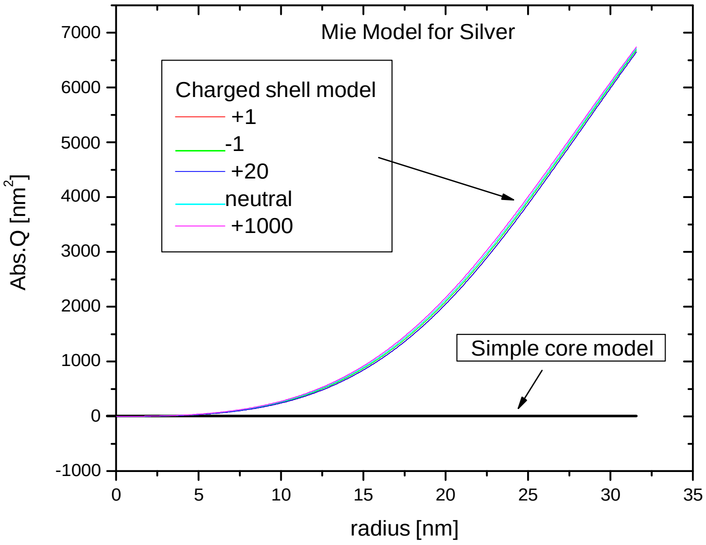

Figure 21: Particle size dependence of the Mie absorption for silver

The absorption Mie cross section shows the same radius cubic dependence for all materials. Here we show the values for Ag that are shifted by the ionization represented as a shell in the Mie model. As seen in Fig. 22, the highest values are always for charges that need thicker shells. In decreasing of amplitude we first have the +1000 charged particle, then we have the neutral particle, then the -1 particle followed by the +20 particle and the +1 particle. The smallest cross section is for the particle that is simulated without shell. All plots show the cubic dependence in the radius. All core radii for Ag are the same 3.35 nm size.

The absorption cross section cubic dependence is clearly seen for small particles. A particle with 0.5 nm in radius has around 40 silver atoms and its absorption cross section is increased multiple times depending on the charge state of the particle.

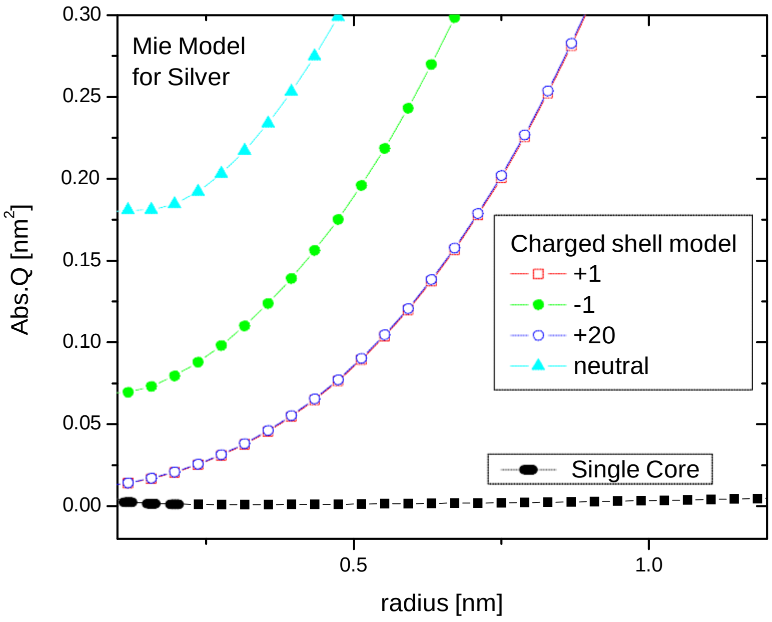

Figure 22: Radial dependence of silver at smaller scales.

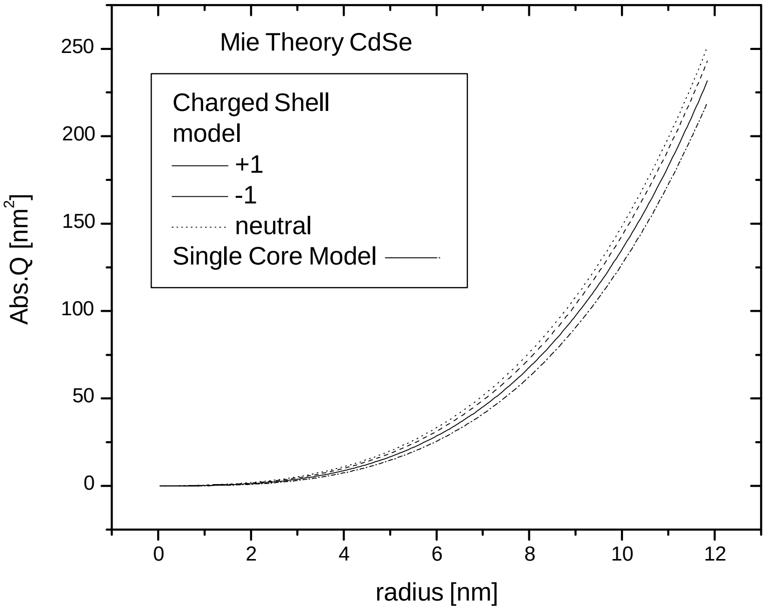

Figure 23: The same radial dependence as for silver is shown here for CdSe

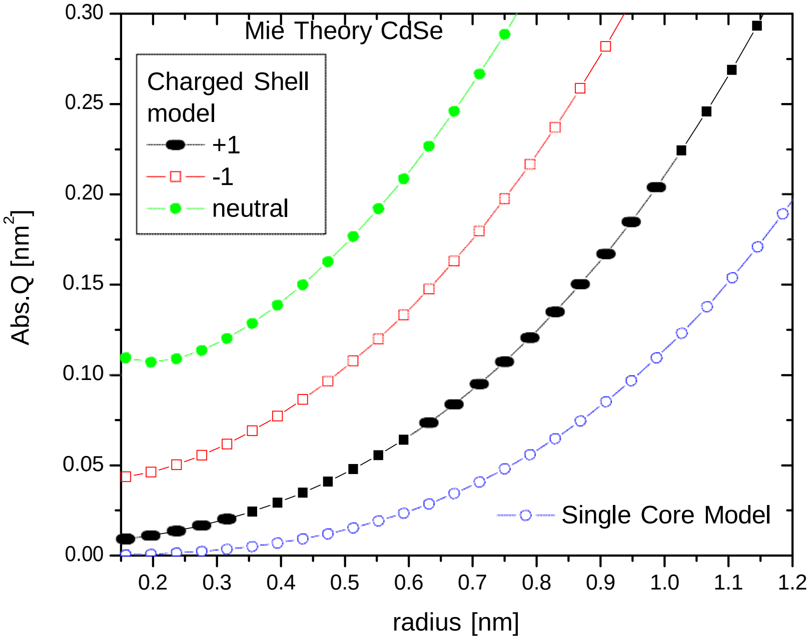

Figure 24: View of Fig. 23 at smaller radii shows higher absorption for neutral particles.

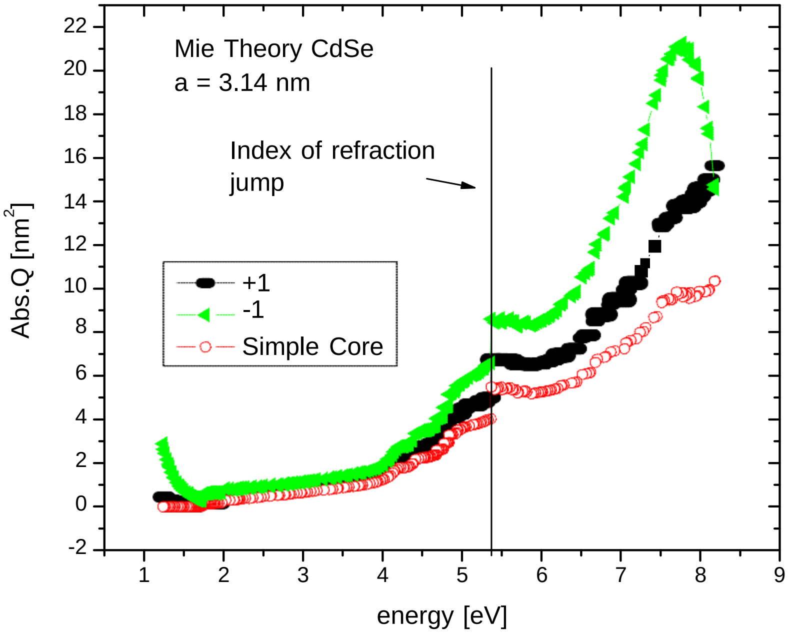

Figure 25: Charge dependence of the experimentally observed size of the CdSe NP

We can see in all our material radial dependences that the absorption at small sizes depends dramatically on the model used. In all the materials, the neutral particle calculated with the ion shell model denoted by “neutral” is above the charged particle simulation. In contrast, the single core model with no ion shell shows that a neutral particle has an absorption curve that has always the lowest calculated absorption.

The CdSe simulation as a function of energy presents a drop in the absorption that reflects the drop in the index or refraction available data as seen in Fig.18 and it should not be interpreted as resonance. For the 0.5 nm size for the CdSe NP, we can observe a resonance around the 2.5 eV peak. This resonance shifts to a 1.5 nm peak when the particle is twice as large. The relative intensity of this resonance is maximum at around 1 nm of the particle size. For larger nanoparticles this resonance is negligible with respect of the rest of the absorbed light located above 5 eV.

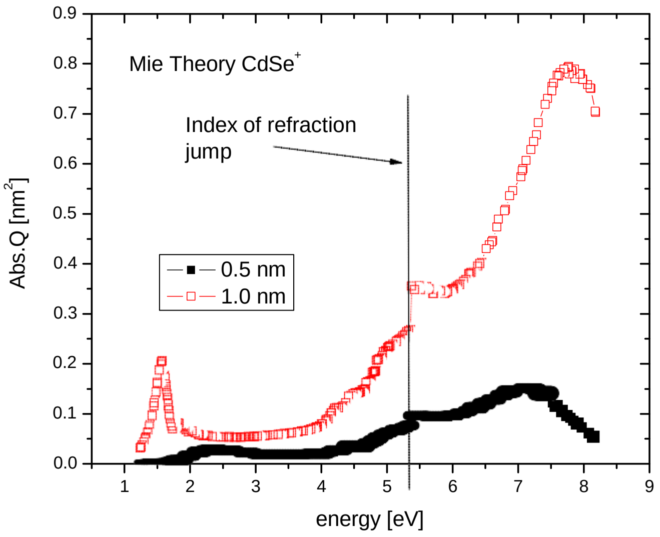

Figure 26: 1.5 eV resonance calculated for a 1 nm CdSe particle.

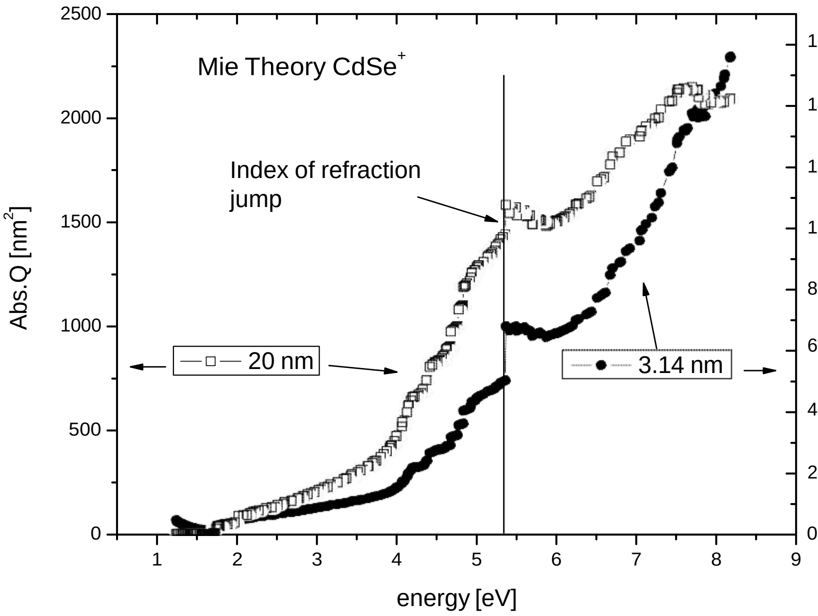

Figure 27: Larger CdSe nanoparticles loose the 1.5 nm resonance.

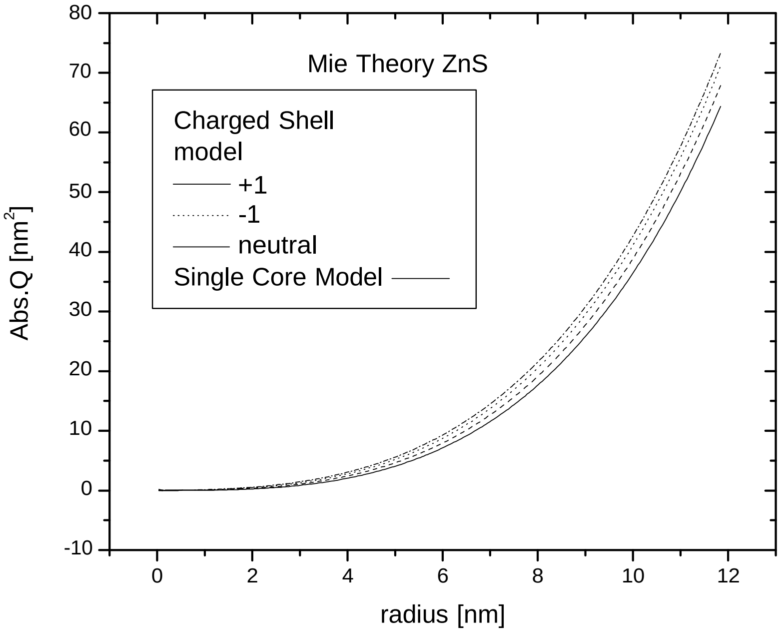

Figure 28: ZnS Mie absorption radial dependence.

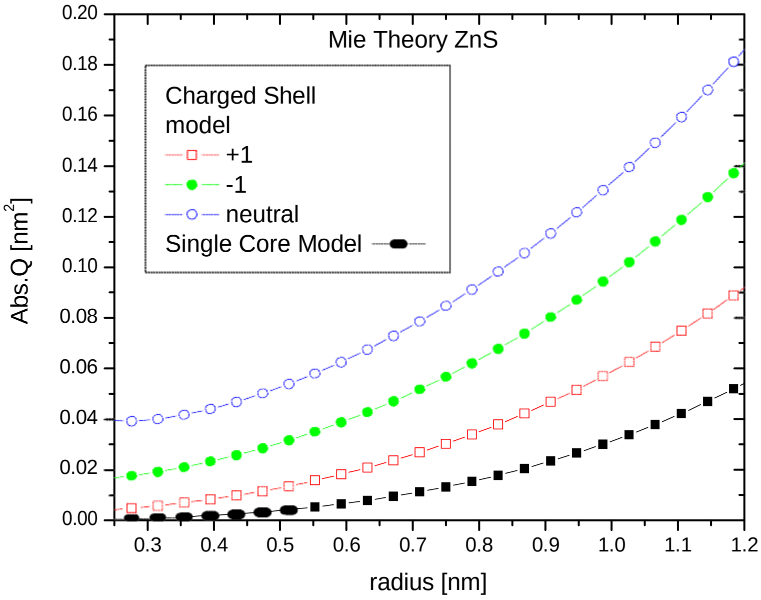

Figure 29: Mie absorption ZnS dependence shows similar behavior as CdSe at smaller scales.

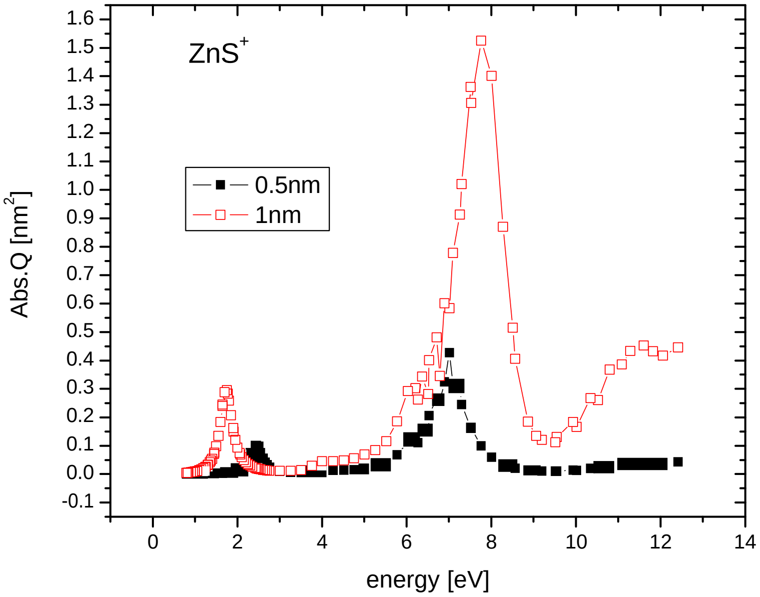

Figure 30: The two ZnS resonances get closer at smaller particle sizes.

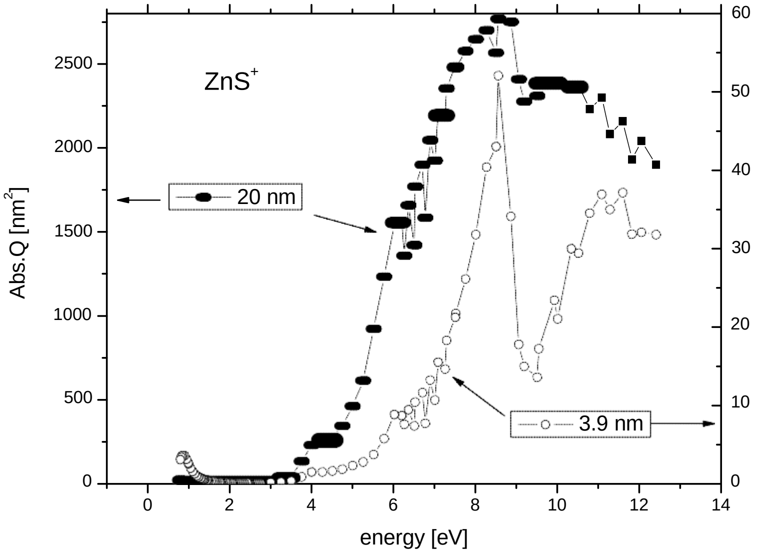

Figure 31: Larger scales show similar behavior as small, above. The two resonances for the 3.9 nm peak are merged in the 20 nm size spectra for ZnS.

In addition to the Mie theory extension of the ionized shell, the core shell model used to calculate the absorption spectra from a single core material which has been ionized, was used for calculating the absorption spectra of the core-shell hetero-structures made of two different materials. For these calculations no ionization was considered. This is justified because the formation of the core-shell structure is made by condensation of the vaporized material, which happens a larger time scales than the electron ion recombination rate and away from the ablation laser field. This is why when we have to compute the Mie absorption for a core shell heterostructure, we don’t have to take into account that they are ionized and we don’t have to take into account a third second shell to calculate for the core-shell structure that is ionized. Core-shell heterostructures are consider to be neutral and only the Bohren model mas used wuth the two different indes of refraction corresponding two the two materials.

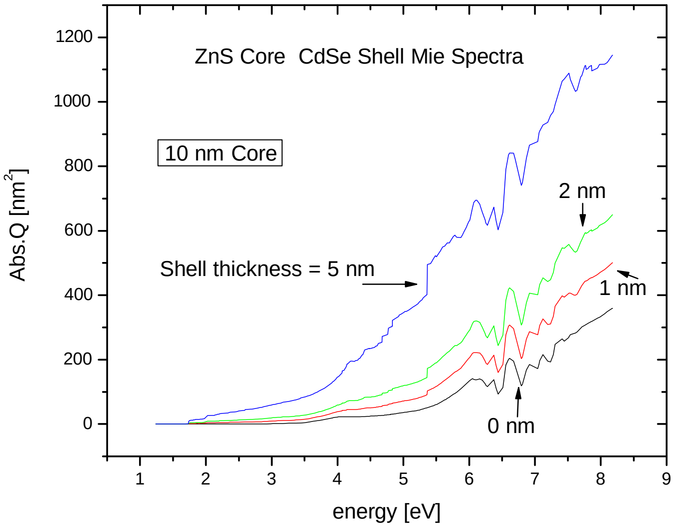

Figure 32: ZnS-CdSe core-shell Mie absorption.

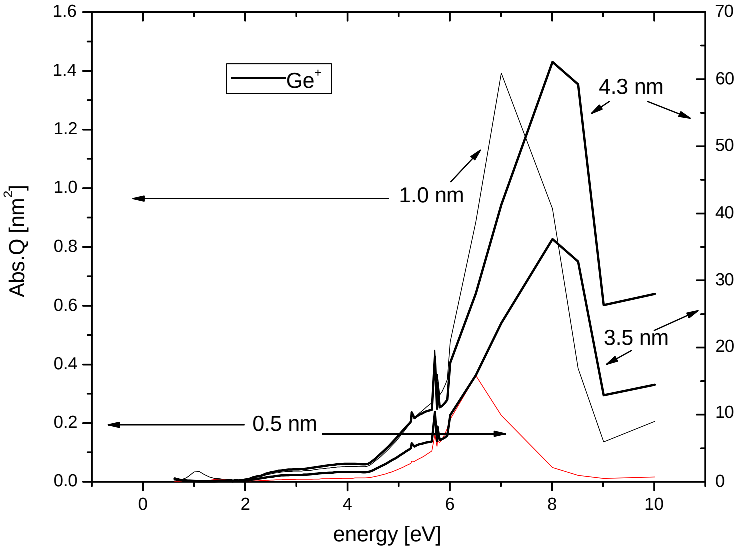

Figure 33: Mie absorption for Ge shows that the 6.5 eV resonance blue-shifts as the particle becomes larger.

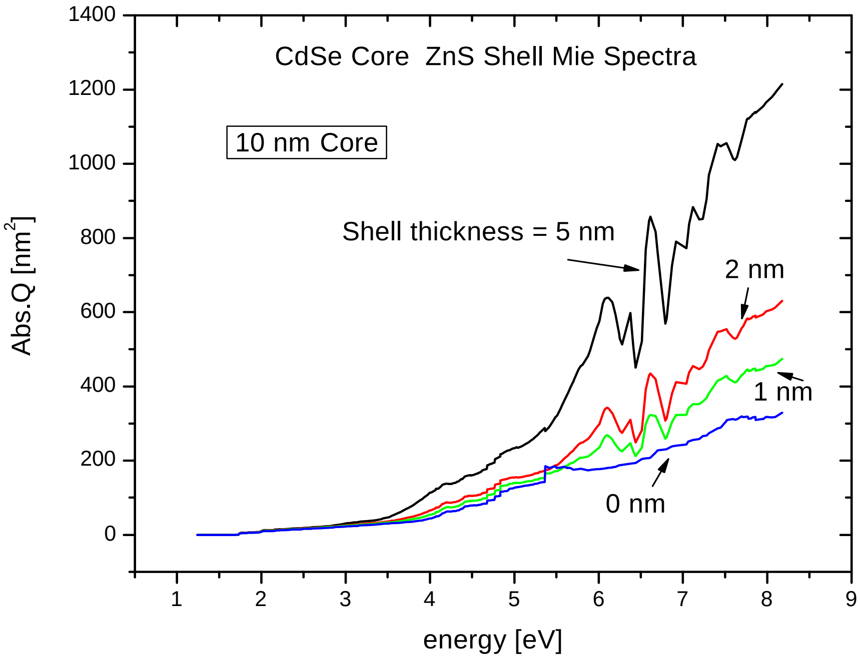

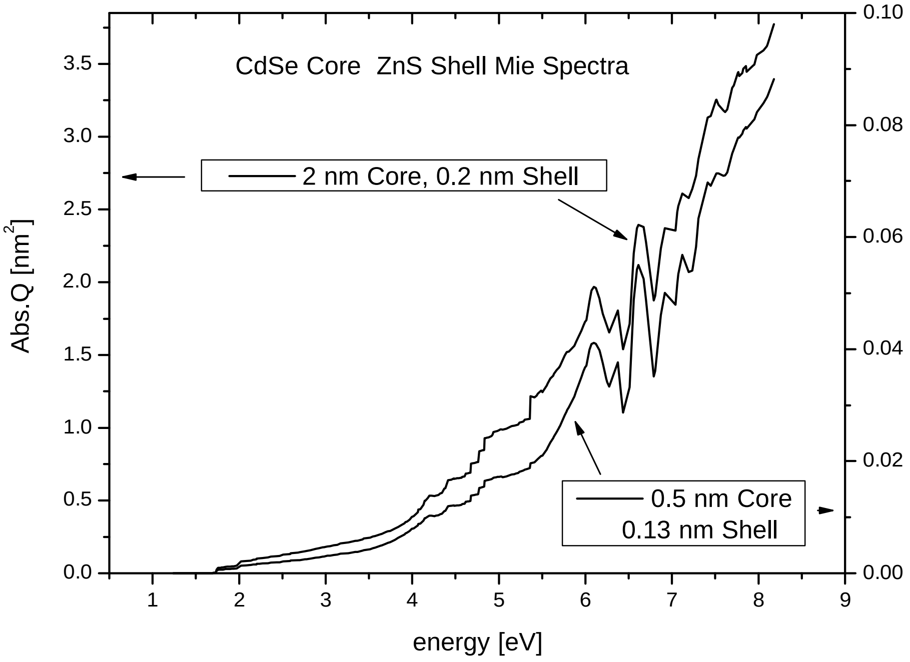

Figure 34: Size dependence on the Mie absorption energy spectra for CdSe-ZnS core-shell heterostructures.

4. Spectral Data

a. CONFOCAL MICROSCOPE MEASUREMENTS

The use of confocal microscopes for looking at quantum dot tagged cells has been used to prove that semiconductor nanocrystals may be superior as existing fluorophores for cell labeling technologies [3]

Dark field images of the fluorescence of nanoparticles deposited on quartz by electrostatic fields were taken with a confocal microscope. The confocal microscope was excited with a 488 nm wavelength from a Coherent Enterprise Ar laser. The laser was coupled to a 2 meter long optical fiber and the total illuminating power was less than 100mW. The fluorescent light was captured with a photomultiplier set to collect a wide spectral range of 100 nm wide in the green region to be able to see the fluorescence from the smallest nanoparticles. Narrow spectral ranges need longer integration times and higher gains that which caused blurry pictures and incomprehensible or no data.

The nanoparticles fluorescence seemed to be stable at laser energies around 20 mW. To measure the fluorescence decay time, we illuminated the nanoparticles with the maximum Ar laser intensity. During this experiment, three different regions on the substrate where illuminated at the same time but their light intensity was measured independently from each other. Regions A and B were big particles or clusters of particles larger than the laser spot size, (300 nm). Region C were dispersed single dots on the substrate, each of the fluorescent spots on region C were smaller than the spot size.

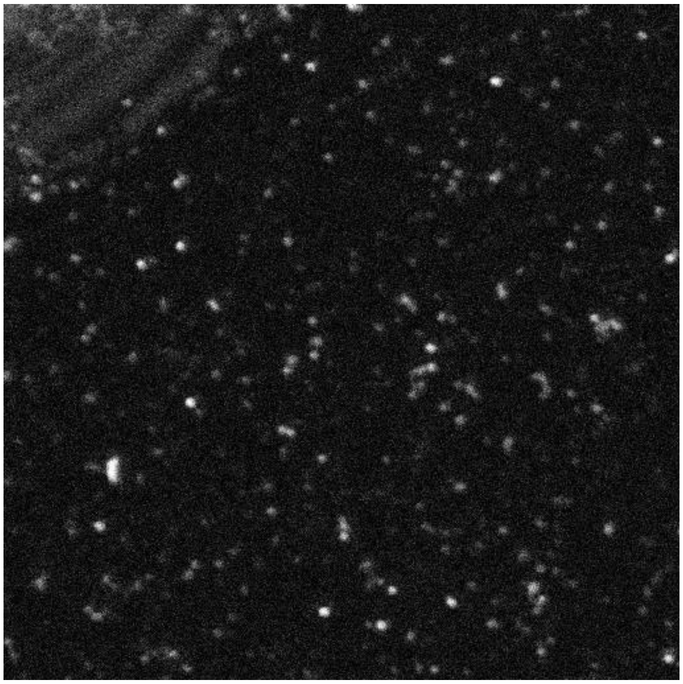

Figure 35: Dark field fluorescence from confocal microscope, image width is 21.62 µm.

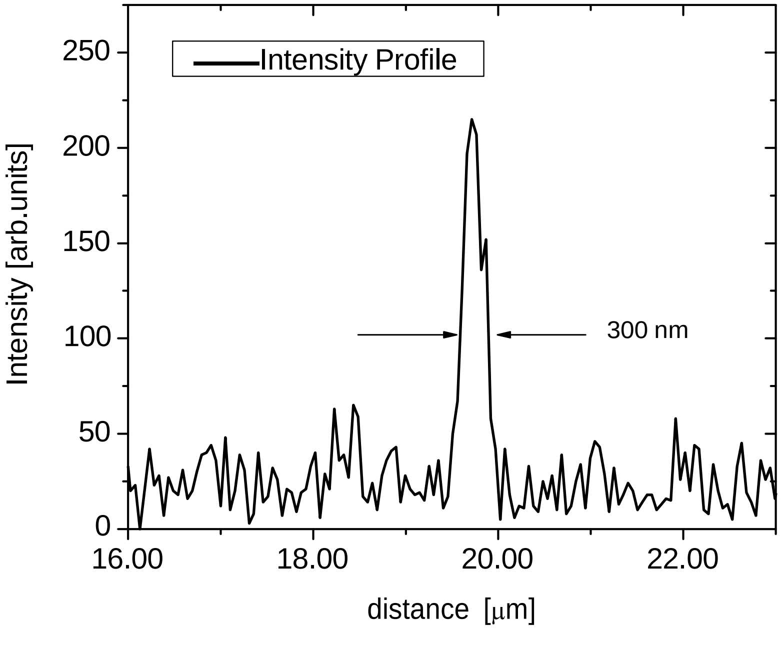

Figure 36: Profile from a dark field fluorescence image that shows that the light sources are smaller than our focused beam, (300 nm)

For the photo-bleaching experiment (for which results are plotted in Fig. 37), the dispersed NPs are on a quartz substrate in an area of 1.05 μm^2 and mean intensity of 91.78 units. With a maximum intensity of 137.99 and a minimum of 73.04 and standard deviation of 20.23 units.

Cluster A covers an area of 0.25 μm^2 with mean intensity of 165.49, max intensity of 170.93 and min intensity of 160.84 with a standard deviation of 3.13. Cluster B is in an area of 0.23 μm^2 with a mean intensity of 221.23 a max intensity of 223.25 and a min intensity of 219.54 with a standard deviation of 1.25. From time dependent intensity plot we see that smaller clusters or individual nanoparticles are quenched in the presence of a high intensity field. Because of the higher curvature of individual nanoparticles and lower cohesive energies, by applying the same laser intensity to all cluster sizes, we induce more surface defects by speeding the atomic migration on smaller structures. This explains the fluorescence quenching of the nanoparticles at higher laser intensities. Larger particles could be clusters of nanoparticles or unablated impurities. Because we were using the Ar laser at full power, we needed to prove that the observed light is not simple reflection from a small fraction of the laser light that could be transmitted by an inefficient filter. The following are two arguments to disregard the possibility of any reflected laser light. Nanoparticle fluorescence quenching shows that observed light is not a reflection from the laser light transmitted through the filter of the system. Reflected light does not quench over time. Another way to disregard the possibility of reflected light are the wavelength dependent fluorescent measurements done on the same type of particles in the Micro-Raman machine. These wavelength-dependent measurements show fluorescent peaks that can't be described as reflection from the laser long tale.

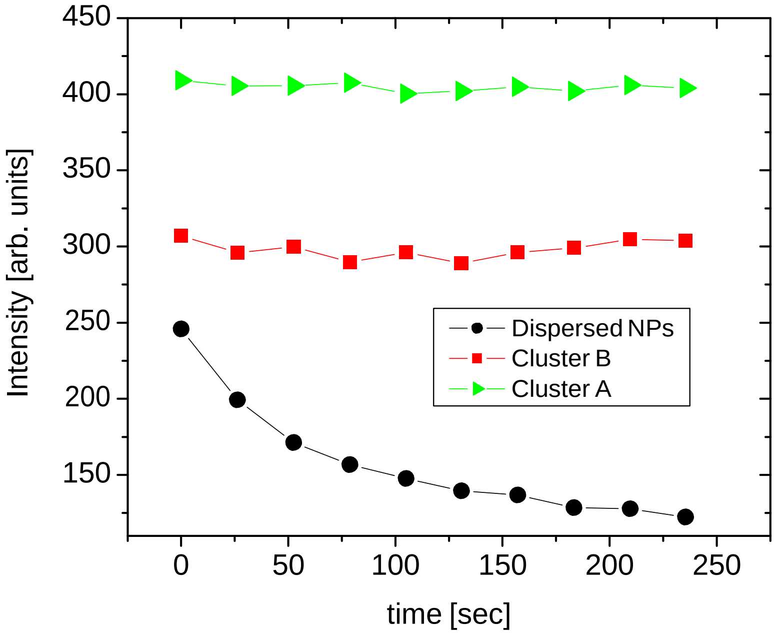

Figure 37: PL nanoparticle bleaching when exposed to maximum laser power above 100mW.

b. ABLATION SPECTROSCOPY

Taking advantage of the borosilicate glass of which the ablation chamber is made we aligned a StellarNet 2000 NIR2-14 spectrometer coupled to a 2 meter long multimode optical fiber. The spectrometer has no filters other than the borosilicate glass and it detects first and second order emissions simultaneously. By first and second order emission we mean that the spectrometer grading overlaps atomic lines that have λ and λ/2 in the same output channel of the spectrometer. To separate first from second order grating reflections we could use at filter that would eliminate all wavelengths below λ, (or above λ/2) but this was not necessary for our studies or analyzing the data.

Depending on the material, atomic lines were most of the time visible as second order lines, and sometimes as first order. When first and second order lines are present in the same spectra no comparison in their relative intensities was made due to the different and unknown sensitivity of our detector at this two different orders. Intensities of spectral lines of the same order can be compared to each other.

The data taken with the spectrometer during the laser ablation does not show PL measurements for the quantum dots. PL occurs three or two orders of magnitude later than the nanoparticle formation time. [27] The nanoparticle has to be cooled down before fluorescing. Spectrometer data was indexed with the atomic lines available through the NIST website. [28]

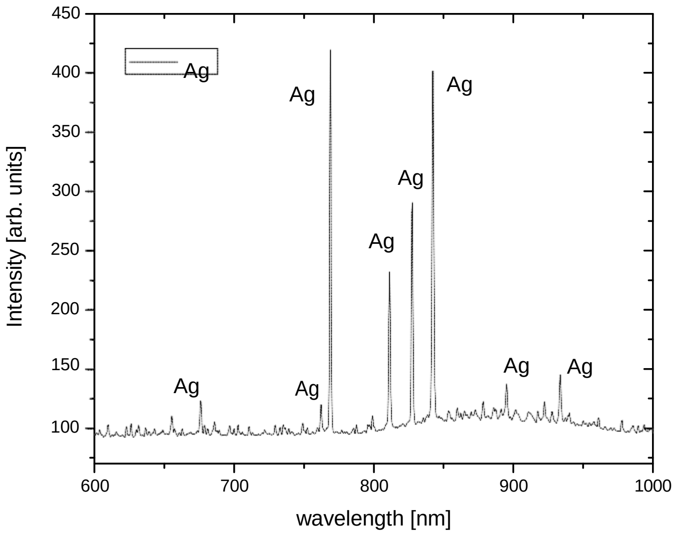

Figure 38: Ag ablation spectra shows atomic lines and Mie scattering from the resonance at 445 nm

Ag neutral λ [nm]	Relative intensity	Ag^+ λ [nm]	Relative intensity
328	550	368	75
338	280	392	70
381	200	408	80
405	100	418	100
421	100	478	100
447	50		
461	30		
466	50		
768	320		
827	500		

Table 3: Second order and first order atomic lines for Ag and Ag^+

Most of the spectral peaks shown in the Ag measurements (Fig. 38) come from well defined neutral atomic transitions. Only one peak was identified for oxygen as its most intense peak at 777 nm. This peak is the brightest of the oxygen lines and it was not measured nearly as bright as the Ag peaks. This means that our Ag ablation is taking place in an almost clean oxygen free environment. As expected, no He lines or any other element lines were seen. NIST tabulated values (Table 3) for a peak intensity of the Ag^+ are as large or even larger than the Ag peaks but they don't show up in our measurements. This suggests that the ions originated in the plasma have a small life time and that during our integration time of 3 seconds, almost all the emitted lines come from neutral atoms. This supports our Mie calculations in which we have assumed that in average at most one Ag ions were generated for each nanoparticle.

The 100 nm FWHM second order peak with a maximum around 890 nm shows radiation coming from silver nanoparticle resonance at 445 nm. This 445 nm resonance is in agreement with the Mie theory nanoparticle resonance for Ag. The resonance is excited by the 405, 421 and 447 nm atomic lines and shows that light coming from the plasmons of silver nanoparticles can be emitted at high temperatures.

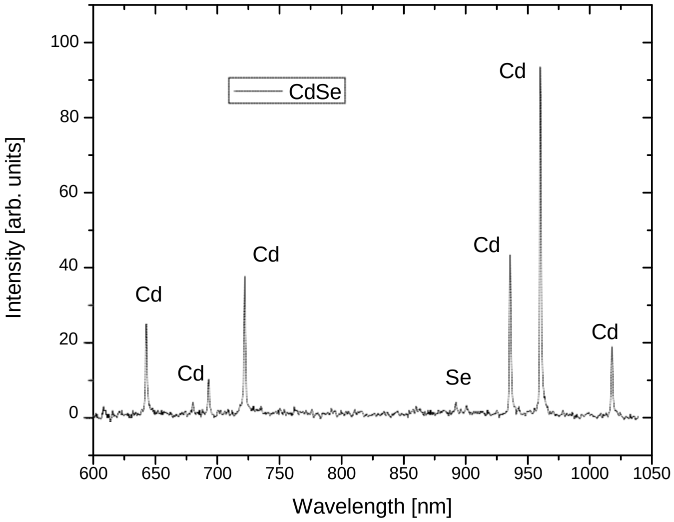

Figure 39: According to the atomic line data, selenium lines have dimmer relative intensities and are hardly seen in the measured spectrum.

Cd neutral λ [nm]	Relative intensity	Cd^+ λ [nm]	Relative intensity
340	800	441	1000
346	1000		
361	1000		
467	200		
479	300		
509	1000		
642	2000		
734	1000		

Table 4: All the neutral Cd peaks correspond to atomic line transitions as tabulated on NIST.

Most of the peaks for the CdSe ablation spectra (Fig. 39) are second order peaks and the sensitivity of our spectrometer seems to be not the same for these second order peaks. The observed intensities match the assumption that the sensitivity of the detector for second order peaks goes down at smaller wavelengths. It is interesting to notice that the 734 nm peak (Table 4) does not shows up in our measurements. It is clear from our measurements that the 441 line is not present most likely because we don’t have many ionized Cd atoms.

Se neutral λ [nm]	Relative intensity	Se^+ λ [nm]	Relative intensity
706	300	446	285
892	300	605	450

Table 5: Atomic lines for Se and Se^+ from the NIST tables.

The absence of the Se 706 peak from Table 5 might be understood in the context of the presence of the Se 892 peak. Both peaks have the same relative intensity according the NIST but the 892 peak that is very low despite it is located in the range of highest sensitivity for our detector. The NIST reported 605 peak for Se^+ which has a higher intensity than the other peaks, can be absent because of the absence of ions or because the lower sensitivity at smaller wavelengths.

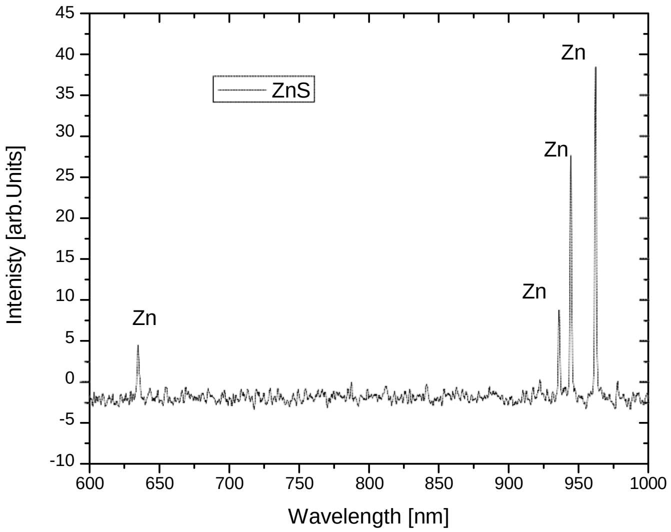

Figure 40: ZnS ablation spectra taken through the borosilicate glass chamber.

Zn neutral λ [nm]	Relative intensity	Zn^+ λ [nm]	Relative intensity
468	300	491	800
472	400	492	500
481	400	602	500
636	1000	610	500
		621	500

Table 6: Zn^+ lines from NIST are not present in our spectra ZnS spectrum.

The large work function of Zn (7 eV) makes it possible to understand why we don't see any of the multiple Zn^+ peaks that should be present according to NIST values in Table 6. Only one first order peak is present in Fig. 40 together with three second order peaks. The relative intensities show clearly that the sensitivity of our detector is not the same for first and second order peak intensity comparison. The 636 peak should have twice as large intensity than the rest peaks but it is measured at almost half the intensity in comparison with the smallest second order 468 peak.

To compare the spectra of the semiconductors and metals that we have ablated with the spectrum of an oxide we ablated and took the spectrum of TiO_2 and we show the results in Fig 41.

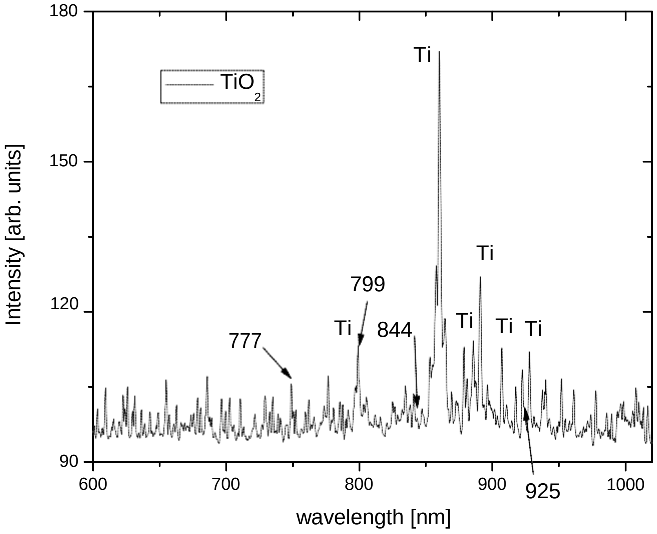

Figure 41: Titania spectra shows oxygen and titanium atomic transitions.

Ti neutral λ [nm]	Relative intensity	Ti^+ λ [nm]	Relative intensity
319	3800	316	1000
399	7800	324	5200
428	890		
430	6000		
431	1200		
439	330		
443	890		
445	1100		
453	6000		

Table 7: Some of the atomic lines from NIST that we should see in our ablation spectra of TiO_2

All the Ti visible lines shown in Fig. 41 are second order lines. NIST data in Table 7 shows all first order lines to be too week to be resolved with our experimental conditions and spectrometer. In addition, the Ti^+ lines are not resolved by our spectrometer. This is an indicator that they could not be present but more likely it indicates that the sensitivity of our spectrometer for this second order light is not good enough. This is supported by the dimmer peaks that neutral Cd shows at these wavelengths.

O neutral λ [nm]	Relative intensity
777	870
799	250
844	1000
925	500

Table 8: Oxygen atomic lines that could be present in our ablation spectra.

Only the 777 and the 799 oxygen lines are seen in the TiO_2 ablation spectra. But not all relative intensities are in agreement with the NIST references because we have no 844 peak above the noise level. Ti line intensities are harder to compare with those from first order oxygen intensities shown in Table 8 because of the difference in sensitivity from the first to the second order of our detector. The 799 peak of oxygen overlaps with the second order of the 399 of Ti but the relative intensities of these two peaks and the peaks around them indicate that what we observe is the Ti peak.

Despite the fact that we are not able to resolve atomic lines coming from ions, we have proved by electrostatic collection methods that many nanoparticles are ionized.

These spectra suggest that the nanoparticles are singly ionized by the time they are formed. Most of the atoms in the nanoparticle are neutralized by recombination in a very short time. A single ionized atom on the surface of the nanoparticle is enough to generate the electrostatic forces required for electrostatic collection. Nevertheless, the light that this single ionized atom emits during the spectral measurements is not as intense as the light that all the other neutral atoms emit right before they condense into a nanoparticle. Because the spectral lines from neutral atoms and ions are closed to each other, neutral atom emission increases the background beyond the single ion intensities.

In previous studies, [29] by using the same technique and spectrometer they were able to measure dysprosium atomic lines that show both neutral and ion atomic emissions. In dysprosium all the ion lines are in the second order for the spectrometer. Even though they do not report these values, their spectrum was able to show the multiple 375 and the 360 nm lines for the Dy ion. The explanation for this is that in contrast to the high work function of all the materials studied in this present work, rare earth materials like Dy have a much lower work function, (around 3 eV) and a larger number of atoms are ionized during ablation. These larger ion numbers emit as much light as the neutral atoms and it is enough light to be detected by the same spectrometer that we used.

5. Metallic and Semiconductor Nanoparticle Evaporation Induced by Laser Pulses

a. INTRODUCTION

In the present experiment nanoparticles are produced by laser ablation of microparticles (LAM) in an aerosol. LAM is a process for the production of nanoparticles of a wide variety of materials (metals, semiconductors and dielectrics), having relatively narrow nanoparticle size distributions and large production rates. [6] In the LAM process, a laser pulse is focused on a stream of microparticles (2-20 µm in diameter) with sufficient fluence to produce breakdown and generate a plasma. A subsequent shockwave compressively heats the particles as a traveling wave. Condensation of nanoparticles occurs behind the shockwave. As a result, a high percentage of the microparticle mass is converted to nanoparticles with a range of mean diameters from 3 and 20 nm depending upon aerosol gas type and pressure. [7,8] Here we investigate when LAM generated particles are shot with the laser a second time. The effects of this second laser pulse have been applied for the formation of core/shell structures [30] and these effects are described with detail in this chapter. In the first section we talk about the experimental setup and how measurements were taken. In the second section we describe our theoretical model and list all the experimental parameters used in our simulation. Then in section three we compare the TEM and PL experimental results with the numerical simulation. Finally in section four we discuss the results and the error sources for the experiment and theoretical model.

b. EXPERIMENT

We used the LAM process for the nanoparticle fabrication [6] with the addition of the double ablation cell described at the beginning of the dissertation and shown schematically in Fig 42**.** The ablation process takes place in quartz, UV transparent ablation cells, where a laminar nozzle flow of helium is focused to a parallel flow by an outer coaxial flow. The coaxial flow has its own exhaust independent from the center flow which is extracted by a skimmer. The center flow carries the feedstock material in the form of a micro-powder aerosol. This is achieved by aerosol generators, which contain microparticle powder (99.9999% Ge CAS-7440-56-4 from Atlantic Equipment Engineers, Ag ~2 µm from DuPont Electronic Materials, 99.995% CdSe CAS-1306-24-7 and 99.99% ZnS CAS-1314-98-3 both from Alfa Aesar) deposited on top of a vibrating membrane attached to a solenoid that is driven at 10 Hz.

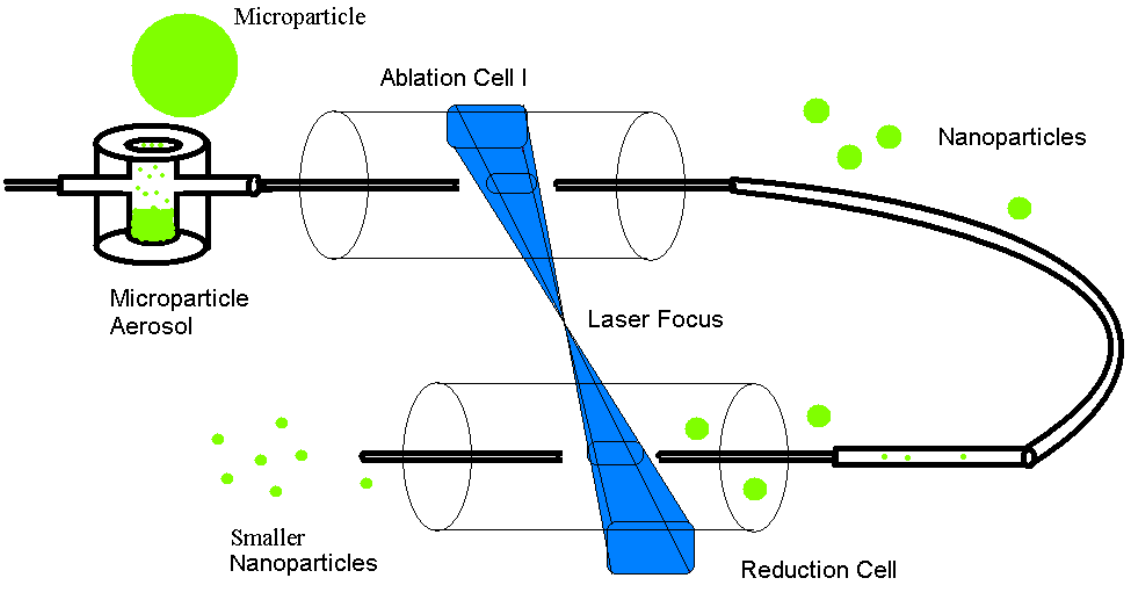

Figure 42: Scheme of the experimental setup.

The same laser beam is used in both ablation cells. The particle flow goes clockwise. The aerosol generator contains the microparticles and creates the aerosol. Right before the second cell, nanoparticles are focused with a coaxial flow before second ablation. For single ablation, only the first cell is used.

Transmission Electron Microscope (TEM) grid samples for singly ablated Ag, Ge, CdSe or ZnS undergoing LAM were collected using direct jet impaction 10 cm away from the ablation region. TEM micrographs taken with a 200 KeV JEOL 2010F microscope were analyzed using MetaMorph® software.

The laser source was a Lumonics KrF excimer laser (λ = 248 nm, 200 Hz rep. rate) with a pulse width of 18 ns. The output energy of the laser was focused to a line between the two cells. The position of the cells was adjusted to provide laser fluence of 2 Jcm^{-2} at the center of both cells. The length of the line focused at each cell is adjusted so that the aerosol flow velocity just fills the focal volume in the time between laser shots, thus in the first cell a microparticle was ablated at most once. After the two ablations, the nanoparticles went through a supersonic expansion which allows NP collection directly onto a TEM grid. The flat walled supersonic nozzle was 100 µm in diameter with a He stagnation pressure of 1 atm. The vacuum pressure was maintained below 200 mTorr by a roots blower. The deposition time ranged from 2 sec to 5 sec to prevent thick depositions on the grid that would make it impossible to count single particles. As an aid, characteristic ablation plasma light was used as a guide for alignment and to monitor ablation efficiency.

In the second cell the NP's were shot with the laser pulse again. The nanoparticles (which have a diameter smaller than the wavelength of the laser), do not develop a shockwave. Nevertheless, because of laser heating to high temperature, the nanoparticles partially evaporate and condense outside the laser beam. These partial vaporization and recondensation reduces their radius and narrows the size distributions. The evaporation rate is dependent on material and particle size. To compare the density of the nanoparticles before and after shrinkage, the particle flow is kept constant for all runs (around 2 *L/min* for center flow and 5 *L/min* for coaxial flow). Comparison of particles before and after ablation are taken with the same flow conditions to minimize the error coming from particles that go unablated in the first cell and ablate in the second cell for the first time.

To understand how fluorescence is affected by the size reduction of NP, single and double ablated CdSe particles collected by supersonic impaction on quartz slides were made and studied. Dry nanoparticle films were taken to a Renishaw inVia micro-Raman optical microscope to study their fluorescence within one hour after they were made to avoid photobleching by oxidation. A 50x objective was used to observe and excite the particles with the 514 nm line from an Ar laser. 0.1% of the laser power was used to take the spectra and 10% of the power was used to burn a spot on the NP film to mark the exact position of the observation. Different nanoparticle densities were deposited on top of the quartz glass in such a way that scanning was possible across the substrate and spectra was captured from agglomerated or individual nanoparticles inside the laser spot size.

c. MODELING

Thermodynamic numerical calculations describe the behaviour of nanoparticles in the second ablation cell. In contrast with the model used to describe the microparticle ablation process, the evaporation of nanoparticles assumes no shockwave creation when the nanoparticles are illuminated with the laser. Because nanoparticles are two orders of magnitude smaller than the wavelength of the UV light, they are heated uniformly and no temperature or pressure gradient forms across them and no shockwave forms. The numerical simulation is based on the heat transfer model used by Kompa et.al. [31] He proposed three different heat transport processes modelled in one system of two coupled equations.

$$q(r) = \frac{4}{3}\rho_s r(t) C_p(T)\frac{dT}{dt} + \frac{\zeta a_v e^{-C_s/kT}}{\rho_s \sqrt{T}} + \eta T \qquad \textbf{- 30}$$

$$\frac{dr}{dt} = -\frac{a_v e^{-C_s/kT}}{\sqrt{T}} \qquad \textbf{- 31}$$

where, in Eq.(30) all terms are given in units of W/cm^2 and $q(r)\ )=I(t)Q_{abs}$ is found by numerically calculating the dimensionless Mie absorption cross section (Q_{abs}) and as a function of the nanoparticle radius (r) and the laser power $I(t)$.

In principle, we should be able to obtain Q_{abs} with the single core Mie theory presented in chapter two, but to take into account the free charges on the surface of the nanoparticle, we follow the core-shell approximation used by Kresin et al. [32]. The exact solution for the core-shell Mie calculation was taken from Bohren et al. [25].

$$Q_{ext} = \frac{\lambda^2}{2r^2}\sum_{n=1}^{\infty}(2n+1)\,\mathrm{Re}(a_n + b_n) \qquad \textbf{- 32}$$

$$Q_{sca} = \frac{\lambda^2}{2r^2}\sum_{n=1}^{\infty}(2n+1)(|a_n|^2 + |b_n|^2) \qquad \textbf{- 33}$$

$$Q_{abs} = Q_{ext} - Q_{sca} \qquad \textbf{- 34}$$

where

$$a^n = \frac{\psi_n(y)[\psi'_n(m_2y) - A_n\chi'_n(m_2y)] - m_2\psi'_n(y)[\psi_n(m_2y) - A_n\chi_n(m_2y)]}{\xi_n(y)[\psi_n(m_2y) - A_n\chi_n(m_2y)] - m_2\xi_n(y)[\psi_n(m_2y) - A_n\chi_n(m_2y)]}$$

$$b^n = \frac{m_2\psi_n(y)[\psi'_n(m_2y) - B_n\chi'_n(m_2y)] - \psi'_n(y)[\psi_n(m_2y) - B_n\chi_n(m_2y)]}{m_2\xi_n(y)[\psi_n(m_2y) - B_n\chi_n(m_2y)] - \xi_n(y)[\psi_n(m_2y) - B_n\chi_n(m_2y)]}$$

and

$$A^n = \frac{m_2\psi_n(m_2x)\psi'_n(m_1x) - m_1\psi'_n(m_2x)\psi_n(m_1x)}{m_2\chi_n(m_2x)\psi_n(m_1x) - m_1\chi_n(m_2x)\psi_n(m_1x)} \qquad B^n = \frac{m_2\psi_n(m_1x)\psi'_n(m_2x) - m_1\psi_n(m_2x)\psi'_n(m_1x)}{m_2\chi_n(m_2x)\psi_n(m_1x) - m_1\psi_n(m_1x)\chi_n(m_2x)}$$

where m_1 and m_2 are the complex index of refraction for core and shell materials and $x = (2\pi a/\lambda)$ and $y = (2\pi b/\lambda)$. a is the radius of the core and b is equal to the sum of a plus the thickness of the shell. χ_n is the Riccati-Bessel function and Ψ_n is the Bessel function of the first kind.

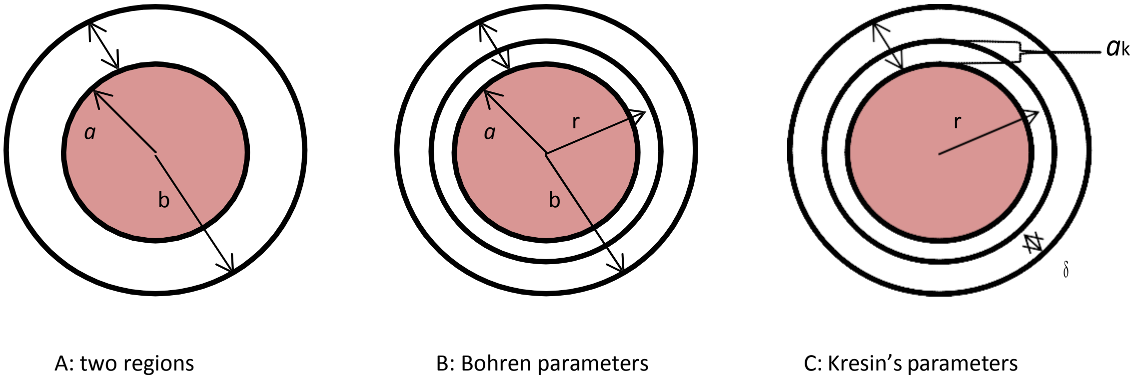

Figure 43: A: Core-shell model as described by B: the Bohren equations and C: the Kresin's parameters. B and C models are equivalent and describe a core-shell particle A.

To calculate this Mie cross section, the electron density shell model was used with the known Ag parameters given in [32], but instead of calculating Q_{abs} from the polarizability, (which is a good approximation for small particles), here we used the exact Mie solutions [25] to calculate first the extinction cross section Q_{ext} and the scattering cross section Q_{scas}. Finally from Eq. (34) we get Q_{abs}. It is assumed singly ionized particles and all the multipoles up to $n = 10$ in Eq. (34) are counted.

In the electron density shell model, δ is the spilling of the valence electrons from the atom surface into the vacuum and it is calculated to be zero for a positive ion. The notation for the present calculation shown in Fig. 43 is equivalent to that on the model by Kresin et. al. The transformation from the two core-shell models are $b = r + a_k + \delta$ and $a = r - a_k$, where a_k is the length of the polarization free zone in Kresin's paper. Notice that in the charged particle model the core a is not the radius r of the physical particle. What matters is that both models are representing a two region core-shell structure; a core with an index of refraction equal to that of the material, and a shell with the index of refraction generated by the free surface charges.

The polarization free zone is represented as a region in which the index of refraction is given in terms of the dielectric constant for free electrons ε_o

$$\varepsilon_o = 1 - \frac{\omega_p^2}{\omega^2 + i\Gamma\omega} \quad . \qquad \textbf{- 35}$$

To calculate the index of refraction of the free electron shell (m_2) we use $m_2 = \sqrt{\varepsilon_o}$ and the damping parameter Γ is $\omega_p/25$, where $\omega_p = 9$ eV is the Ag bulk plasma frequency. The thickness of the free charge shell ($a_k + \delta$) around the charged nanoparticle is found by adjusting the values of a_k and δ around the atomic radius value (for Ag the atomic radius r_s is 0.158 nm) to fit the experimental data, ($\delta = 0$ and $a_k = 0.13$ nm for Ag^+) [32]. After our simulation was finished we were able to reproduce the plots given in the reference as to prove the accuracy of our Mie calculation.

The terms on the right hand side of Eq. (30) describe the heat capacity of the nanoparticle, vaporization, and cooling by atmospheric collisions respectively. The constants are defined by $\eta = (5/2)\gamma Jmk/M$ and $\zeta = 4Cs\,\rho_s/M$ where m is the mass of the incoming atmospheric colliding atom (6.692 x 10^{-24} g for He) and M is the atomic mass of a surface atom (18.04 x 10^{-23} g for Ag, 12.144 x 10^{-23} g for Ge, 15.9 x10^{-23} g for CdSe and 8.12 x 10^{-23} g for ZnS). γ is the number of translational collisions required to transfer a vibrational quantum of energy.

	CdSe	ZnS	Ag	Ge
Cp 300K [J(gK)$^{-1}$]	0.244	0.475	0.228	0.325
Atom radius [Å]	1.33	1.18	1.58	1.22
Melting T [K]	1521	2103	1235	1211
Surface Tension [eV]	0.9	1.63	7.2	1.03
Density [g/cm^3]	5.664	4.079	10.490	5.323
Cohesive [eV]	2.224	3.102	2.95	3.87
Atom M [10^{-23}g]	15.9	12.0	18.04	12.14
Index of R.- 248 nm	2.02+1.58i	2.97+ 0.68i	1.298+1.35i	1.394+3.197i
Work func. [eV]	5.35	7	4.26	5

Table 9: Parameters used in the Calculation

For a reasonable range of values, ($10^{-1} > \gamma > 10^{-3}$), collisional cooling was found to be negligible compared to evaporative cooling. The flux of atoms on the surface of the particle is given by J and this is a function of velocity and temperature of the gas on the surface given by $J = 6x10^{23}\eta_g[8kT/(\pi m)]^{1/2}$ where η_g is the gas density (η_g = 2.68 x 10^{19} atoms.cm^{-3} at one atmosphere of He).

The parameter a_v in the vaporization term depends on the temperature (T_0) and pressure (P_0), which define a point in the coexistent curve, and it is calculated from simultaneously solving the solid-gas Clausius-Clapeyron and the continuity equations at the surface [33], as shown in Eq. 28. The dependence of P_0. on T_0 at the coexistent curve is determined from the experimental tabulated values for Ge, [34] from a parametric equation [35] for Ag, and from the melting points for CdSe and ZnS. [35] C_s (2.95 eV for Ag, [36] 3.87 eV for Ge, [37] 2.224 eV for CdSe and 3.102 eV for ZnS [38]) is the cohesion energy of the nanoparticle and C_p is the heat capacity at constant pressure given as a function of temperature [39]. Because of its dependence on the coexistent curve point (P_0, T_0), the value of a_v follows the equation:

$$a_v = \sqrt{\frac{8M}{\pi k}}\frac{P_0}{\rho_s}e^{Cs/kT_o} \qquad \textbf{- 36}$$

Eq. (31) is related with the vaporization term and it gives the time dependence of the nanoparticle radius, where r is the radius of the particle, t is time, T is the temperature in *Kelvin* and ρ_s is the density of the materials (10.490 g/cm^3 for Ag 5.323 g/cm^3 for Ge, 5.664 g/cm^3 for CdSe and 4.079 g/cm^3 for ZnS in bulk materials).

Solving the two coupled differential equations for a time ten times longer than the duration of the laser pulse (18 ns), we obtained the time dependence of the temperature and radius of the particle after a single shot**.**

For this simulation to work in the nanoscale regime, bulk Eq. (36) was updated for nanoparticles values by substituting the pressures and temperatures at the coexistent curve. The pressure of a nanoparticle is obtained by using the Kelvin equation

$$P_n = P_b \exp\left(\frac{2\gamma_n M}{\rho_s RTr}\right) \qquad \textbf{- 37}$$

and the evaporation temperature [36] for a curved nanoparticle (T_n) is

$$T_n = T_b\left(1 - \frac{32\pi\gamma_n r_s^3}{3E_B r}\right). \qquad \textbf{- 38}$$

P_n is the pressure on the curved surface of the nanoparticle which is given it terms of the pressure of the flat surface of the bulk material (P_b). Similarly, T_n is given in terms of the temperature of the bulk (T_b) and the nanoparticle radius r. The surface energy γ_n is 7.2 Jm^{-2}, 1.03 Jm^{-2}, 0.9 Jm^{-2} and 1.672 Jm^{-2} for Ag, [36] Ge [37], CdSe [40] and ZnS [41] respectively. Finally, the bulk cohesive energy is also substituted for the cohesive energy of a nanoparticle [36] C_n.

$$C_n = C_s - \frac{8\pi\gamma_n r_s^3}{3r} \qquad \textbf{- 39}$$

where r_s is the bulk radius of an atom on the surface of the nanoparticle and r is the NP radius.

d. RESULTS

After analyzing hundreds of nanoparticles, based on HRTEM micrographs, we could observe experimentally that their mean radius decreases from 3.4 ± 0.2 nm to 2.6 ± 0.2 nm, from 4.3 ± 0.1 nm to 3.5 ± 0.1 nm, and from 3.1 ± 0.2 nm to 2.6 ± 0.2 nm for Ag, Ge and CdSe, respectively. No ZnS nanoparticle reduction was observed within the width *w* of the distribution. These values are obtained by fitting the experimental size distributions with a Lognormal distributions (expected for particles grown via vapor coalescence) with equation,

$$y = \frac{1}{\sqrt{2\pi}wx} e^{\frac{-\left(\ln \frac{x}{xc}\right)^2}{2w^2}} \qquad \mathbf{-\ 40}$$

Where *xc* and *w* are the experimental mean size and size distribution width reported values. The data and fits for the Ag, Ge, CdSe and ZnS distributions are shown in Figs. 44, 45, 46 and 47 respectively. These size distributions were taken from many size reduction images like those shown in Figs. 48 to 51. To compare the size dependence, Fig. 52 shows the theoretical values of the mean particle radii and temperatures for each of the four materials.

By looking at the experimental *w* value, it is seen that the Ag size distribution narrows after the second pulse. In contrast, the *w* value for the Ge size distribution increases after the second pulse. This is because evaporation has competing processes, like aggregation. Aggregation and subsequent coalescence strongly take place in the irradiation of Ge, Smaller particle dumbbells have the lowest surface tensions in Ge (with respect to the other studied materials) and when they coalesce together after the second ablation they form larger particles which are also counted in the final distribution as single nanoparticles.

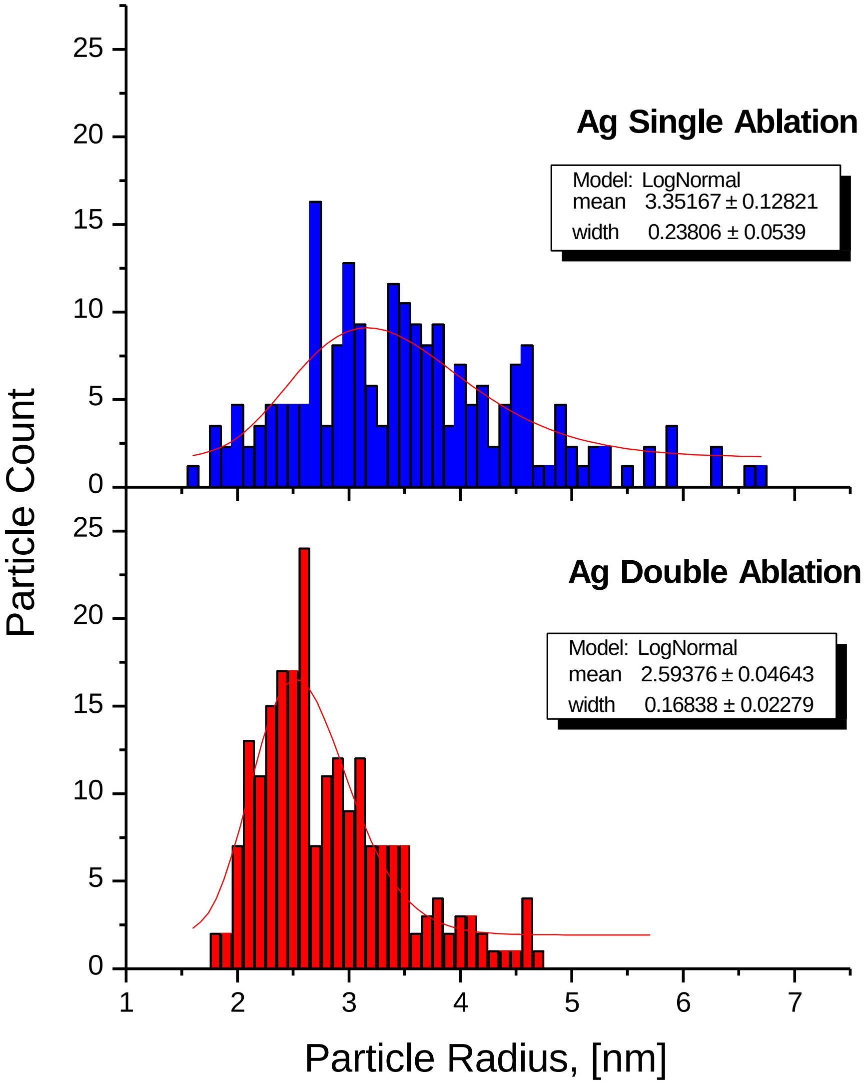

Figure 44: Ag nanocrystals reduce their mean radius from 3.4 nm and Lognormal width of 0.23nm to a mean radius of 2.2nm and Lognormal distribution width of 0.16 nm.

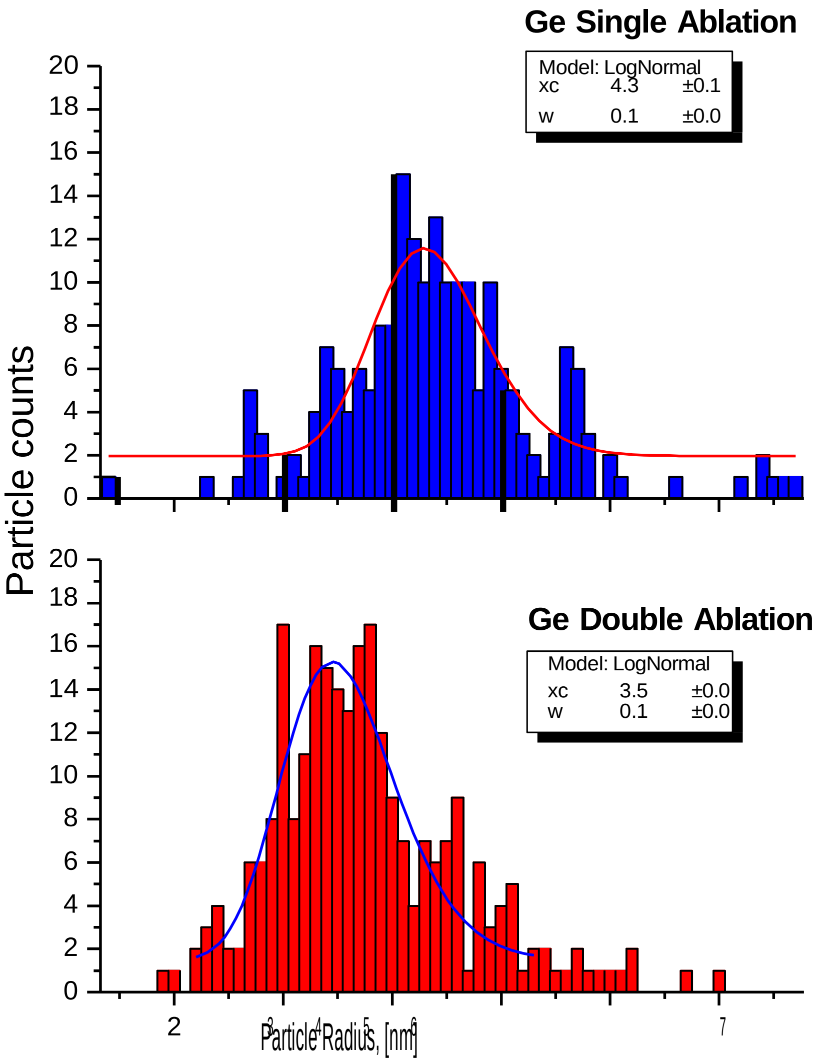

Figure 45: Ge nanocrystals reduce from a 4.3 nm mean radius and Lognormal width of 0.11 nm to a mean radius of 3.5 nm and Lognormal distribution width of 0.14 nm.

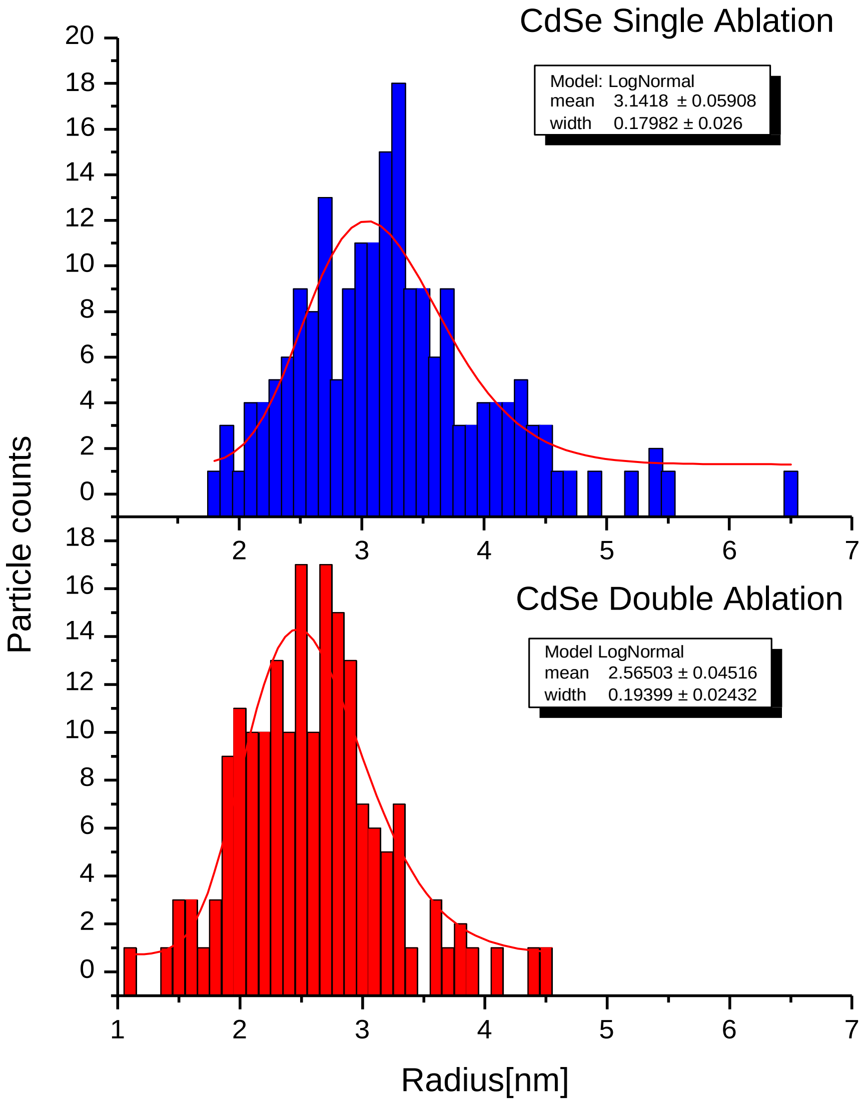

Figure 46: CdSe nanocrystals reduce from a 3.1 nm mean radius and Lognormal width of 0.17 nm to a mean radius of 2.5 nm and Lognormal distribution width of 0.19 nm.

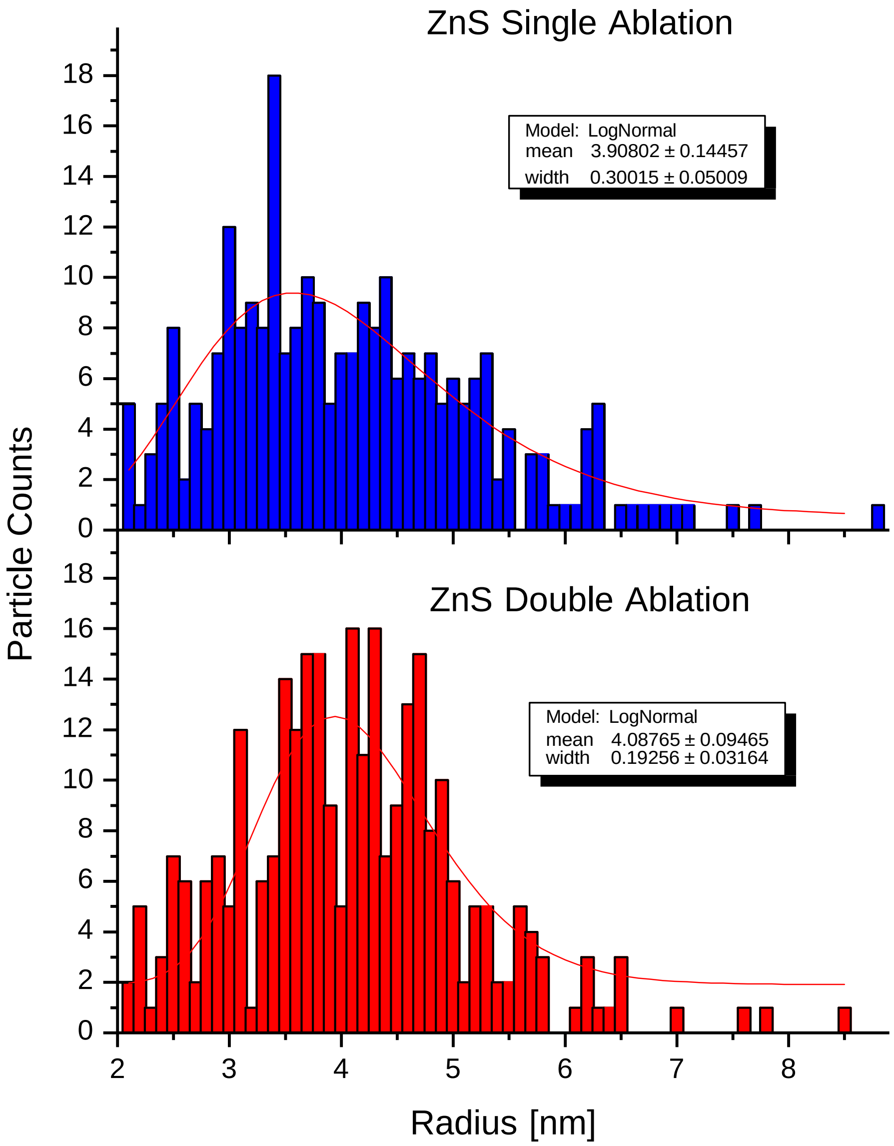

Figure 47: ZnS nanocrystals stay from a 3.9 nm mean radius and Lognormal width of 0.30 nm to a mean radius of 4.0 nm and Lognormal distribution width of 1.19 nm.

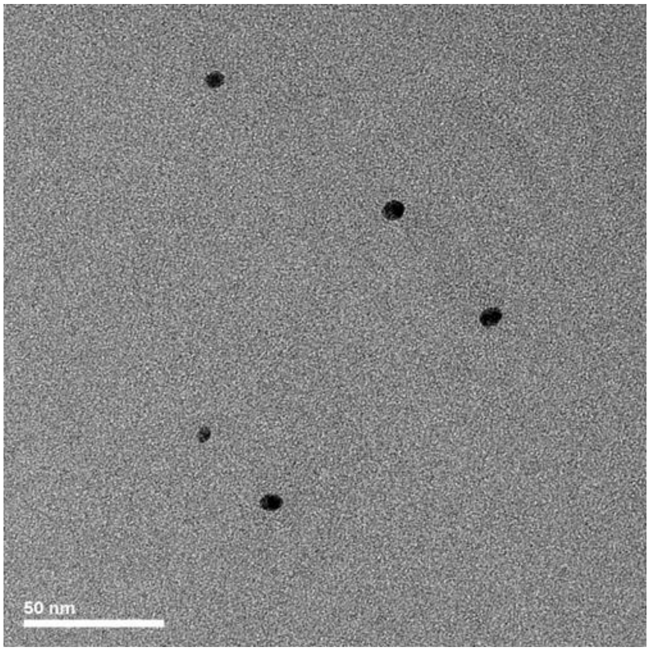

Figure 48: HRTEM micrographs of Ag nanoparticles right after formation in the first cell in a single shot.

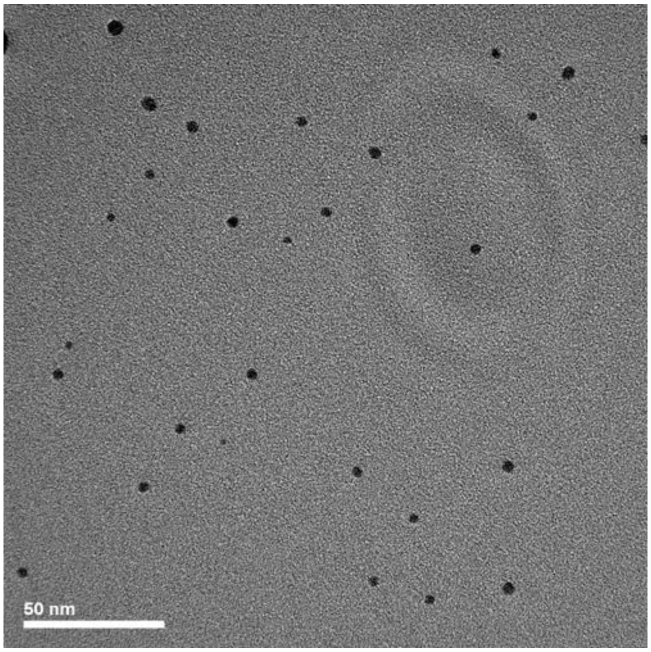

Figure 49: Evaporated Ag nanoparticles after irradiation with a single pulse in the second glass cell.

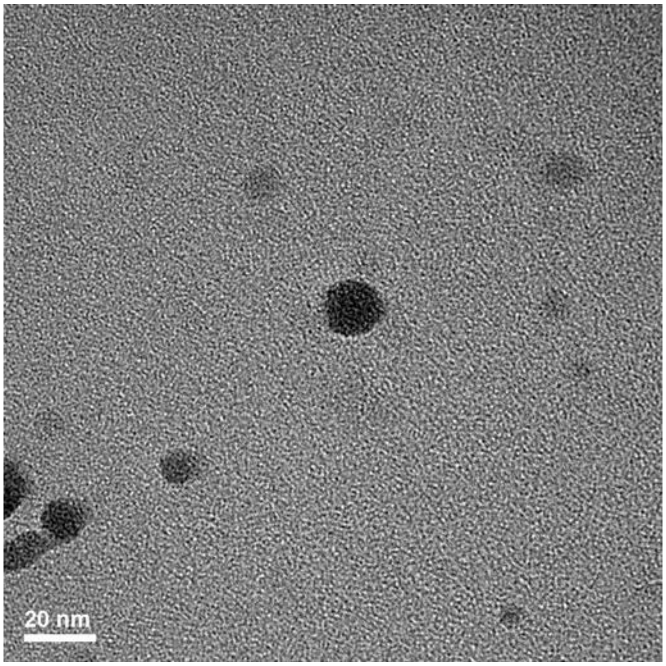

Figure 50: HRTEM micrographs of Ge nanoparticles right after formation in the first cell in a single shot.

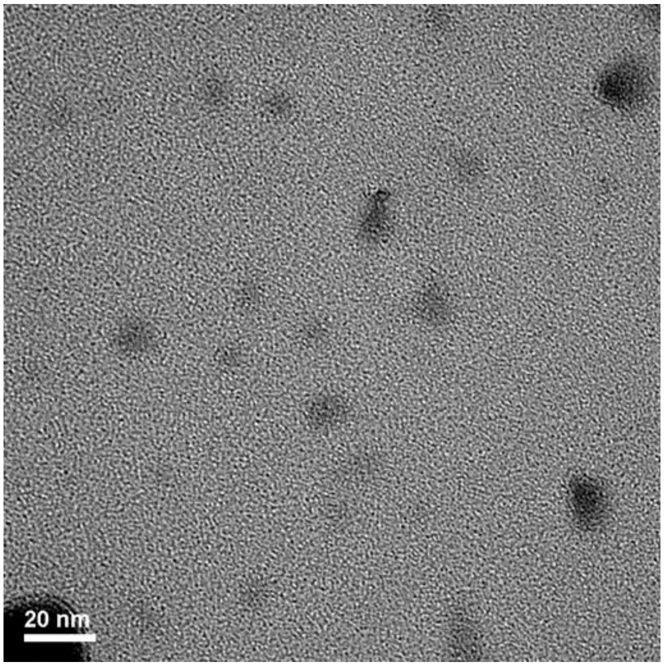

Figure 51: Evaporated Ge nanoparticles after irradiation with a single pulse in the second glass cell.

The characteristic mean size for Ge before the second ablation is 1.2 times larger than that for Ag as shown in Fig. 45. During the second pulse and for a given fluence, CdSe reduces its diameter faster than any other material (Fig. .52). According to the simulation results in Fig. 53, all materials except for ZnS reach their melting point within the first half of the laser pulse. (1121.7 K for a 4.3 nm particle of Ge and 1049.2 K for a 3.35 nm particle of Ag; as calculated from Eq. (38)). CdSe reaches its melting point, for bulk at 1521 K and nanoparticle at 1225 K for a 3.1 nm radius. In contrast, the ZnS temperature never reaches its melting point of 2103 K for the bulk and 1800 K for a 3.9 nm particle. The simulation shows that at these high temperatures only Ag and CdSe NPs are completely vaporized into atoms and ZnS and Ge remain as nanoparticles with a few hundreds of atoms. Nevertheless, all of them should be vaporized to a size small enough that cannot be observed in the TEM grid or collected by impaction after the second laser pulse. Positively charged nanoparticles such as Ag absorb more light than neutral or negatively charge nanoparticles, but they all reduce their diameter enough not to be resolved in this experiment. This is clearly seen in Fig. 54 that shows absorption as a function of energy resulting from running the simulation for Ag^+ and Ag^-. The smaller the particle, the higher the difference in absorption as shown in Fig. 55. Leading to differences in absorption as high as 50% for a radius of 0.5 nm.

Figs. 56 and 57 show the fluorescence spectra of single and double ablated CdSe nanoparticles on quartz substrates. The raw data was fitted to a Gaussian to obtain the mean and width of the PL peaks. In Fig. 56 we clearly see a peak at 627.51 ± 0.12 nm with a standard deviation of 95.71 ± 0.205 nm. In Fig. 57 we see images of an individual light spot on the surface of quartz that could have only one or a few NPs with narrow emission peaks at 525.649 ±0.051 nm and standard deviation 5.784 ± 0.38 nm. And in Fig. 58 we have focused on a 300 nm wide green spot with PL peaks located at 520.96 ± 1.20 nm and 525.18 ± 0.41 nm and have standard deviations of 2.34 ± 0.459 nm and 4.87 ± 1.06 nm respectively. This bright spot suggests that our single spot might be a superposition of nanoparticles with radii of a few angstroms different from each other.

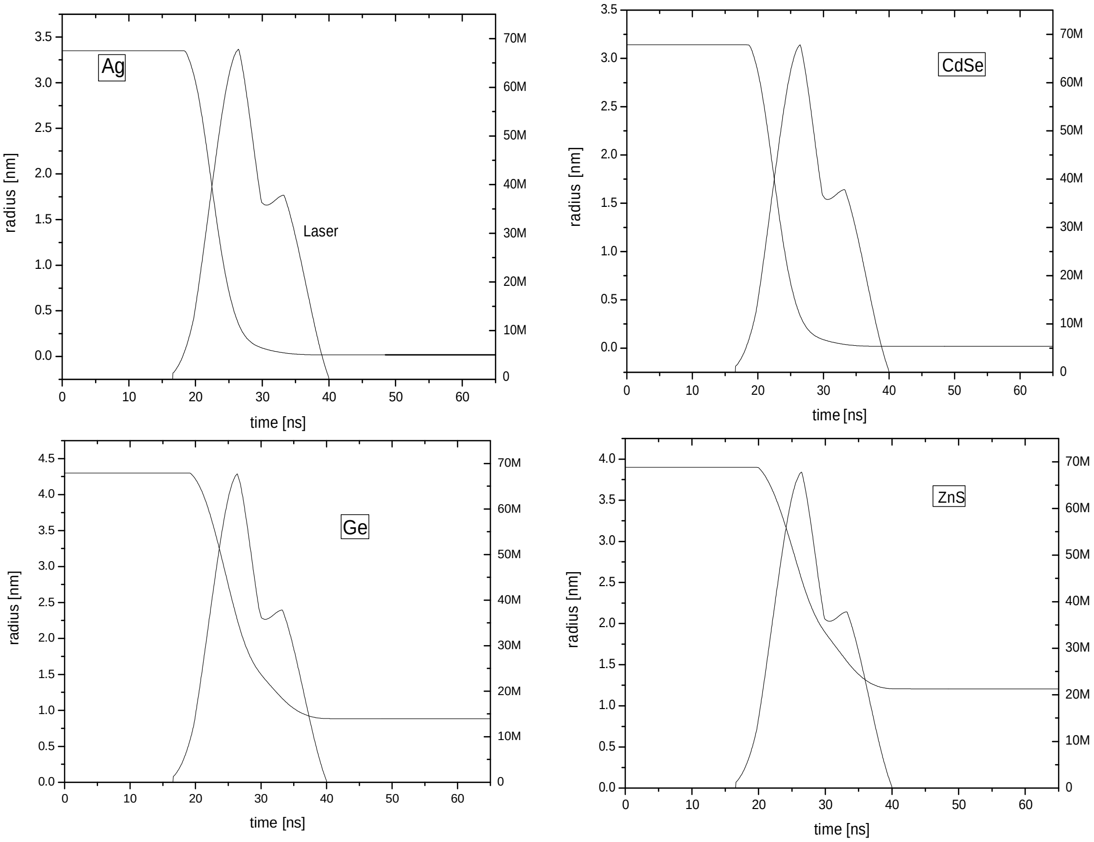

Figure 52: Theoretical particle radii for the four materials during the second laser pulse. The two peak curve is the measured excimer laser pulse.

CdSe fluorescence spectra of single and double ablated nanoparticles were used to calculate the radius of the particle before and after the second laser pulse. We assumed tjat the Stock shift for each peak was the same as for the bulk. The difference between the bulk band gap and our measured 713 ± 0.03 nm bulk fluorscencence peak is 35 ± 0.03 nm. In Eq. (41) we input the exciton energy (E_{exc}) and solve this equation to find the radius *r*.

$$E_{exc} = E_g + \frac{h^2\pi^2}{2m_e^* r^2} + \frac{h^2\pi^2}{2m_h^* r^2} - 1.8\frac{e^2}{\varepsilon r} \qquad \textbf{- 41}$$

The effective mass of the electron ($m_e^* = 0.112m_o$), the effective mass of the hole ($m_h^* = 0.746m_o$) and the energy gap (E_g = 1.829 eV) were taken from Madelung [42]. m_o is the mass of the free electron and the dielectric constant (ε = 7.8) is the average dielectric constant for CdSe.

For the single ablation the calculated corresponding radius for 627 nm PL peak is $r = 3.4 \pm 0.2$ nm and for the double ablation 525 nm PL peak is $r = 2.2 \pm 0.2$ nm

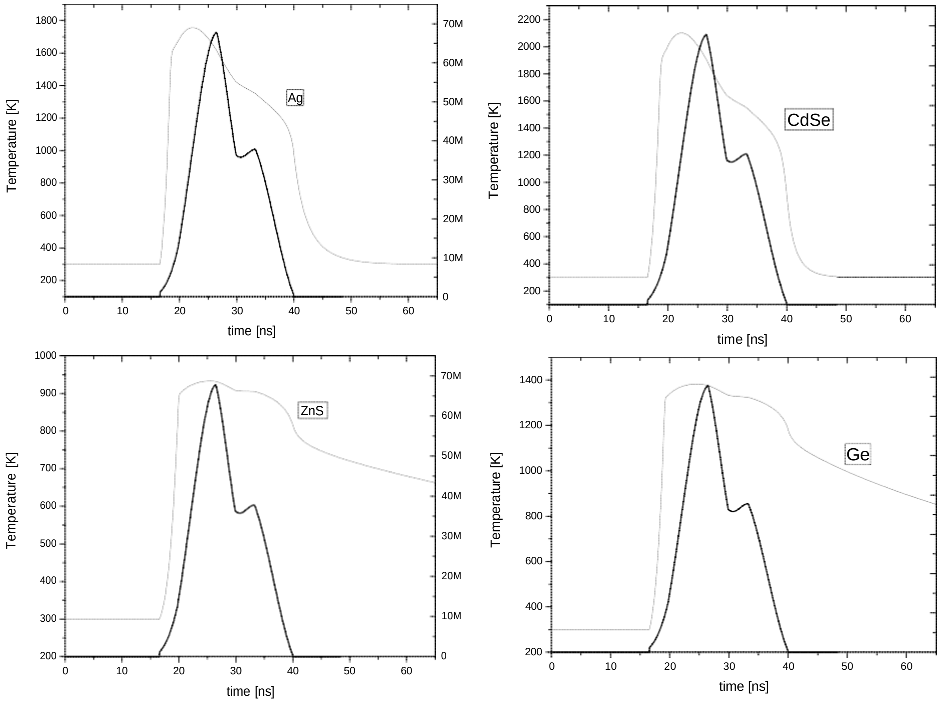

Figure 53: Theoretical temperatures for Ag, Ge, CdSe and ZnS. Only ZnS never reaches its theoretical melting point.

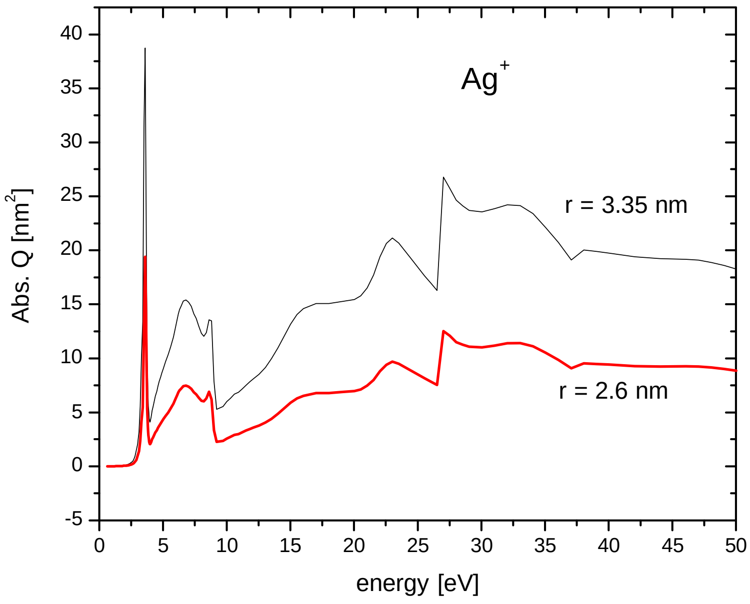

Figure 54: Mie Theory computation for charged nanoparticles uses a core-shell structure configuration for the model. a) a_k and δ were the same used by Kresin et. al. for Ag$^+$ to calibrate our simulation.

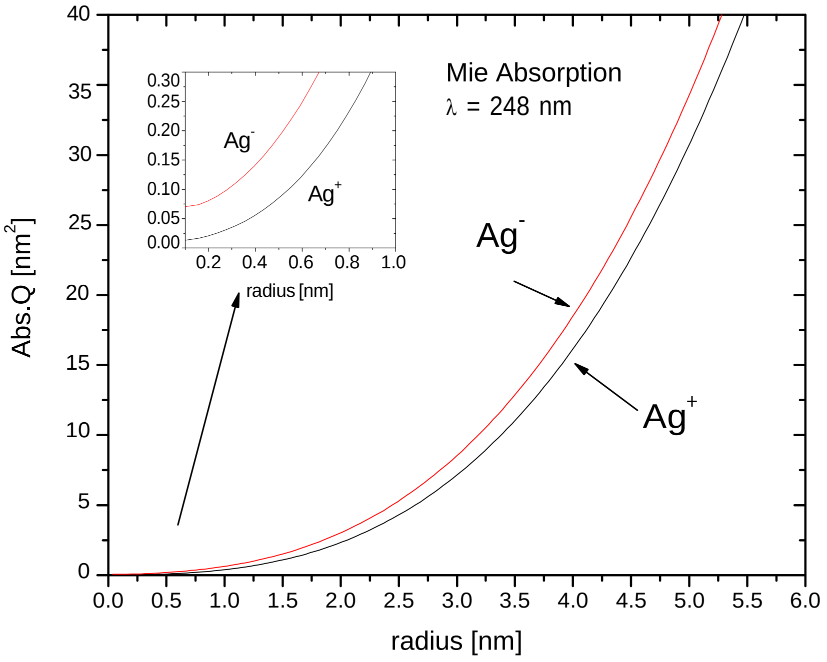

Figure 55: Larger particles show faster size reductions because they have larger absorption Mie cross sections. Inset: For particles around 0.5 nm in radius Mie absorption doubles when going from positive to negative charged particles.

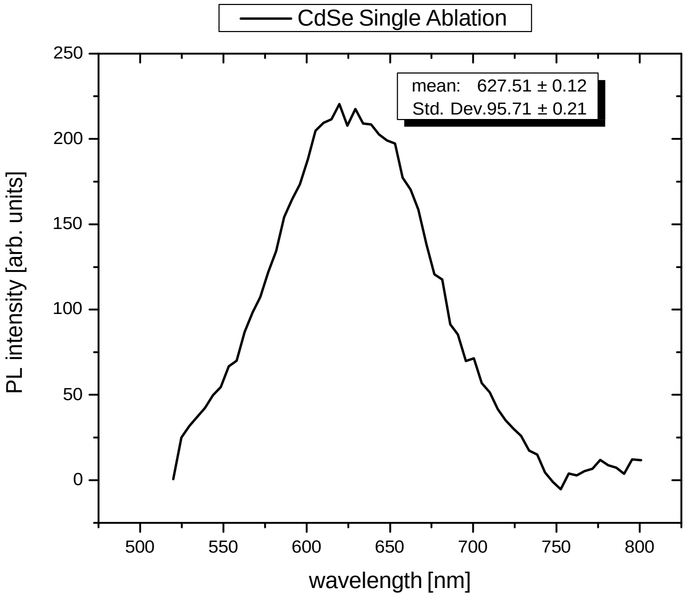

Figure 56: Single ablated nanoparticle fluorescence. CdSe NP 627 nm fluorescence peak shows that we have made CdSe NP with radius r = 3.4 ± 0.2 nm when calculated by the parabolic band approximation given by Eq.41.

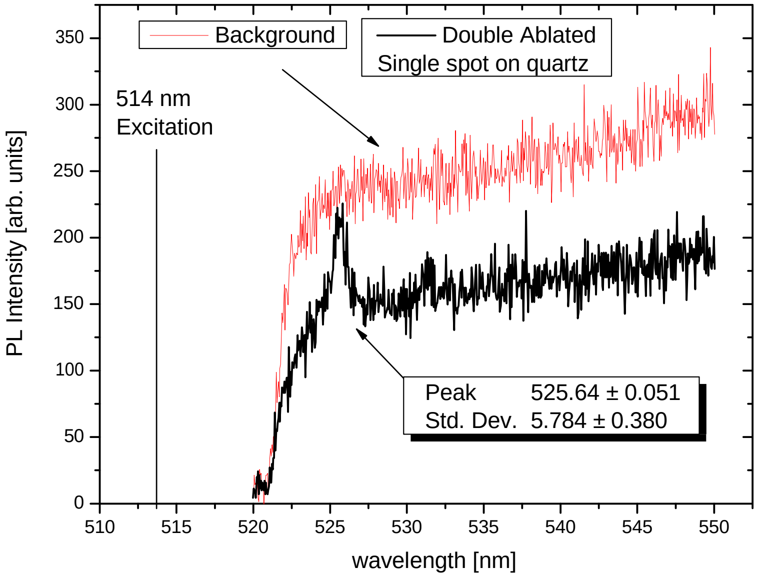

Figure 57: Double ablated nanoparticle fluorescence. Green nanoparticle fluorescence at 525 nm shows that after a double ablation the nanoparticles change in size down to a radius r = 2.2 ± 0.2 nm when calculated with Eq.41. for the parabolic band approximation. a) Spectrum of Single PL spot for a double ablated NP on quartz surface as seen with a 50X optical microscope.

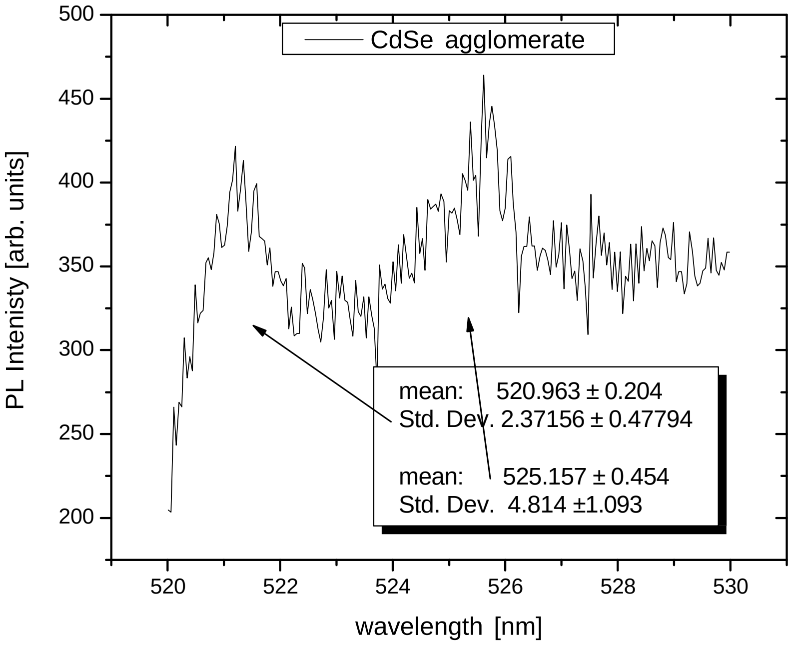

Figure 58: Double ablated nanoparticle fluorescence. Green nanoparticle fluorescence at 525 nm shows that after a double ablation the nanoparticles change in size down to a radius *r* = 2.2 ± 0.2 nm when calculated with Eq.41. for the parabolic band approximation. NP cluster shows different sizes of double ablated NPs in the same spectra.

e. DISCUSSION

i. Size Distributions

The observed differences in size distributions for the four materials are not only a result of the LAM process itself but also how effective the collection process is and the resolution of the HTEM measurements. As we explained earlier in the experimental section, to obtain the size distributions from the analyzed images, radii of the nanoparticles were calculated with MetaMorph® software as a function of their contrast with the background. The contrast sets the limits for the minimum particle size that can be counted and this limits the detection limit for particles at around 1 nm radius. For best contrast, thinner support films would work better but they don't resist the nanoparticle direct impaction collection process. Thin support films like those used for counting chemically grown particles are normally torn and this cannot be used. Another disadvantage that is normally present when collecting particles directly from a gas flow is that the size distributions depend not on the real particle size but also on the "active" nanoparticle surface [43]. The LAM process has no such disadvantage because in LAM, resulting particles are spheres and therefore they all have the same well defined active surface. Surface impaction at supersonic velocities on the other hand, sets the theoretical minimum particle size that can be collected. This theory indicates that with the pressure gradient across the nozzle and the given density of the studied materials, the minimum particle radius that can be collected on the impaction surface after the expansion are 0.9 nm, 2.0 nm, 2.1 nm and 2.7 nm for Ag, CdSe, Ge and ZnS respectively (Fig. 10).

In this double ablation experiment, chaining is sometimes present. Chaining of nanoparticles can happen after the first ablation and before the second ablation depending on how long it takes to the ions to loos their charge and the distance they have to travel before the second ablation. Under the second laser pulse, agglomerated particles exit the second ablation chamber and larger irregular shaped nanoparticles are formed as seen in Fig 50. Germanium NPs tend to agglomerate more than the rest of the NPs and we explain it through the much lower cohesive energy of Ag, CdSe and ZnS with respect to Ge. To only take into account double ablated nanoparticles and neglect any agglomerated nanoparticles, we just measured only spherically shaped nanoparticles for tabulating the size distributions. This implies that for particle counting, highly magnified images were needed and because of this, it is difficult to have large number of particles on a single high resolution micrograph. Several images with the same contrast needed to be analyzed. Furthermore, additional discrepancies may occur when single ablated nanoparticles miss the second ablation during the beginning of the run when we try to stabilize the central flow. This makes false size distributions by adding more counts to the larger domain of the distribution. The particles that skip the second laser shot are spherical and are counted as double ablated in the measured size distributions after the double ablation setup. On the other side of the distribution, however, particles with radius smaller than 1nm are hard to collect or to see with HTEM and this will affect our observed distributions.

ii. Simulation

The simulation shows a correlation between the particle evaporation and some of the experimental parameters used in it. The ratio between the initial and final particle size was plotted for some of the most important parameters used in the computation, (Fig. 61). Ag has a final radius of 77% its initial NP radius, Ge is 81% of its initial NP, CdSe is 84% and ZnS reminds unchanged (100%), according with the experimental values. These values are plotted for each material and for most of the plotted parameters (Fig. *a*, *b*, *c* and *d*) we observed that they increase from left to right having a maximum for ZnS. Figs. *e* and *f* have a decreasing behavior with the lowest value for ZnS. The work function is always increasing, just like the melting point. The density plot is decreasing like the atomic mass.

With the exception of the plot for the imaginary index of refraction, all the other parameters have similar values for Ge and CdSe. This predicts the similarities in the mass reduction for these two materials observed in the experiment. It also makes it clear that, theoretically, Ge shows a larger size reduction compared to CdSe, due to its larger complex index of refraction which is associated with Beer's law absorption. Large differences in the measured behavior between ZnS and Ag are clearly shown in the contrasting values for all the parameters of these two materials. The simulation is sensitive to the surface energy (γ_n) and this value increases by a factor of four from bulk Ag to the Ag NPs. [36] Here we have used the NP value for Ag and CdSe and the bulk value for Ge and ZnS due to the lack of available data in the nanoscale for the last two materials.

The cooling mechanism due to thermionic electron emission was calculated with the Richardson-Dushman equation but its value was negligible in comparison to the other presented mechanisms. Cooling mechanisms like radiation in the form of black body radiation and heating by electron-ion collisions were calculated and found to be negligible as well. For all materials, agreement between theory and experiments is better at small particle sizes.

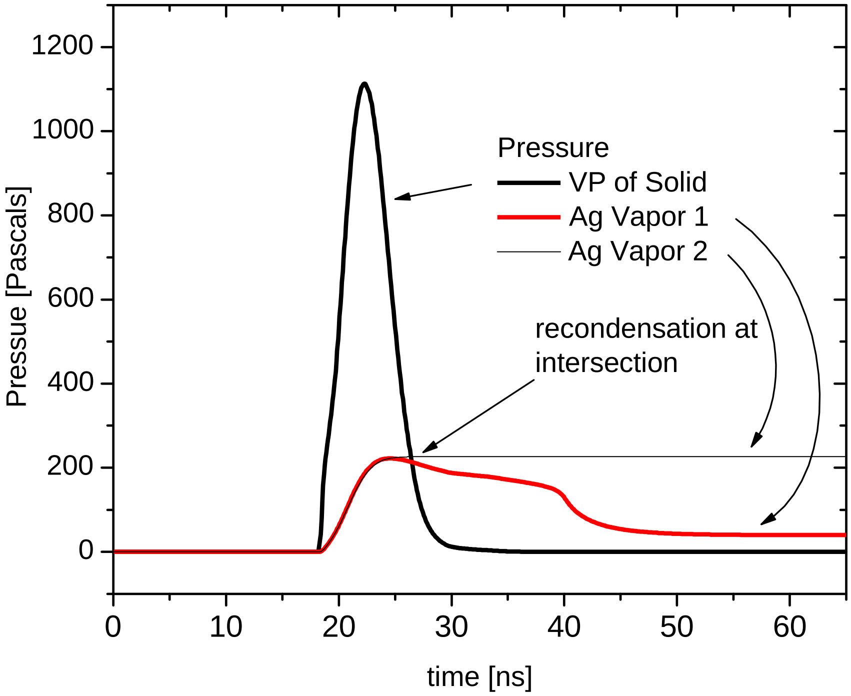

Figure 59: The intersection between vapor pressure of the NP and atomic silver pressure around the NP indicates recondensation. Ag NPs are expected to stop shrinking when diameter is 0.8 nm.

To take into account and explore a qualitatively behavior of the condensation process missing in our simulation, the Ag partial pressure of the gas surrounding the NP was calculated in two ways: (1) Using the ideal gas equation as a function of the temperature of the nanoparticle,

$$P(t) = Rn(t)T(t)\,, \qquad \textbf{- 42}$$

and (2) using the cumulative ideal gas equation integrated over time with the formula

$$P(\tau) = \int_0^{\tau} R \frac{dn(t)}{dt} T(t)dt \ , \qquad \textbf{- 43}$$

where *n(t)* is the number of moles per unit volume, *T* is the temperature of the nanoparticle and *R* is the ideal gas constant.

Fig. 59 shows that as the vapor pressure of the solid rises on the surface of the nanoparticle, the Ag surrounding partial pressure (in both calculations 1 and 2) goes up similarly. Nevertheless, when the vaporization pressure reaches its maximum at 22 nanoseconds the Ag atomic pressure keeps going up. This behavior leads to the intersection of both pressures at around 26 nanoseconds. Around this time, the solid vapor pressure and the pressure for the Ag vapor (1 or 2) are equal and recondensation of the atomic Ag onto the nanoparticle is expected. For times longer than the intersection time, our model becomes inaccurate because it is not considering recondensation and particle growth, (which changes *T(t), r(t)* and *n(t)*). The model predicted values for the particle size shown in Fig. 52 are therefore expressing the lowest limit for the real particle size. The model predicts that at the point when recondensation starts the Ag nanoparticles have shrunk to 0.4 nm in radius, which means that the nanoparticles do not complete vaporize and they remain nanoparticles after the second ablation.

According to Mie theory, larger particles absorb more heat and elevate their temperature well above the melting point of the materials. Because of the lack of experimental parameters at high temperatures, (such as surface energy, vapor pressure or heat capacity), our simulation becomes less accurate at these high temperatures. Before the collection the surrounding vapor will recondense on top of the NPs, according to the simulation and experimental data comparison.

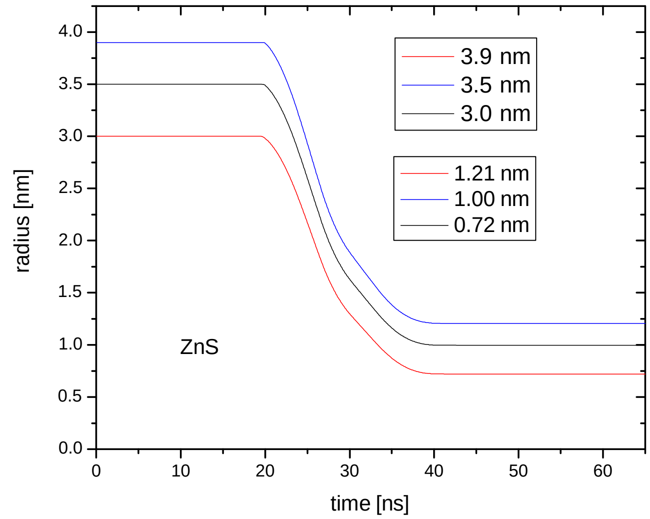

Figure 60 : Theoretically, the size distribution is predicted to narrow down 46% after second ablation.

A narrowing of the experimental size distributions is predicted by the simulation. It is seen from the simulation that larger particles will decrease their diameter in a larger absolute magnitude. Larger particles will shift to lower counts and the size distribution will become narrower. For ZnS this narrowing effect is measured for the value of *w* that decreases from 0.3 nm to 0.19 nm. The time domain of the simulation starts right before the laser pulse at time zero and it is stopped after the nanoparticles present no change in diameter or reach room temperature. In addition to the influence of contrast on our detection limits, one main reason to explain the larger experimental radius with respect to the theoretical predictions is that particle radii measured from supersonically impacted TEM grids may be not the real particle radius but a slightly larger radius due to deformation upon impaction as suggested by the non-spherical Ge nanoparticles shown in Fig.5b. Even Ag, that has the highest reported surface tension from these four materials has shown elastic deformations [44] after impaction on surfaces that lead to larger particle cross sections from the perspective of the TEM electron beam. Larger Ge or

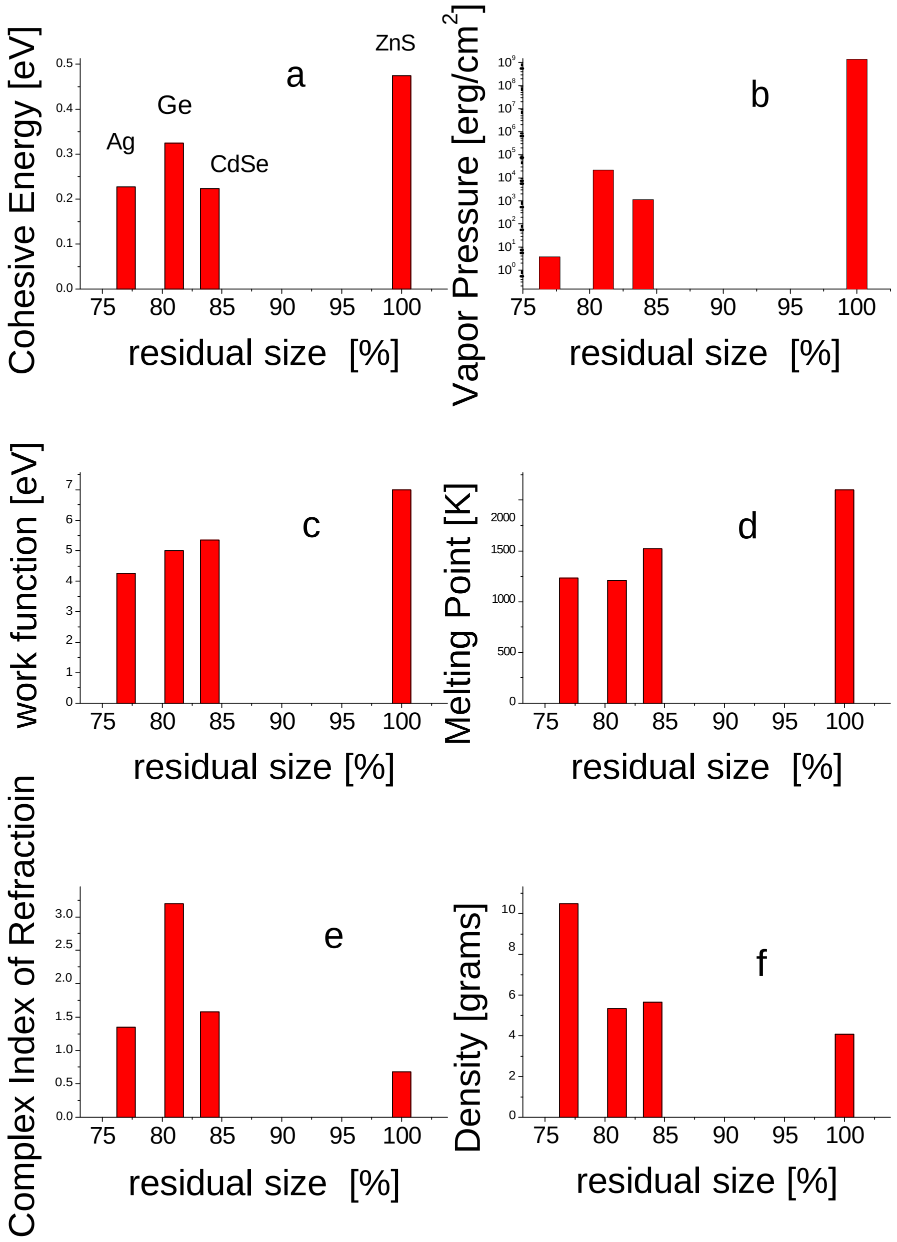

Figure 61: The experimental size reduction was plotted against parameters in the calculation. The ratio of the initial mass and the final mass of the TEM measured nanoparticles was calculated. Ag has a final radius of 77% its initial NP radius, Ge is 81% of its initial NP, CdSe is 84% and ZnS reminds unchanged (100%). a) cohesive energy, b) vapor pressure, c) work function, d) melting point, e) index of refraction, f) density.

CdSe particles (with lower surface tension than Ag), will deform on the TEM grid and could change in shape. To measure the size distributions we only counted spherical nanoparticles as seen in the TEM and this makes us ignore the amorphous large nanoparticles that were deformed upon impaction on the grid. This non-spherical big particle discrimination results in a larger number of smaller particles for the distributions.

When deformed, larger Ge particles are not counted. Most of the size originated errors are quantitatively measured when we measure the experimental size distribution width. Nevertheless, the charge density has the largest impact when computing the energy absorbed for the nanoparticles and their evaporation. The fact that we are able to see single particles and just a few clusters in the TEM images, show us that the particles have some average charge density left when we collect them.

iii. CdSe Luminescence

The two fluorescent peaks for single and double ablation spectra support the experimental radius sizes observed for CdSe NPs on TEM grids. Theoretically, the small mismatch of the PL calculated radius with the TEM values for the sizes is due to the approximation of the valence band with the parabolic model used in Eq. (41). Experimentally, this mismatch is explained through the differences in the collection by impaction between a quartz glass and a TEM grid. For these two surfaces the flows and minimum NP size that can be collected could be slightly shifted and lead to shifted size distributions.

6. CdSe & ZnS Core/shell Nanoparticles

a. EXPERIMENT

For the core/shell heterostructure fabrication process, our experimental apparatus is similar to one reported earlier, [7] with the addition of a double ablation cell shown schematically in Fig. 62**.** Two ablation processes take place in two UV transparent quartz ablation cells. In each of them a coaxial flow and an exhaust are used so as to focus the centered main aerosol flow through a skimmer. The centered main flow carries the feedstock material in the form of a micro-powder aerosol. The microparticles are suspended and dragged in the main flow by aerosol generators. In these aerosol generators, the semiconductor microparticle powder (99.9% ZnS ~3 μm & CdSe ~5 μm from Alfa Aesar Company) on top of a vibrating membrane in contact with an oscillating iron plunger that is driven by a solenoid at around 10 Hz. Pure He gas enters the aerosol generator and drags the microparticles downstream. Feedstock microparticle samples collected on carbon tape were taken to the Scanning Electron Microscope (SEM) to study their size and agglomeration rates.

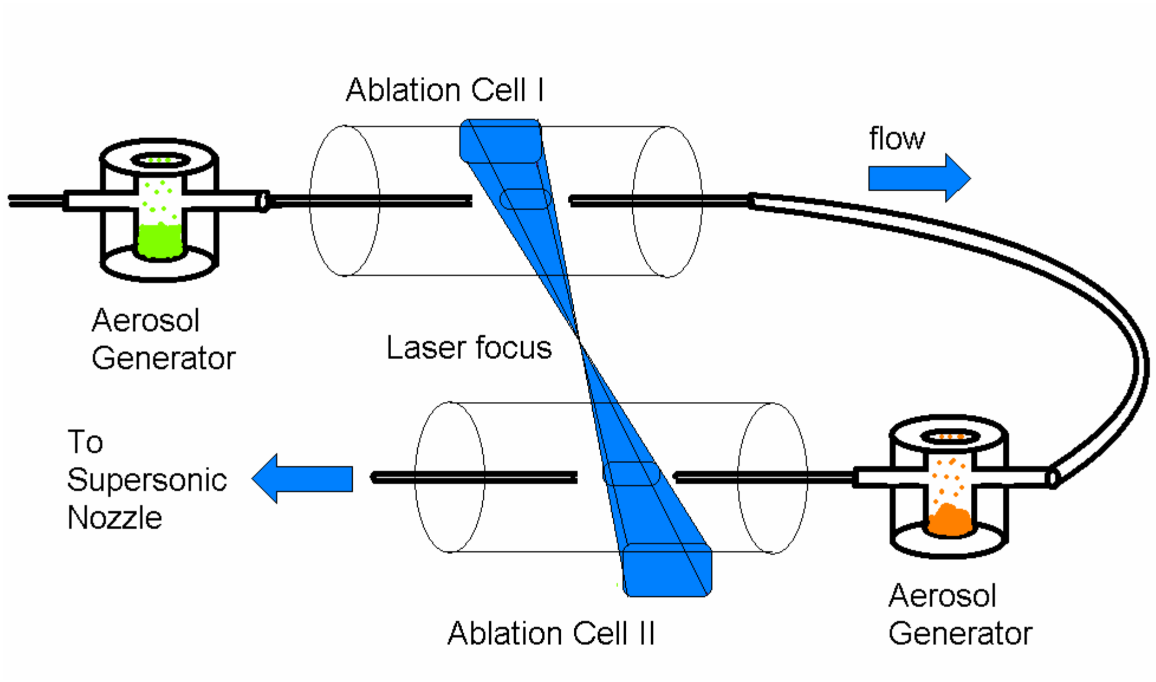

Figure 62: Scheme of the experimental apparatus. The same laser beam is used in both ablation cells. The particle flow follows the arrows clockwise. Each aerosol generator contains one semiconductor material.

The ablation laser source was a Lumonics KrF excimer laser (λ = 248 nm, 200 Hz rep. rate) with a pulse width of 14 ns. The output energy of the laser was focused by two transverse plano-convex cylindrical lenses. The setup was arranged so that the same laser beam was used in both ablation cells. After the two ablations, the core/shell nanoparticles were supersonically impacted, allowing us to collect the nanoparticles directly on top of a transmission electron microscope (TEM) grid sitting in vacuum. The supersonic nozzle was 400 μm in diameter with a stagnation pressure of 1 atm. The deposition time was from 2 s to 5 s to prevent TEM grid damage by non-ablated microparticles that impact on the support film. The material dependent emission from the ablated plasma plume was used to check alignment and determine ablation efficiency. To optimize the process, the focal spot could be moved laterally across the cells to adjust the ablation fluence.

The threshold fluences necessary to ablate CdSe and ZnS were measured by determining the minimum laser energy E required to visualize the ablation process. As mentioned above, the ablation process is seen by a characteristic plasma light emission. The fluence F is defined as the pulse energy divided by the cross sectional area A of the laser beam. To calculate the fluence threshold for these two materials, the minimum energy for which ablation emission is observed and the cross section of the beam were measured at the ablation zones. Laser energy losses in the lenses and quartz cells were taken into account in the calculation. We estimate the threshold for shock formation to be 0.1 J cm^{-2} and 1.3 J cm^{-2} for CdSe and ZnS respectively. Because errors can be large for absolute estimates due to uncertainties in focal areas, we determined the ratio of threshold fluences to be a factor of 13 ± 1.

To make a core/shell nanostructure, spherical ZnS nanoparticles are first generated by the standard LAM process described above. In a second cell, the nanoparticles are mixed with CdSe microparticles and ablated again. The second ablation process is size dependent. Here, the CdSe microparticles ablate just as the ZnS do in the first stage, but the ZnS nanoparticles (which have a diameter smaller than the wavelength of the laser and heat nearly uniformly) do not absorb enough light to create a shockwave. Because of laser heating to a high temperature, the nanoparticles partially evaporate, reducing their 3 nm radius by a factor of 2. This nanoparticle vaporization is in agreement with thermodynamic calculations. [45] The plasma from the exploding CdSe microspheres surrounds many of the ZnS nanoparticles which have an average density of 10^{14} cm^{-3}. Consequently, the ZnS nanocrystals act as seed particles for heteronuclear condensation to form ZnS/CdSe core/shell heterostructures. In addition, by interchanging the order of the two ablation processes we also made inverted CdSe/ZnS core/shell nanoparticles.

The CdSe and ZnS core/shell nanoparticles produced by LAM were further characterized by using HRTEM, EDS, SEM and diffraction patterns. The different size distributions for ZnS and CdSe are not only a result of the LAM process itself but also of the collection process. To obtain the size distributions from the analyzed images, radii of the nanoparticles were calculated with MetaMorph® software as a function of their contrast with the background. This contrast sets the limits for the minimum particle size that can be counted. The narrower size distribution for CdSe with respect to ZnS may be a consequence of the different ablation thresholds between the two materials. Although the mean radius of the ZnS particles is 3.3 ± 0.1 nm (Fig. 47), there are a few above 9 nm in radius. These few big ZnS core particles make it easier to probe the core/shell structures with the 5 nm EDS electron beam and resolve the core and shell in a single particle. The few useful particles above 9 nm in radius are expected as part of the long tail of the lognormal distribution. Smaller particles can be probed only once for core or shell EDS measurements. Consecutive core and shell EDS measurements can’t be done on small single particles because of beam damage after exposure to the electron beam mixes core and shell lattices and enhances atomic migration.

TEM grid samples for single ZnS and CdSe undergoing LAM were collected 10 cm downstream from the ablation region using direct jet impaction. When using the same laser fluence and carrier gas flow conditions, without further size selection, different size distributions were found for the two materials. Because of contrast limitations, the minimum particle size that could be counted under these conditions was 1.76 nm radius for ZnS and 1.48 nm radius for CdSe. Size distributions shown in Fig 46 were best fit to a lognormal distribution giving a mean radius of 3.1 ± 0.09 nm for CdSe and 3.3 ± 0.1 nm for ZnS nanocrystals.

When measuring the core composition using EDS within the TEM, the electron beam is aimed at the center of the particle but it goes through the thin shell as well. Therefore, higher peak counts in the spectrum correspond to the core and lower peaks to the shell. When the electron beam is aimed at the edge of the sphere only the edge of the beam reaches the core and therefore predominant peaks in the spectrum come from the shell material. To be sure that we are looking at core/shell structures and not just a smaller particle sitting on top of a bigger one, the TEM grid support stage was rotated. Only images of shelled spheres are invariant under such rotations. For several rotations, EDS measurements were made to probe the shell. After EDS measurements, the targeted spot is easy to visualize on the nano-sphere because the electron beam evaporates the targeted area of the particles and this looks like a bright spot under TEM imaging. For shells thicker than the focused electron beam, a rough estimate of the shell thickness can be obtained by scanning the beam across the radius of the sphere towards the center of the particle. As soon as the EDS spectrum detects the core, the scan is paused and the resultant visible ablated path across the shell gives an estimate of the shell thickness.

The different properties of ZnS and CdSe make the core/shell formation a non-symmetric process under the same laser and flow conditions. Large ZnS cores covered with CdSe shells are easier to observe than CdSe cores with ZnS shells because of the TEM Z contrast. To optimize the double cell configuration and to match the two different fluence thresholds with the two materials, we positioned our cells on either side of the focal point and placed the ZnS cell closer to the focus.

b. RESULTS

i. CdSe/ZnS Core/Shell

The micrographs allowed us to see this structure of the core and the shell (Fig. 63). FFT and diffraction patterns show that the generated core and shell materials are crystalline. If we zoom in on the HRTEM, the crystal fringes and faceted domains can be observed in the larger particles (Fig. 64). For 10 nm radius cores, shell thickness ranged from 4 to 8 nm thick. Smaller (~2.5 nm), dark clusters had smoother shells but crystal planes in the interface of the core shell structure were difficult to resolve. High Z contrast TEM imaging was useful to resolve thick shells. Due to the higher atomic number Z in CdSe, the electron scattering cross section is larger and the contrast is higher for CdSe than ZnS. The bigger the core the more difficult it is to have it completely covered with a shell.

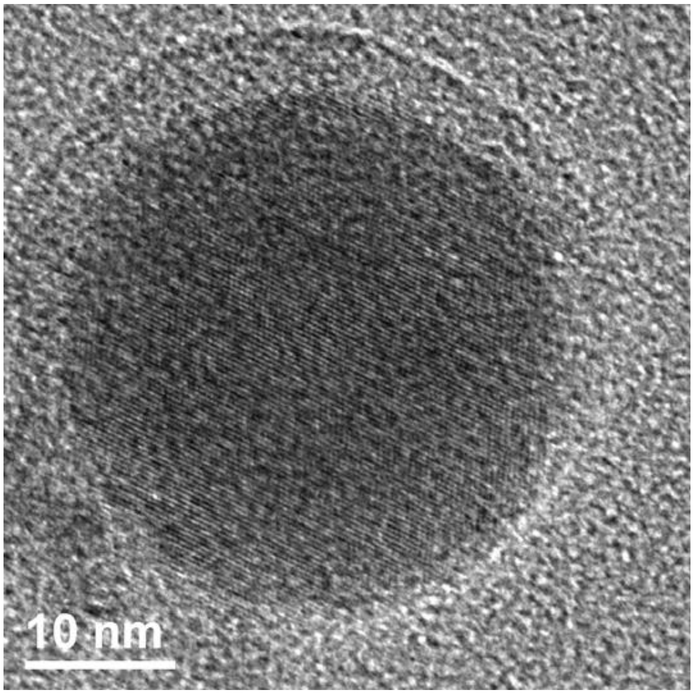

Figure 63: HRTEM micrographs of a CdSe/ZnS core/shell nanoparticle. The spherical darker core and covering lighter shell can be observed.

The ~2 nm EDS electron beam probe was used to reveal the composition of the core and shell separately to determine if we had the expected semiconductor core/shell configurations. Fig. 65 shows typical EDS spectra obtained in this experiment. Fig. 65b shows the EDS spectrum from the core (center of the core/shell nanoparticle) and Fig. 65a shows the EDS spectrum from the edge. This second spectrum reveals that no CdSe is present in the edge. In contrast, in the spectrum from the center of the sphere (Fig.. 65b), both CdSe and ZnS peaks are seen, but the concentration of CdSe is greater than that of ZnS (CdSe ~90% vs. ZnS ~10% relative percentages). These spectra and percentages confirm that the nanoparticles made in this process are CdSe/ZnS core/shell nanoparticles.

The presence of small quantities of ZnS in the EDS spectrum from the core is expected since the EDS electron beam hits both the shell and the core when performing EDS measurements from the center of the core/shell nanoparticle. The electron beam goes through a shell/core/shell interface as it crosses the nanocrystal. On the other hand, when the EDS beam used for these measurements is aimed with a diameter small enough to tangentially touch the edge of the sphere, only the ZnS registers in the spectrum. This probes only the shell.

For the CdSe/ZnS core/shell structures the shell is often not completely covering the core, and sections of naked cores can be seen in the micrographs. Approximately 5% of the analyzed nanoparticles present a completely formed ZnS shell. In the HRTEM micrographs, we can observe darker spots of ZnS that appear in the shell and distort its spherical shape, (Fig. 66). These may result from nanoparticles made in the ablation of the shell material.

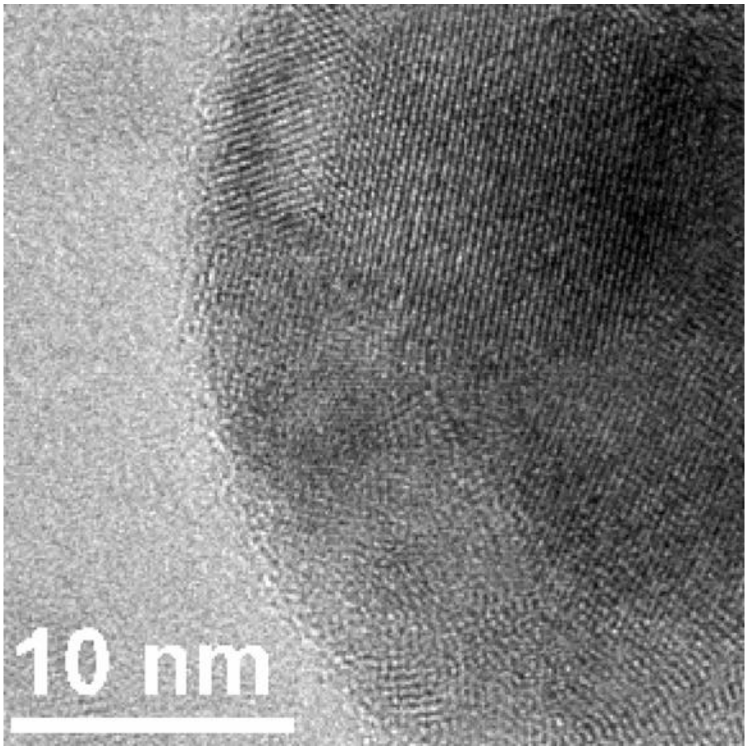

Figure 64: HRTEM micrograph of a shell close-up of a CdSe/ZnS core/shell nanoparticle. ZnS crystal planes can be seen in contrast to the darker CdSe core.

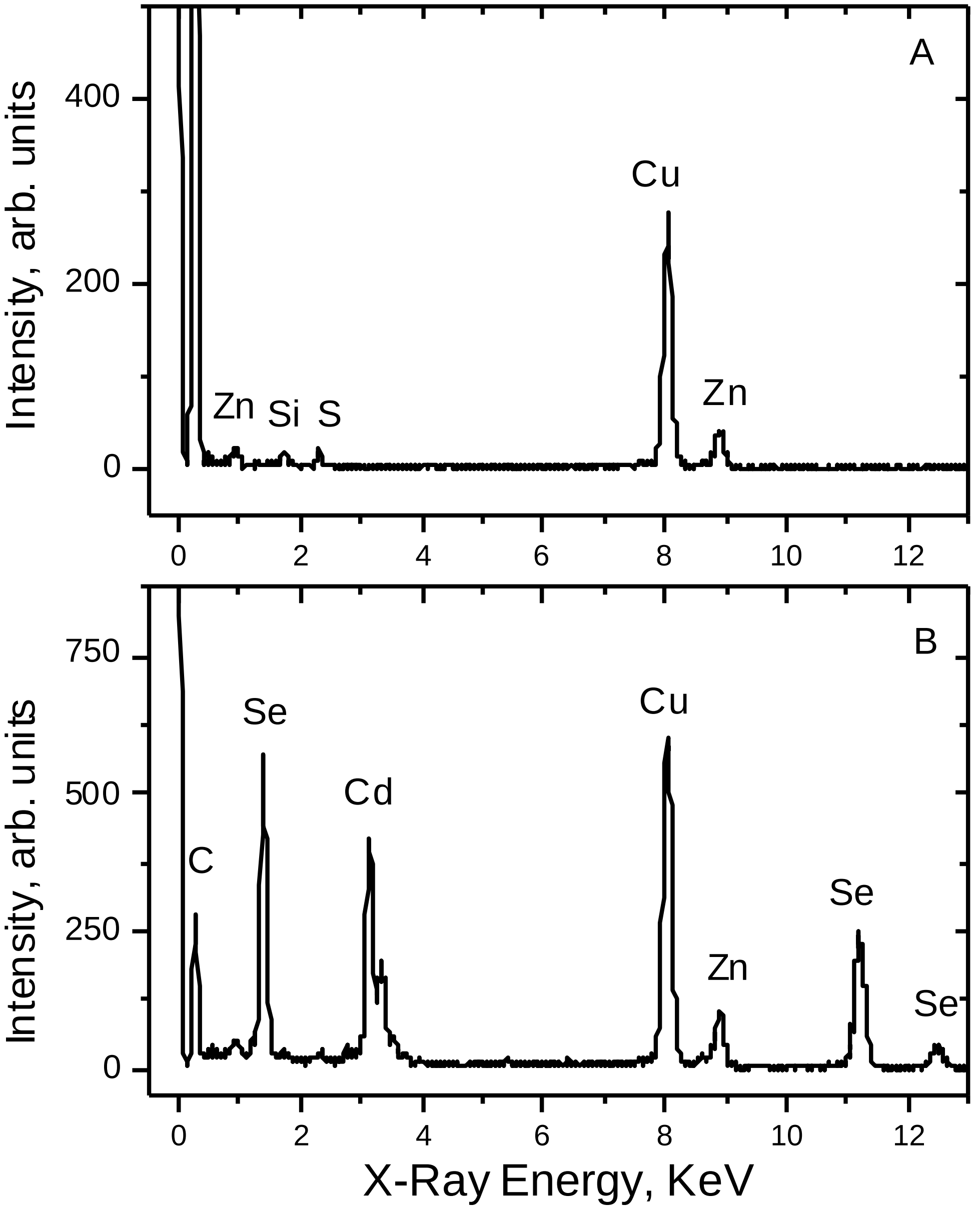

Figure 65: a) Spectrum from the edge of a core/shell nanoparticle. b) Spectrum from the center of a core/shell nanoparticle. Both semiconductor materials are present, but the concentration of ZnS is less than that of CdSe. The peaks at ~0, ~0.4, ~8 and ~1.8 keV can be ignored. They correspond to copper (Cu), carbon (C) and silicon present on the TEM grid.

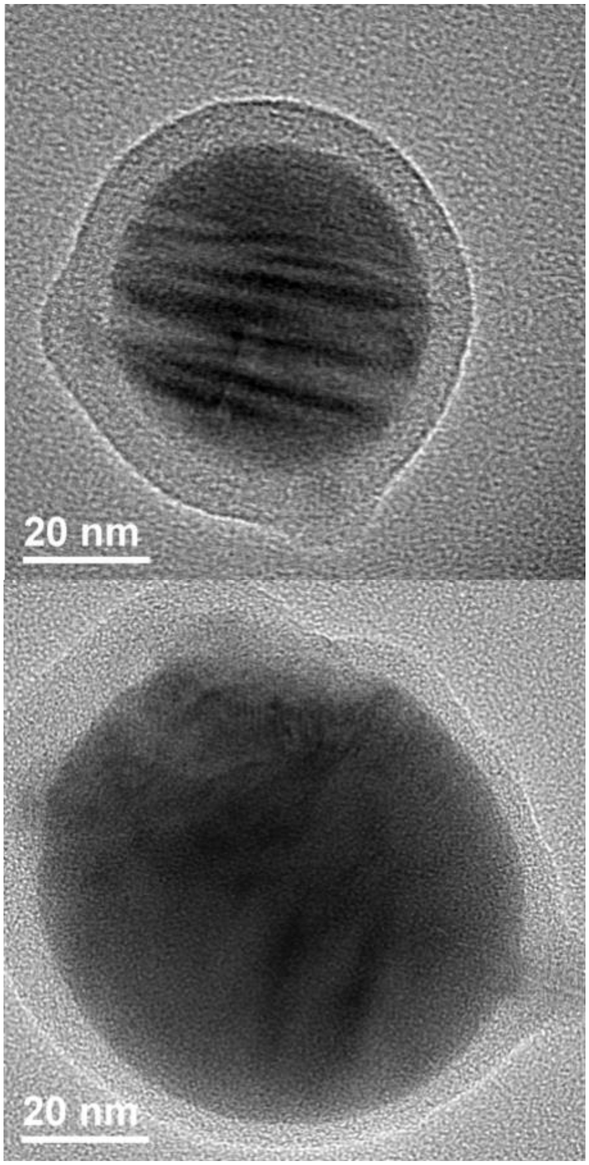

Figure 66: HRTEM micrographs of core/shell nanoparticles. In these cases, the CdSe cores are partially covered by ZnS. The ZnS shows up in the micrographs as the darker and crystalline parts in the shell. For the largest particles, proportionally less area is covered with a shell.

ii. ZnS/CdSe core/shell

Completely CdSe covered ZnS cores were seen with a process efficiency of 15% within a range ≥ 4 nm in radius. Just like for CdSe/ZnS structures, ZnS/CdSe core/shell nanoparticles with core radius of ~15 nm were seen coated with a highly contrasting and darker CdSe shell. As before, these characteristic images were expected due to a higher scattering cross section of the shelling material, as is shown in Fig. 67. Because of this contrast, the smallest core/shell heterostrucutes that we were able to resolve with the microscope were around ~4 nm in radius.

Crystal diffraction pattern insets demonstrate different structures for shells and cores as shown in Fig. 67. Each characteristic pattern identifies the crystal structure of CdSe and ZnS. The fact that the patterns change as we move across the particle indicates several distinguishable facets. To easily measure the crystal lattice spacing we look around for particles that were deposited on the TEM grid and were aligned with the electron beam in a particular zone axis. Each reported zone axis and measured lattice comes from a different nanoparticle. Lattice spacing was calculated from Fig. 67. At the upper part of the shell there is a clear (110) zone axis from which the

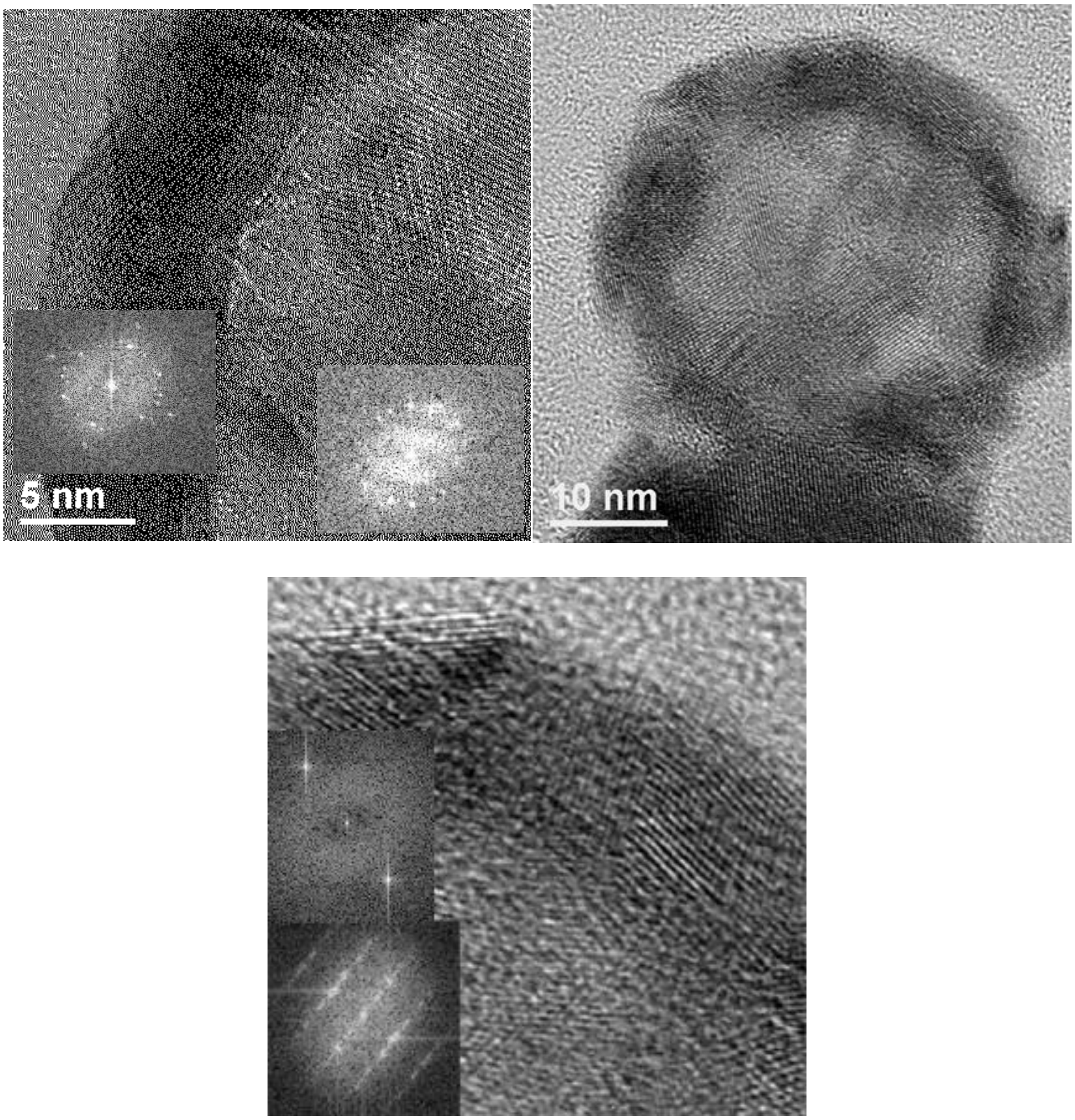

Figure 67: ZnS/CdSe core/shell micrographs. Above: ~20 nm (in radius) particle. Below: zoom in of crystal structure that can be identified as core and shell. Inset: FFT diffraction patterns for shell and core showing crystal orientations.

value of 6.99 ± 05 Å was obtained for the unit cell spacing, which is in agreement with the CdSe wurzite structure $C_o = 7.02$ Å. In the same way, the measured lattice parameter

C_o = 6.1 ± 1.5 Å for the (110) structure of ZnS showed an agreement with the Wurzite C_o = 6.23 Å value for bulk ZnS. It was also possible to get a (001) measurement of a_o =3.82 ± .05 Å for ZnS and see its hexagonal pattern in Fig. 67. This value is in agreement with the 3.811 Å for bulk ZnS.

Furthermore, a superposition of lattices coming from CdSe and ZnS is seen at the center of the nanoparticle. Unshelled cores are mostly single crystal and not multifaceted, hence we believe that these multifacets observed in the center of the nanoparticles are a result of the overlaying facets in the shell. The hexagonal pattern of the (001) zone axis is clearly seen in some segments at the center of core and outer shell. None of the measurements support a cubic Zincblende structure. Area selective EDS spectra show CdSe cores and ZnS shells as indicated by the highest peaks in Fig. 68.

In a few larger core/shell ~10 nm structures, different orientations and morphologies along the shell crystal could suggest that different shell nucleation sites start growing at separate points on the surface. Even though crystal structure was seen, no measurements of lattice constants were reported from these particles because they were off from any identifiable zone axis and the TEM stage couldn’t rotate enough to align the beam in the needed orientations.

c. DISCUSSION

After demonstrating that the LAM process behaves differently for ZnS and CdSe, it is not surprising that the shell formation process inside the second ablation cell is also different for the two semiconductors. According to the reported Mie absorption and thermodynamic simulations, [45] for a fixed fluence, ZnS nanoparticles irradiated in the second cell reduce their diameter by a factor of two. In contrast, CdSe nanoparticles reduce their diameter by a factor of three, (which makes it more difficult to measure their size distribution), inside the second cell. To invert the process we change the powders and the fluences. Changing the fluence helps for the optimization of the ablation but it indirectly affects the speed of the shell formation as we shrink and ionize the naked cores differently. This means that inverting the powders and readjusting the fluence area are not sufficient to invert the whole process. Observed differences in shell thicknesses and coverage efficiency support this asymmetry in the process.

In the case of the ZnS coated CdSe cores, the presence of the small Si peak in the EDS spectra is seen due to the impurities on the TEM grid support film. The support film is important to collect nanoparticles by impaction. Thick films show Si EDS peaks but provide strong films to collect higher numbers of particles.

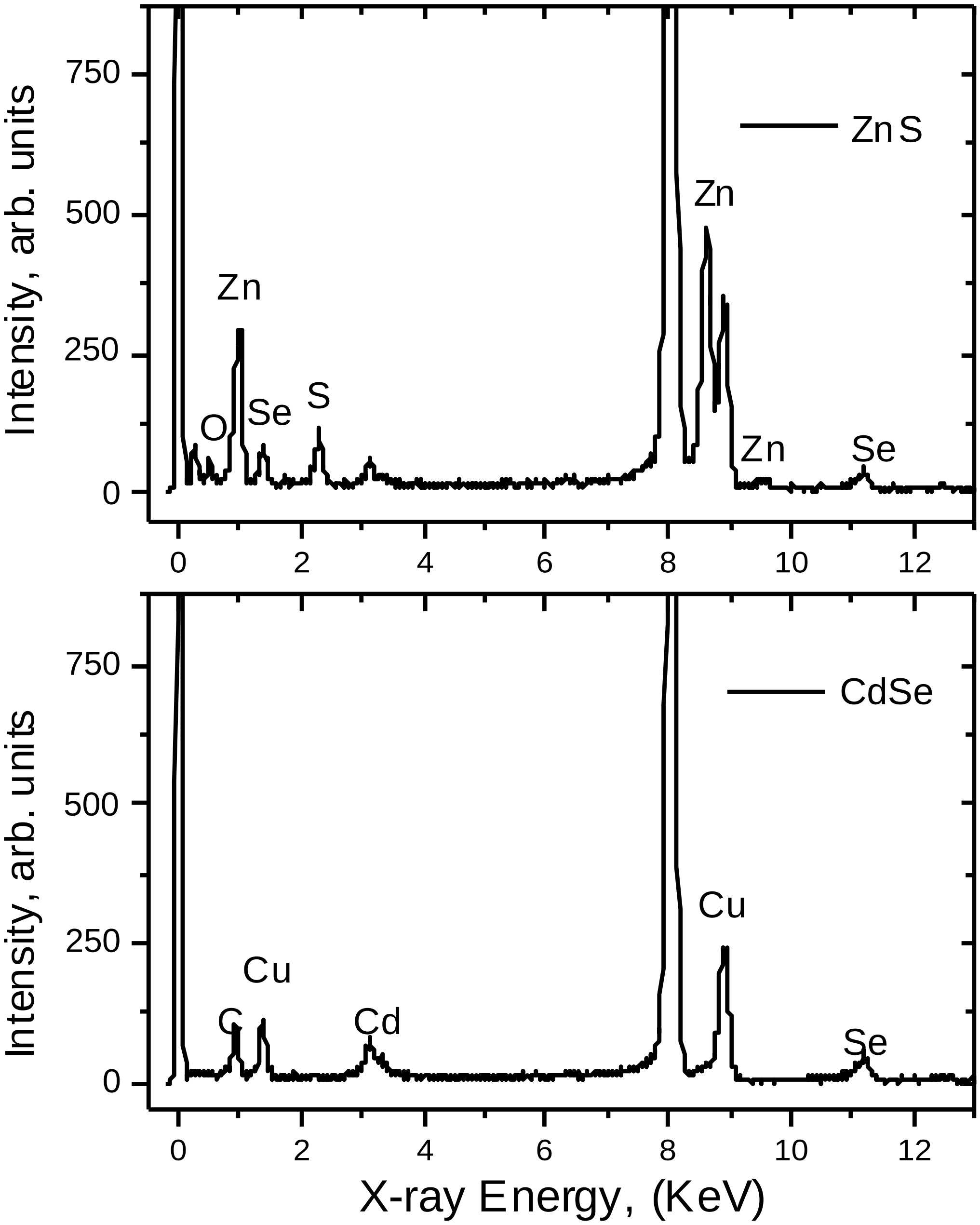

Figure 68: EDS measurements from a ZnS/CdSe core/shell nanoparticle. The peaks at ~0, ~0.4 and ~8 keV can be ignored. They correspond to copper and carbon present on the HRTEM grid. Upper spectrum was focused on center, (core). Lower spectrum was focused on the edge, (shell).

High resolution area selective EDS damages the particle, affecting subsequent measurements of the same particle. Fig. 69 shows the damage resulting from the highly focused ~2 nm EDS beam. A highly focused beam was necessary for spatial resolution and detection rates above the noise. Unfortunately, such conditions degrade the particle surfaces; once we have measured the core, the crystal surface and structure of the shell is slightly damaged. This is the primary reason it is difficult to probe and confirm the existence of a shell for small, (~2.5 nm) particles. Nevertheless, we believe that this double ablation process works for coating ~2.5 nm radius particles as well. During the formation of the shell we expect to have a homogeneous atomic cloud around the core nanoparticles. In this atmosphere, the atomic flow is the same in all directions and it is independent of the covered area. Therefore, large and small cores will have the same number of colliding atoms per unit area at their surface and similar shells will be formed. Nevertheless, we would expect more uniform shells for smaller nanoparticles both because the atomic diffusion rates are longer for smaller radii and the distances of diffusion are shorter.

This isotropic behavior for atmospheric collisions may be perturbed by the size distribution of exploding microparticles inducing slightly denser regions of vaporized material. Another type of perturbation that might affect the shell formation is the shock wave generated when ablating the second microparticle powder. As we described above, inside the second aerosol generator, nanoparticles are among microparticles. When the microparticles are ablated, nanoparticles with larger cross sections are pushed away from the ablation center. With a density of ~10^5 microparticles/cm^3, their average separation is 300 µm, and the ~2 µm particles will expand into a cloud with ~50 µm radius. This expansion depends upon the aersosol pressure and type of gas. [8,46] This final volume does not fill all the space. The space between these expanding microparticles contains only He and nanoparticles from the first ablation and produces some uncoated nanoparticles.

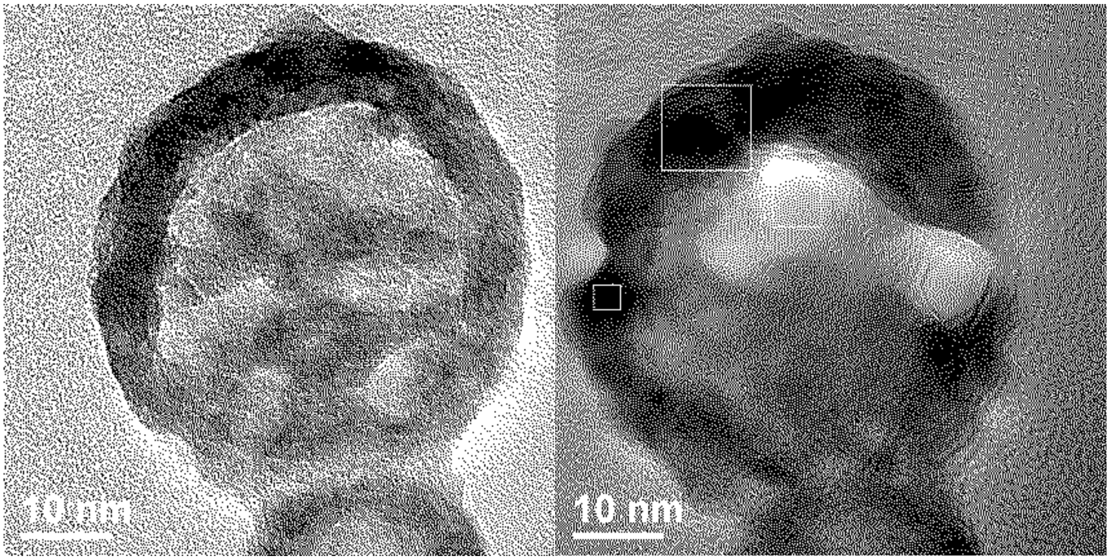

Figure 69: EDS effects on nanoparticles: On the left: before EDS measurement. On the right: after EDS measurements bright holes and deformed surface can be seen as the electron beam disrupt the crystal structure which makes image darker

This explains the observed inefficiency of completely shelled ~15 nm cores and the HRTEM observation of single crystal naked cores.

Coverage efficiency would be improved with an increased microparticle density. We are now working on improved powder feeders to reliably obtain higher microparticle densities. Lower pressures in the second ablation cell would give a larger expansion of the microparticle cloud also helping to more uniformly fill the volume with shell vapor. Lower pressures would also give thinner shells. [8] Finally, a filtration system or microparticle impactor [47] should be placed after the first ablation cell to prevent non-ablated CdSe microparticles from entering the second cell. Such particles are only ablated once and they become an obstacle for size selectivity.

7. Fluorescence of CdSe in Dimethyl sulfoxide (DMSO)

a. INTRODUCTION

The high surface-to-volume ratio of nanoparticles suggests that the surface properties are of great importance when studying relevant optical phenomena like quantum yield. Semiconductor nanoparticles that have smoother edges enhance band-edge luminescence and increased quantum yields. Larger atomic number and contrast difference between CdSe and ZnS make it an ideal semiconductor heterostructure for size reduction visualization in the HRTEM. The large amount of data on CdSe nanoparticles gives an ideal background to compare experiments with simulations, (that will be soon published), which require accurate experimental parameters.

Nanoparticles have been previously prepared by chemical synthesis, using organometallic reagents [48]. In such process the particles are made by nucleation and subsequent growth. The present work discusses a new inverted process for nanoparticles in which they reduce their diameter after the nucleation by using LAM in the gas phase. We also focus on how this size reduction affects the CdSe absorption and emission spectra.

b. EXPERIMENT

A two step LAM process for ZnS & CdSe core-shell nanoparticle production has been implemented (Fig. 62). In a first ablation cell, spherical ZnS nanoparticles are generated by a standard LAM process as described above. Following the flow lines, nanoparticles are mixed with CdSe microparticles and this mixture is ablated again. At this point, microparticles are normally ablated as in the first cell but nanoparticles (which have a diameter comparable to the wavelength), are not expected to develop a shockwave. Nevertheless, because of the high temperature, (above the material's melting points), nanoparticles start to reduce their diameter, (in agreement with thermodynamic calculations [45] which estimate that CdSe nanoparticles decrease their diameter by half after the second ablation). Due to a subsequent condensation of the ablated microparticle material around the nanoparticle seeds, core-shell structures are formed. Particles can be collected in dry films on glass or trapped in liquids.

To see the core shell structures or single CdSe nanoparticles, after the two ablations the nanoparticles were supersonically impacted, allowing us to collect the nanoparticles directly on top of a TEM grid, (Fig. 70), in vacuum. The supersonic nozzle was 100 µm in diameter with a stagnation pressure of 760 Torr. The order of the materials has been successfully exchanged to form inverted core-shell particles. Micrographs show high contrast TEM images. Crystal structures show evidence of Wurtzite symmetry for both semiconductor materials. Electron dispersive Scattering (EDS) inside the TEM is used to analyse the 20 nm ZnS & CdSe-core shell structures. Major core/shell work has been submitted for publication [30].

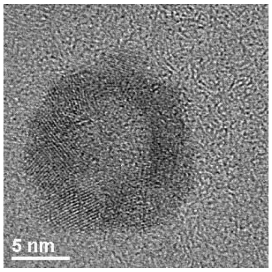

Figure 70: 10 nm ZnS/CdSe core/shell heterostructure

The present work focuses on the double ablation process effects on the luminescence of the CdSe nanoparticles. The same setup was used as in the core shell formation experiment, with the only difference that in this present report there is no ZnS present in the second aerosol generator shown in Fig. 62 and therefore, no mixture of nano and microparticles is ever formed. For trapping the small nanoparticles inside the liquids, we used the same method for impaction on surfaces in vacuum. We keep a continuously flowing thin layer of liquid on top of a flat surface. Nanoparticles are supersonically impacted on top of this thin layer of flat moving liquid that is injected into the vacuum chamber through a needle. Dimethyl Sulfoxide (DMSO) was used to collect the nanoparticles because of its low vaporization pressure, (VP = 0.42 Torr at 20^{o}C) and high surface tension, (ST = 43 dynes/cm at 20^{o}C). When DMSO is used we had no phase transitions during the process, unlike what happened with water, which solidified, (VP = 17.54 Torr, ST = 78 dynes/cm), or with Chloroform, (VP = 156.05 Torr, ST = 27.5 dynes/cm) which vaporized before we finish the collection run. The time it took to make one sample is 30 minutes, which was the sum of the three times we recycle the liquid to increase particle concentrations. After they were made, the samples were sealed in test tubes to avoid any water absorption by the hydrophyllic DMSO. Soon after made, samples were taken for measurements to avoid the absorption of water from the humid air.

A UV-VIS NIR Spectrometer (Cary 5000) and a fluorimeter were used to analyze the absorbed and emitted light. To prove consistency between doubly ablated nanoparticles and the size reduction, we studied the fluorescent blue shift that occurs on CdSe nanoparticles when their size is reduced.

c. RESULTS

Thermogravimetric (TGA) measurements (with a Perkin Elmer TGA 7)**,** show that we collected 31 ± 04 *μgr* of nanoparticles for every 40 *mg* of DMSO solution. This represents roughly a 1:1000 CdSe to DMSO mass ratio. In the TGA plot on Fig. 71 we can see how the DMSO suspended nanoparticles have already absorbed some water by looking at the change in slope of the weight as a function of temperature. The solution starts to evaporate and most of the water is gone when we start to evaporate DMSO. At around 5.8 minutes we are just below the boiling point of DMSO (189º C) and we observe an inflection point in the mass curve because up to this point the change in mass is mostly due to water evaporation but at this time DMSO starts to vaporize at a smaller rate than water. The change in the slope of the mass-time curve indicates that evaporation decelerates when we have 25 *mg* left. This mass left is mostly DMSO that it just starting to vaporize. At this point the temperature changes almost without weight loss because DMSO is absorbing the heat right before it saturates its heat capacity. A dramatic drop in weight is obvious at 20 mg when DMSO has absorbed enough heat to vaporize abruptly with no change in temperature. The same type of inflection point in the mass curve is seen when we finish vaporizing all the DMSO at 30 μg and the only mass left in the crucible is CdSe. Nevertheless, at this point we don’t see further weight drop because we are still far below the vaporization point of CdSe. TGA was done under nitrogen atmosphere to avoid flames. The DMSO flash temperature is 89º C.

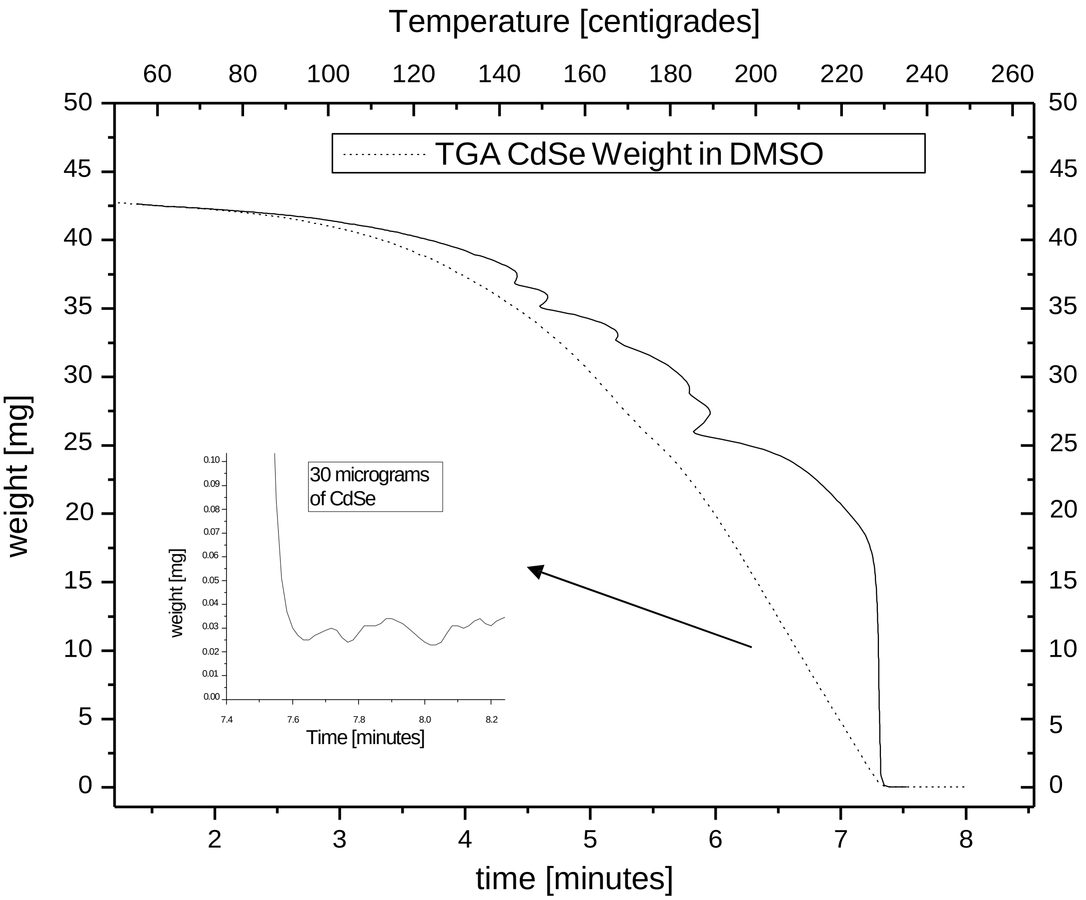

Figure 71: TGA measurements: Dotted line shows the change of the weight in time. Solid line shows the change of the weight in temperature. Inset shows a zoom in to resolve the nanoparticle weight and its uncertainty after DMSO vaporization.

After analyzing hundreds of nanoparticles, based on HRTEM micrographs, we could observe that their mean radius decreases from 2.5 ± 0.2 *nm* to 1.2 ± 0.2 *nm* (see Fig. 46). These values are obtained by fitting the experimental size distributions with Lognormal distributions with Eq.(40).

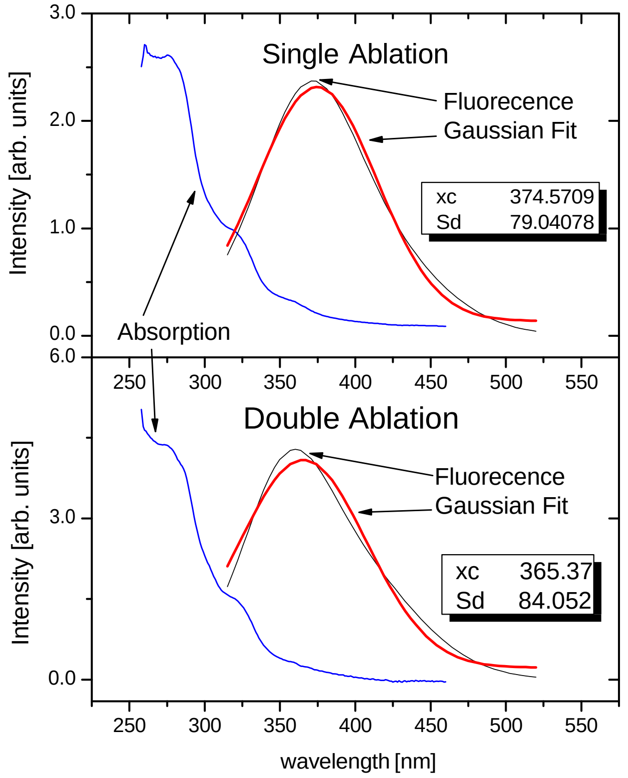

Figure 72: Absorption steps and PL peaks can be seen for CdSe nanoparticles. Top: Single ablated nanoparticles show a mean (xc) Gaussian peak at 374.6 nm. Bottom: Double ablated nanoparticles with a fitted Gaussian peak at 365.4 nm.

d. DISCUSSION

The width of the size distributions taken with TEM does show narrowing of the Lognormal peak. In contrast, the width of the fitted Gaussian peak of PL shows no narrowing after the double ablation.

Differences in the absorption spectra between single and double ablated particles are seen more clearly in the 360 *nm* shoulder, which is more obvious for the single ablated nanocrystals. The 325 *nm* and 280 *nm* shoulders in the absorption spectra are common to both, single and double ablation. This means that the larger particles that originate the 360 nm shoulder are reduced in size enough to quench this absorbance shoulder.

Uncertainties may occur when single ablated nanoparticles miss the second ablation. Despite of our control of laser and flow synchronization, turbulent flows in the on/off transient times may occur before we stabilize the continue gas injection. This makes false size distributions by adding more counts to the larger domain of the distribution. We average out these on/off transient times by making the run (with constant uniform flows) much longer, (one liquid cycle lasted 10 minutes). In the double ablation collection, large single ablated particles that skip the second laser shot are counted as double ablated in the measured size distributions. These single ablated particles fluoresce and absorb in the double ablation spectrum and they broaden the spectrum.

Equally important, on the other side of the size distribution, however, the smallest particles with radius shorter than 1 nm have lower contrast to be seen with HRTEM and these measurements will affect our observed distributions. The blue and soft UV lines of the PL peaks from nanoparticles collected in DMSO match the ones that correspond to band gap estimates for particles of ~1 nm in diameter that are reported by V. Soloviev et. Al [49]. Comparing the size of the particles from our size distributions and the size of the particles indicated by the theory [49] from the PL peaks of the DMSO trapped nanoparticles, it seems that smaller particles are easier to collect on DMSO than on top of TEM grids. We also have to consider that larger particles and agglomerates suspended in the liquids, precipitate faster than the smaller ones. Smaller particles are easily dispersed in the DMSO solution.

Surface impaction at supersonic velocities on the other hand, sets the theoretical minimum particle size that can be collected. This theory indicates that with our pressure gradient across the nozzle and the given density of our materials, the minimum particle radius that can be collected on the impaction surface after the expansion is 2.0 nm for CdSe. [45] This minimum particle size was calculated for an impaction on a hard surface and it might slightly differ from impactions on a hard surface covered by a soft liquid surface.

Dimethyl Sulfoxide-immersed CdSe nanoparticles showed a fluorescence peak that was fitted with a Gaussian distribution. The mean size of the fitted Gaussian is around 374 nm and standard deviation of 79 *nm* single ablated nanoparticles and a blue shift of ~10 nm was observed upon second ablation. Secondly ablated particles show its peak at 365 nm with a standard deviation of 84 *nm*.

The Quantum Yield (QY) was calculated using the formula [50],

$$QY = \frac{(A_{NP})(I_{dye})}{(A_{dye})(I_{NP})}\eta_{fl}\,, \qquad \textbf{- 44}$$

where A is the area under the PL curve and I and $\eta_{fl} = 0.75$ are the absorbance intensity and the tabulated quantum yield for Rhodamine 6G [51] at the excitation wavelength (300 nm), respectively. The *PL* curves were calibrated to the specific energy-dependent sensitivity of the detector to take into account different photon energies. Because the QY is measured in number of photons we have to correct the area under the

PL curve by the proportional photon energy E_{photon}. To do so one can use the equation: $\# photons(\lambda) \rtimes E_{photons} \propto PL(\lambda)$ before integrating the area A.

QY was calculated from the measured fluorescence and absorbance as 26% in comparison to Rhodamine 6G. Such emissions are expected for particles smaller than 2 nm in diameter [49] The data presented in Fig. 72 was filtered to remove the DMSO signal and it was reproducible for several samples of nanoparticles in solution. The intensities of the peaks have arbitrary units and were taken directly from the calibrated fluorimeter. The reported absorption peaks are comparable and blue shifted to the ones reported for Thiol-Stabilized CdSe nanocrystals [52].

8. Conclusions

We have shown evidence for the mean size reduction of Ag, Ge, CdSe and ZnS nanoparticles exposed to a high energy excimer laser UV pulse. HRTEM data together with digital image analysis were used to measure the size reduction. This size reduction is in agreement with PL measurements done on CdSe NPs. According to calculations, small (0.5 nm or less) ionized particles absorb twice as much laser energy as neutral nanoparticles. Experimentally, (except for ZnS) we observed the narrowing of the size distributions for these materials and we theoretically supported that at atmospheric pressure the evaporation is the strongest cooling mechanism. These studies show high material- dependent laser evaporation differences with respect to charge, size and surface tension. Ag high contrast images, PL measurements and the well studied experimental parameters in the simulation lead to the conclusion that the NPs reduce their mean diameters by a factor of 0.3 due to vaporization and followed by subsequent recondensation before they are collected by impaction. Ag served as a well studied model to develop the thermodynamic simulation and compare some of the simulation consequences with available published data. Ge has larger particles that were not counted because they were not spherical due to deformation upon impaction or coalescence due to its higher cohesive energy and much lower surface tension. ZnS on the other hand, shows no size change. When irradiated and collected by impaction in dry substrates or liquids, CdSe size reduction and size distribution narrowing has been measured by blue shifted fluorescence. [53]

Having the designed ablation chamber configured for liquid collection to make our samples we have used optical absorption and PL blue shifts to support and measure the size reduction of CdSe nanoparticles after laser radiation. TEM micrographs were taken to measure the size distribution shift to smaller sizes. These measurements are consistent with the nanoparticle CdSe/ZnS core/shell formation reported earlier. [30] Collecting nanoparticles by supersonic impaction in DMSO shows emission spectra of blue wavelengths. Control over the collection by impaction should be tuned to collect particles of specific bigger sizes and detect longer PL wavelengths.

When collected on dry quartz substrates we reported larger red fluorescing CdSe nanoparticles than the CdSe blue fluorescent nanoparticles in liquids. The differences in fluoresce between liquid and dry collected NPs are explained through interactions within the nanaoparticles and the solvent or the quartz substrate. Impaction on liquids is also expected to collect slightly different particle sizes than in solids. All the jet impaction theory presented in this work is valid only for hard surfaces and, even though we used high surface tension liquids, this theory should differ for these liquids.

We have produced CdSe & ZnS core/shell nanoparticles by laser ablation. Characterization methods that detect core/shell nano-structures have been used, (HRTEM, SEM, FFT and EDS), to verify the structure, geometry, size and composition of the nanoparticles. The material dependence of the laser ablation process yields core radii around 3 nm. The thickness of the shells was found to vary between 4 to 8 nm for ~10 nm radius cores. Thinner shells were more difficult to probe with the EDS beam. For the LAM technique to be applicable for surface passivation of bigger cores, core/shell generation efficiency has to be improved beyond the current 15% and 5% for ZnS/CdSe core/shells and the CdSe/ZnS core/shell particles, respectively. The present characterizations were supported by numerical simulations [45] and good agreement with the observed particle size distributions was found. In addition, a strong material dependent fluence threshold was seen for the two *IIB-VIA* type semiconductors. The low rate of complete ZnS shell formation on top of CdSe prevented us from gathering good statistics of increased quantum yield of the core-shell heterostructures in comparison with the simple CdSe core fluorescence. The Confocal microscope and Micro-Raman system fluorescent measurements proved no increase in the quantum yield for our core-shell samples with respect to the single core samples. Nevertheless, the nanoparticle fluorescence and the photobleaching of the quantum dots due to damage from high laser intensities was measured as a function of time.

We were able to further characterize the LAM process by showing that its high temperatures make it impossible to see semiconductor fluorescence during the ablation time. Fluorescence measurements from semiconductors can only be made when the NP have reached room temperatures and, as reported in chapter 3, the fluorescence is brighter as the temperature decreases due to more stable energy levels and exciton transitions. Nevertheless, the fluorescence from metals like Ag was predicted by Mie theory absorption calculations and proven with the ablation measurements that showed fluorescence below 450 nm of the hot Ag nanoparticles during the condensation time.

Appendix

CHEMICALLY GROWN PARTICLES.

Chemically grown quantum dots can use reactants like CdO and Selenium inside a reactor that consist s of a glass chamber under nitrogen or some other inert gas pressures. Depending on the actual procedure the temperatures in the reactor that is being stirred with a magnet can be as high 300 degrees C. Core shell nanoparticles made of CdSe and ZnS can be made also by an inverse micelle media technique and besides high quantum yields they show strains in the crystal structure that can be detected with X ray spectroscopy due to the 13% length difference in the longer Cd-Se bond with respect to the Zn-S bond. [54]

Chemically grown particles made by Dr. Korgel's group in UT where taken from a sample given to me by Dr. Ken Shi's lab former member Dr. Pablo Bianucci. Samples were dispersed in chloroform and we use a pipette to transfer the nanoparticles from the solution to a TEM grid. The samples were left to dry out in room temperature before inserted inside the TEM. The nanoparticles were not seen to be fluorescent under UV light.

As seen in Fig. 73, these nanoparticles seem to have narrower size distributions than LAM particles but apparently, there is some precursor in the solution that didn't react as seen in Fig. 74, which was taken at 7.1K magnification.

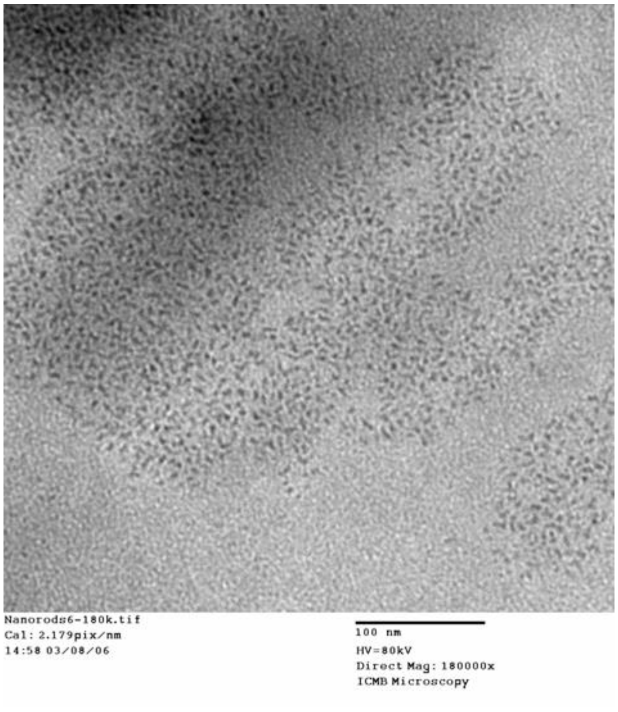

Figure 73 Chemically grown NP. high magnification

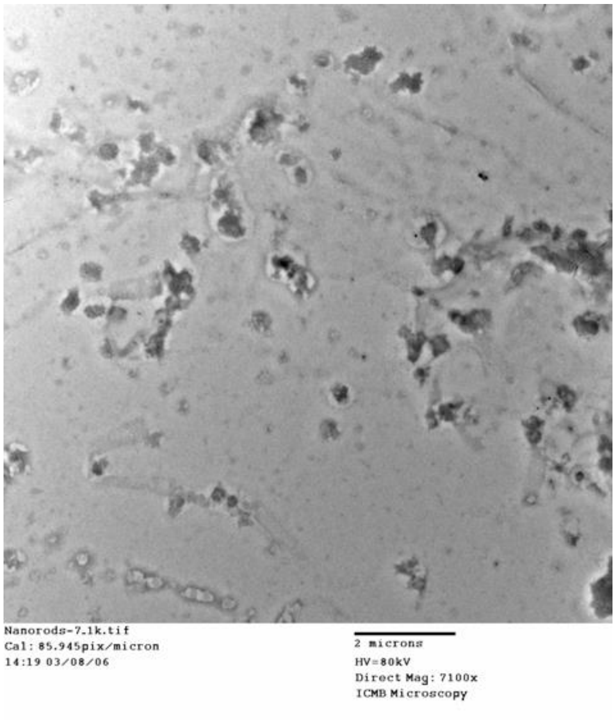

Figure 74 Chemically grown NPs at low magnification

Bibliography

---

[1] J. Rodriguez-Viejo, K. F. Jensen, H. Mattoussi, J. Michel, B. O. Dabbousi and M. G. Bawendi, “Cathodoluminescence and photoluminescence of highly luminescent CdSe/ZnS quantum dot composites” Appl. Phys. Lett. **70**, 2132 (1997).

[2] Sergei A. Ivanov, Jagjit Nanda, Andrei Piryatinski, Marc Achermann, Laurent P. Balet, Ilia V. Bezel, Polina O. Anikeeva, Sergei Tretiak, and Virctor I. Klimov et al. “Light Amplification Using Inverted Core/Shell Nanocrystals: Towards Lasing in the Single-Exciton Regime” J. Phys. Chem. B **108**, 10625 (2004)

[3] M. Bruchez Jr., M. Moronne, P. Gin, S. Weiss and A. P. Alivisatos, “Semiconductor Nanocrystals as Fluorescent Biological Labels”, Science **281**, 2013 (1998)

[4] M. A. Hines and P. Guyot-Sionnest, J. Phys. Chem. **100**, 468 (1996)

[5] Shimizu, K.; Empedocles, S. A.; Neuhauser, R.; Bawendi, M. G. Stark, Proc. -Electrochem. Soc., **98**-19, 280-285 (1999)

[6] C. Juang, H. Cai, M. F. Becker, J. W. Keto, J. R. Brock. Appl. Phys. Lett. **65**, 40 (1994)

[7] W.T. Nichols, John W. Keto, D.E. Henneke, J.R. Brock, G. Malyavanatham, M. F. Becker, and H.D. Glicksman, Appl. Phys. Lett. **78**, 1128 (2001)

[8] W. T. Nichols, G. Malyavanatham, D. E. Henneke, J. R. Brock, M. F. Becker, J. W. Keto and H. D. Glicksman, J. Nanoparticle Res. **2**, 141 (2000)

[9] Š. Kos, M. Achermann, V. I. Klimov, and D. L. Smith, Physical Review B **71**, 205309 (2005)

[10] B. O. Dabbousi, M. G. Bawendi, O. Onitsuka and M. F. Rubner, Appl. Phys. Lett. **66** (11), 1316 (1995)

[11] V. Colvin, M. C. Schlamp & A. P. Alivisatos, Nature (London) **370**, 354 (1994)

[12] S. Coe, W-K Woo, M. Bawendi and V. Bulovic, Nature (London) **420**, 800 (2002)

[13] D. Kovar, A. D. Albert, M. F. Becker, and J. W. Keto, In Press, Proceedings of the ASME Conference on manufacturing Science and Engineering (MSEC 2007), Advances in Synergistic Effects on materials and Processing. NO.MSEC2007-31170, Atlanta, GA, October 15-18 (2007)

[14] D. Gerion, F. Pinaud, S. C. Williams, W. J. Parak, D. Zanchet, S. Weiss, and A. P. Alivisatos. J. Phys. Chem. B, **105**, 8861-8871 (2001)

[15] S. Jeong, M. Achermann, J. Nanda, S. Ivanov, V. I. Klimov, and J. A. Hollingsworth, J. Am. Chem.. Soc., **127**, 19126-10127 (2005)

[16] V. A. Marple and B. Y. H. Liu ,“Characteristics of laminar jet impactors.” Environ. Sci. Technol. 648, (1974)

[17] V. A. Marple and K. Willeke, “Impactro Desing”. Atmos. Environ. **10**, 891, (1976)

[18] V. A. Marple and K. Willeke, “Inertial Impactors”, Springer-Verlag, New York, (1998)

[19] D. E. Henneke, “Nanoparticles Produced via Laser Ablation of Microparticles”, Dissertation, The University of Texas at Austsin, (2001)

[20] G. Arfken and H. Weber, “Mathematical Methods for Physicist, Academic Press, (1995)

[21] Al. L. Efros and A. . Efros, Sov. Phys. Semicond. 16, 772 *1982)

[22] Al. L. Efros and M. Rosen, “Quantum size level structure of narrow-gap semiconductor nanocrystals: Effecto of band coupling” Physical Review B, 58, (1998)

[23] G. Mie, Ann. d. Physik (4), 25, 57 (1908)

[24] M. Born, E. Wolf, “Principles of Optics”, Pergamon Press; 6th edition, (1984)

[25] Bohren C & Huffmann. D. “Absorption and scattering of light by small particles” John Wiley & Sons, Inc. (1998)

[26] V. Kasperovich and V. V. Kresin; Philosophical Magazine B, **78**, 385-396 (1998)

[27] B. Luk’ynachuk and W Marine, “On the delay time in photoluminescence of Si-nanoclusters produced by laser ablation., Applied Surface Science 154 -155, 314-319 (2000)

[28] Ralchenko, Yu., Kramida, A.E., Reader, J., and NIST ASD Team (2008). *NIST Atomic Spectra Database* (version 3.1.5), [Online]. Available: http://physics.nist.gov/asd3 [2009, April 1]. National Institute of Standards and Technology, Gaithersburg, MD.

[29] D. T O’Brien, “Laser ablation of Therfenol-D ($\mathrm{Tb}_{0.3}\mathrm{Dy}_{0.7}\mathrm{Fe}_{1.92}$) Microparticle Aerosol and Subsequent Supersonic Nanoparticle Impaction for Magnetostrictive Thick Films”, Dissertation, The University of Texas at Austin, (2006)

[30] I. Gallardo, K. Hoffmann, J. Keto, “CdSe & ZnS Core/shell Nanoparticles Generated by Laser Ablation of Microparticles ”, Applied Physics A, **94**, 65-72 (2009)

[31] K. L. Kompa et al. J. of Aerosol Sci., **19**, 491, (1988)

[32] V. Kasperovich and V. V. Kresin; Philosophical Magazine B, **78**, 385-396 (1998)

[33] L.E. Reichl, A Modern Course in Statistical Physics, John Wiley & Sons, inc. (1998)

[34] M. M. Stevanovic; Dependence of Vapour Pressure of Si and Ge; Thermochimica Acta, **77,** 167-176 (1984)

[35] David R. Lide et. al. CRC Handbook of Chemistry and Physics, 87th Edition (2006-2007).

[36] K. K. Nanda, S. Stappert et al, PRL **91** 106102 (2003)

[37] J.M Hunter, J.L. Fye, M.F. Jarrold, PRL, **73**, 2063, (1994)

[38] F. Benkabou, H. Aourag, M. Certier: Materials Chemistry and Physics **66**; (2000)

[39] Y. S. Touloukian et al. Thermophysical properties of Matter, **4**; Specific Heat; IFI/Plenum, NY (1970)

[40] S.H. Tolbert and A. P. Alivisatos; Proceedings: Nato ASI on Nanophase Materias, Greece; (1993)

---

[41] Yong Han, E. T. Voiles, L. Chumbley, and M. Aknic; J. Am Ceram. Soc. **77** [12] 3153 (1994)

[42] Otfried Madelung, “Semiconductors: Data Handbook”, Springer, pp 226, (2004)

[43] A. Keller, M. Fierz, K. Siegmann, A. Filippov and H. C. Siegmann; J. Vac. Sci. Technol. A **19**(1) (2001)

[44] A. Hilger, N. Cuppers, M. Tenfelde, and U. Kreibig; Eur. Phys. J. D **10**, 115-118; (2000)

[45] I. Gallardo, K. Hoffmann, J. Keto, “Metallic and Semiconductor Nanoparticle Evaporation Induced by Energetic Laser Pulses”, in preparation, (2008).

[46] G. Malyavantham, D. O’Brien, M. Becker, J. Keto and D. Kovar; J, of Nanoparticle Res. **6** 661 (2004)

[47] W. T. Nichols, G. Malyavanatham, D. E. Henneke, D. T. O’Brien, M. F. Becker and J. W. Keto, J. Nanoparticle Res. **4**, 423 (2002)

[48] Y. Sun, Y. Xia, “Shape-Controlled Synthesis of Gold and Silver Nanoparticles”, Science **298**, 2176-2179 (2002)

[49] V.N. Soloviev, A. Eichofer, D. Fenske and U. Banin. “Molecular Limit of a Bulk Semiconductor: Size Dependence of the Band Gap in CdSe Cluster Molecules”; J. Am. Chem. Soc **122**, 2673 (2000)

[50] B. Korgel. “CheE 384: Nanomaterials Chemistry & Engineering”, class handout HW3, (2004)

[51] T. N. Kopylova, R. T. Kuznetsova, V. A. Svetichnyi, et al. “Radiative and photochemical properties of organic compounds excited by high-power XeCl laser radiation”, Quantum Electronics, 30, 489-494 (2000)

[52] A. L. Roach, A. Kornowski, M. Gao, A. Eychmuller and H. Weller. “Synthesis and Characterization of a Size Series of Extremely Small Thiiol-Stabilized CdSe Nanocrystals”, J. Phys. Chem. B **103**, 3065 (1999)

[53] I. Gallardo, K. Hoffmann, J. Keto, Nanophotonic Materials V, Proceedings of SPIE, **7030**, 70300Z (2008)

[54] A. R. Kortan, R Hull, R. L. Opila, M. G. Bawendi, M. L. Steigerwald, P.J. Carroll, and L. E. Brus, “Nucleation and Growth of CdSe on ZnS Quantum Crystallite Seeds and Vice Versa, in Inverse Micelle Media” J. Am. Chem. Soc, 112, 1372-1332 (1990)

Vita

Ignacio Francisco Gallardo-Guerra, (Nacho), was born in Tampico Tamaulipas, Mexico on October 4th, 1977, the son of Graciela Alejandra Guerra de Gallardo and Miguel Gallardo Rodriguez. After completing high school at Instituto Cultural Tampico, he entered Universidad Nacional Autonoma de Mexico, (UNAM), on 1997. He received a degree of Bachelor of Science in August 2002 with a major in Physics. In a couple of weeks after graduation he entered Graduate School in The University of Texas at Austin to pursue a Ph.D. degree in the Physics Department under the supervision of Professor John Keto. During his stay in the University he founded the Friday Lunch graduate lunches (2002-2008) and the Okabe Car, sharing plan, (2008-present). Ignacio enjoys his free time camping and collecting priceless stones.

Permanent address: 1107 West Annie ST., Austin, Texas 78704
This dissertation was typed by the author.